

**OPTICAL STUDIES OF METAMATERIALS AND
BOSONIC SPECTRA OF HIGH- T_c SUPERCONDUCTORS**

**OPTICAL STUDIES OF METAMATERIALS AND BOSONIC
SPECTRA OF HIGH- T_C SUPERCONDUCTORS**

By

JING YANG, M. Sc.

A Thesis

Submitted to the School of Graduate Studies

in Partial Fulfilment of the Requirements

for the Degree

Doctor of Philosophy

McMaster University

© Copyright by Jing Yang, 2008

DOCTOR OF PHILOSOPHY (2008)
(Physics and Astronomy)

McMaster University
Hamilton, Ontario

TITLE: **Optical Studies of Metamaterials and
Bosonic spectra in High- T_c superconductors**

AUTHOR: **Jing Yang**
B. Sc., 2003 (Peking University, P. R. China)
M. Sc., 2005 (McMaster University, Canada)

SUPERVISOR: **Professor T. Timusk**

NUMBER OF PAGES: **xvi, 127**

Abstract

The optical spectroscopy techniques have been used to investigate left-handed behavior of metamaterials as well as the electron-bosonic spectral functions (or Bosonic spectra) of high-transition-temperature superconductors (or high- T_c superconductors) in the research work of this thesis.

The periodic double-ring split-ring resonator (SRR) array was one of the first proposed magnetic metamaterials which could give rise to a negative magnetic permeability ($\mu < 0$). In the traditional design of negative index metamaterials, the SRR arrays were combined with continuous metallic wires that provide a negative electric permittivity ($\epsilon < 0$). However, the requirement of an unbroken electrical connection between unit cells would be challenging in building contoured devices. In our study, we carefully examine the electromagnetic properties of the double-ring SRR arrays on silicon substrates in the mid-infrared frequency regime experimentally and numerically. For light at normal incidence, we observe that an electric resonance in the outer ring and a magnetic resonance in the inner ring exist at similar frequencies in one of our samples, which suggests that the double-ring SRR array could have simultaneous a negative permittivity and a negative permeability, or a left-handed behavior. Our conjectures are confirmed by the numerical simulations. We also propose a new left-handed metamaterial composed of two single-ring SRRs in each unit cell. The left-handed behaviors in our designs originate from the SRR structure itself only and therefore, there are no metallic continuous wires involved compared to the conventional left-handed SRR metamaterials.

The high- T_c superconductor samples studied here are highly under-doped $\text{YBa}_2\text{Cu}_3\text{O}_{6.35}$ ($\text{YBCO}_{6.35}$), nearly optimally doped monolayer $\text{HgBa}_2\text{CuO}_{4+\delta}$ (Hg1201), Zn- and Ni- doped $\text{Bi}_2\text{Sr}_2\text{CaCu}_2\text{O}_{8+\delta}$ (Bi2212) single crystals. We experimentally de-

termine the optical constants of the samples and numerically extract the electron-boson spectral functions from the optical scattering rate by either an analytic formula or a maximum entropy inversion technique. We find that the bosonic mode obtained from the optical data is consistent with a peak in the q -averaged susceptibility seen in the magnetic neutron scattering studies. The comparisons of the bosonic spectra between YBCO_{6.35} and YBCO_{6.50}, monolayer Hg1201 and trilayer Hg1223 (HgBa₂Ca₂Cu₃O_{8+ δ}), Zn-doped and Ni-doped Bi2212 characterize the variation of the bosonic spectra with the hole concentration, T_c as well as the magnetic and non-magnetic atom substitution.

Acknowledgements

Firstly, I would like to express my deep gratitude to my supervisor, Prof. Thomas Timusk, for his superb guidance, encouragement and support to my Ph.D. research projects all along during the years. Without his patience, understanding and consideration, I couldn't finish my Ph.D. studies so smoothly. I particularly appreciate the opportunities provided by Dr. Timusk for attending all kinds of academic conferences and workshops, which are invaluable experiences for me.

I am also very thankful to Dr. Jungseek Hwang, Prof. Jules Carbotte and the supervisory committee members, Prof. John Preston and Prof. Natalia Nikolova for their tremendous help and helpful discussions. Lots of thanks to Paul Dube for supplying plenty of liquid helium for the temperature-dependent experiments. Thank Steve Koprach for his technical instructions on the scanning electron microscope. Thanks to Graham Pearson for offering the training courses for the Nano Pattern Generation System (NPGS) E-beam lithography system. Thank Doris Stevanovic and Zhilin Peng for providing the cleanroom facility trainings.

I would like to thank the staffs in Physics main office as well for all the kind assistance they offered.

Last but not least, I would like to give my deepest appreciation to my parents and Yi Ma for their love, concern, encouragement and supports.

Hamilton, Ontario

June, 2008

Jing Yang

Contents

Abstract	iii
Acknowledgements	v
Table of Contents	vi
List of Figures	x
List of Tables	xvi
1 Introduction and Motivation	1
1.1 Negative Refractive Index Metamaterials	2
1.2 Bosonic Spectral Density of HTSCs: Probed by Optical Spectroscopy	8
1.2.1 Model Fits Based on Sharapov’s Formula	13
1.2.2 Eliashberg Inversion Based on a Maximum Entropy Method .	16
1.3 Thesis Outline	18
2 Optical Measurements	21
2.1 Introduction — FT-IR spectrometry	21
2.2 Reflectance Measurements	25
2.2.1 Setups of Reflection Spectrometry	25

2.2.2	The <i>In Situ</i> Evaporation Technique	28
2.2.3	Steps Towards Good Optical Alignments	29
2.2.4	Summary of Temperature-dependent Measurements	31
2.2.5	Low-temperature Detectors Preparations	33
2.3	Transmittance Measurements	34
2.3.1	Setups of Transmission Spectrometry	34
2.3.2	Area Correction	34
2.4	Infrared polarizers for anisotropic studies	36
3	Theory and Methods of Analysis	37
3.1	Introduction	37
3.2	Optical Response of Solids	37
3.2.1	Optical Parameters	37
3.2.2	Kramers-Kronig Relations	40
3.2.3	Low- and High- Frequency Extrapolations	41
3.2.4	Drude Model, Extended Drude Model and Drude-Lorentz model	42
3.2.5	Estimations of ϵ_H and ω_p	45
3.3	Bosonic Spectra Extracted From Optical Scattering Rate	47
3.3.1	Sharapov's Formula (Model Fits)	47
3.3.2	Maximum Entropy Inversion	49
3.4	Numerical Simulations for Metamaterials	51
3.4.1	Calculations of <i>S</i> -Parameters	51
3.4.2	Effective Material Parameters Retrieval	54
4	Optical Studies of Metamaterials	57
4.1	Introduction	57
4.2	Sample Fabrications and Characterizations	57

4.3	Left-Handed Behavior of Split-Ring Resonators	60
4.3.1	Left-Handed Behavior in A Double-Ring SRR Array	60
4.3.2	Left-Handed Behavior in A Single-Ring SRR Cubic Structure	68
4.4	Summary	71
5	Bosonic Spectra of Highly Underdoped Y123	73
5.1	Introduction	73
5.2	Annealing Processes	73
5.3	The Experimental Results	77
5.4	Model Fits of $1/\tau(\omega)$ and Discussion	85
5.5	Summary	93
6	Bosonic Spectra of Optimally doped Hg1201 and Hg1223	95
6.1	Introduction	95
6.2	The Experimental Results	95
6.3	The Bosonic Spectra of Hg1201 and Hg1223	98
6.4	Summary	101
7	Bosonic Spectra of Zn-Bi2212 and Ni-Bi2212	103
7.1	Introduction	103
7.2	Sample Preparations	103
7.3	Experimental Results	104
7.4	Discussion: the Bosonic Mode	107
7.5	Summary	115
8	Conclusions	117
	References	121

List of Figures

1.1	An illustration of the intermediate-energy electronic excitations in the high- T_c superconductors (Basov and Timusk, 2005).	2
1.2	(a) The normal refraction for two media which both have positive refractive indices. (b) The anomalous refraction where the second medium has a negative refractive index, but doesn't violate the Snell's law. . .	4
1.3	The schematic diagrams of one element of the double-ring split-ring resonator array (Left) and the magnetic resonance in it when the magnetic component of the incident light is normal to the array (Right). .	6
1.4	Structures of unit cells of high- T_c cuprates with different number of CuO_2 layers.	9
1.5	The phase diagram of the $\text{YBa}_2\text{Cu}_3\text{O}_{6+\delta}$ system, a representative of the HTSCs families. (Refer to (Ahn et al., 2003)) The circular and triangular symbols represent two of the underdoped Y123 samples that are discussed in this thesis.	11
1.6	A schematic diagram of the evolution the Cu-O chains in $\text{YBa}_2\text{Cu}_3\text{O}_{6+\delta}$ with a variation of the oxygen content $6+\delta$	15

2.1	Top panel: A schematic diagram of the FT-IR spectrometer with the reflectance measurement setups. Bottom panels: Photographs of the beam-focusing compartment (Left) and the sample stage for reflection (Right).	23
2.2	A typical interferogram (a) and the power spectrum (b) for a mid-infrared light source.	24
2.3	Left panel: A schematic diagram of the setups for transmission measurements. Right panel: The photographs of the sample stage for transmission (Top) and the beam-focusing chamber to focus the transmitted light to the MCT detector (Bottom).	35
3.1	The real and imaginary parts of the optical conductivity (a) and reflectance (b) of a typical Drude metal.	42
3.2	In this example the cutoff frequency ω_c is defined as the point where $\alpha(\omega)$, the absorption coefficient of the low frequency Drude conductivity, extrapolates to zero.	46
3.3	The density of states of the quasiparticles in vicinity of the Fermi energy for the normal states of the highly underdoped YBCO _{6.35} . . .	48
3.4	The model used to calculate the transmission of a periodic SRR array on a Si substrate.	52
3.5	The model for simulations of the S -parameters of a periodic SRR array.	53
4.1	The SEM pictures of the overview and the individual elements of the double-ring SRRs samples, SRRs #1 and SRRs #2.	58

4.2	(a) The measured transmission spectra of the SRRs #1 sample for two orthogonal polarizations of light, E parallel to the sides featuring gap of the SRRs (solid red curve, for short, E_{\parallel}) and E perpendicular to the sides featuring gap (dashed blue curve, for short, E_{\perp}). (b) The numerically simulated transmission spectra for E_{\parallel} (solid red curve) and E_{\perp} (dashed blue curve).	61
4.3	(a) The measured transmission spectra of the SRRs #2 sample for two orthogonal polarizations of light, E parallel to the sides featuring gap of the SRRs (solid red curve, for short, E_{\parallel}) and E perpendicular to the sides featuring gap (dashed blue curve, for short, E_{\perp}). (b) The numerically simulated transmission spectra for E_{\parallel} (solid red curve) and E_{\perp} (dashed blue curve).	62
4.4	The simulated transmission spectra of SRRs #2 for E_{\parallel} (solid red curve) and E_{\perp} (dashed blue curve), replotted from Fig. 2(b). The dash-dotted (pink) and dotted (green) curves are for E_{\parallel} for the inner ring only and outer ring only, respectively.	63
4.5	The surface current densities at frequencies which are indicated by dips α , β and γ , as seen in Figure 4.4.	64
4.6	The retrieved effective parameters of the double-ring SRRs whose dimensions have been increased by 1000 times in order to increase the strength of the magnetic resonance in the inner ring.	66
4.7	One unit cell of the single-ring SRR cubic structure and the configuration of the incident EM wave.	69
4.8	The retrieved effective parameters of the proposed single-ring SRR cubic structure.	70

5.1	Sketch of the home-made annealing facility.	74
5.2	The transition temperature T_c as a function of the annealing temperature for YBCO _{6.45} (Veal et al., 1990) (squares) and our YBCO _{6.35} sample (triangles).	75
5.3	The magnetic susceptibilities of the original YBCO123 sample and the sample annealed at two different temperatures.	76
5.4	(a) a-axis reflectance data of the highly underdoped YBCO _{6.35} sample at 9 different temperatures above T_c , up to 10,000 cm ⁻¹ . (b) The expanded view of the low-frequency reflectance.	78
5.5	The optical conductivity (a) and the optical scattering rate (b) of the highly underdoped YBCO _{6.35} sample at 9 different temperatures above T_c	79
5.6	The optical conductivity (a) and the optical scattering rate (b) of the highly underdoped YBCO _{6.35} sample at different temperatures above T_c , after the phonons have been removed.	82
5.7	A comparison of the optical scattering rate between YBCO _{6.35} (a) and ortho-II YBCO _{6.50} (Hwang et al., 2006a) (b) at different temperatures, with phonons removed.	83
5.8	The temperature-dependent dc resistivity of the highly underdoped YBCO _{6.35} extracted by extrapolating the optical conductivity to zero frequency.	84
5.9	The model fittings to the experimental data of optical scattering rate at $T=30$ K with bosonic mode only in $I^2\chi(\Omega)$	87
5.10	(a) The bosonic spectra of YBCO _{6.35} at different temperatures. Inset shows an expanded view of the low-frequency mode. (b) The resulting fits to the optical scattering rate.	88

5.11	The area of the mode that peaks at 5 cm^{-1} , the area of the step-like background, and the total area of $I^2\chi(\Omega)$ shown in Figure 5.10. . . .	89
5.12	Comparisons between the bosonic mode of $I^2\chi$ determined by our study (left panels) and the central mode of the local magnetic spin susceptibility spectrum determined by neutrons (right panels) (Stock et al., 2006, 2008).	91
5.13	A comparison of the Bosonic spectral density of the $\text{YBCO}_{6.35}$ (a) and the ortho-II $\text{YBCO}_{6.50}$	92
6.1	The reflectance (a) and optical conductivity spectra (b) of Hg1201 at eight different temperatures.	96
6.2	The optical scattering rate of Hg1201 at different temperatures. Inset: the optical scattering rate of trilayer Hg1223 ($T_c=130 \text{ K}$) (McGuire, 2001).	97
6.3	(a) The fits to the optical scattering rate of Hg1201 at different temperatures by using the maximum entropy inversion process. (b) The bosonic spectral density of Hg1201 at different temperatures.	99
6.4	(a) The fits to the optical scattering rate of Hg1223 at different temperatures by using the maximum entropy inversion process. (b) The bosonic spectral density of Hg1223 at different temperatures.	100
7.1	The reflectance and optical conductivity spectra at different temperatures for the Zn-substituted Bi2212 sample (a and b) and for the Ni-substituted sample (c and d).	105
7.2	The optical scattering rate and the real part of optical self-energy of Zn-Bi2212 (a and b) and of Ni-Bi2212 (c and d).	106

7.3	(a)-(d) Expanded view of the real part of optical self-energy at low frequencies for Zn-Bi2212, Ni-Bi2212, OPT(1) Bi2212, and OPT Bi2212. (e)-(h) The derivative of $-2\Sigma_1^{op}$ with respect to frequency for Zn-Bi2212, Ni-Bi2212, OPT(1) Bi2212, and OPT Bi2212.	108
7.4	The slope of the right side of the peak in $-2\Sigma_1^{op}$ relative to the background, as a function of temperature for Zn-Bi2212, Ni-Bi2212, OPT(1) Bi2212, and OPT(2) Bi2212.	109
7.5	The extracted bosonic spectra of Zn-Bi2212 (a) and Ni-Bi2212 (b). .	111
7.6	(a) The amplitude of the bosonic mode relative to the background of room-temperature spectra for different temperatures. (b) The width of the bosonic mode as a function of temperature. (c) The shifts of mode position with temperature. (d) The variation of the gap size with temperatures.	112
7.7	The real part of the electron self-energy at a maximum $\text{Re}\Sigma(\omega)^{max}$ as a function of temperature for bare Bi2212, Zn-Bi2212, and Ni-Bi2212 in an ARPES study. And the spin susceptibility χ'' of bare YBCO, Zn-YBCO, and Ni-YBCO in an inelastic neutron scattering study. (Terashima et al., 2006)	114
8.1	A summary of the center frequency of the bosonic mode (Ω_{mode}) verses the HTSC transition temperature (T_c), based on the optical studies. The dashed line shows a linear fit.	119

List of Tables

2.1	The different combinations of the light source, the beamsplitter, the IR window and the detector for the reflectance measurements in the four different frequency regimes.	27
4.1	The dimensions of SRRs #1 and SRRs #2, the length L , the gap width G and the ring width W for the outer and inner rings, measured with the SEM. The values are in nm.	59
5.1	Parameters of the Drude-Lorentz model fit at different temperatures for the $\text{YBCO}_{6.35}$ sample.	81
5.2	Parameters of the Gaussian functions for the bosonic mode ($\text{PK}(\Omega)$) and the Heaviside step functions for the broad background ($\text{BG}(\Omega)$) in $I^2\chi(\Omega)$ at different temperatures.	90

Chapter 1

Introduction and Motivation

Optical spectroscopy is a powerful tool for the experimental investigation of the physical properties of a variety of materials. In our laboratory, with different combinations of the light source, the beamsplitter, the infrared (IR) window and the detector, we are able to cover a wide energy range, from the far infrared (FIR) up to the ultraviolet (UV). Here we use optical spectroscopy to probe intermediate-energy electronic excitations in the well-known high-transition-temperature superconductors (high- T_c superconductors or HTSCs) as well as the electromagnetic properties of the 2D metamaterials, *i.e.* the negative refractive index materials (NRMs) that were discovered only a couple of years ago. As illustrated in Figure 1.1, many interesting physical phenomena of the HTSCs exist in the energy regime that the optical spectroscopy covers ($50\text{-}40,000\text{ cm}^{-1}$), such as the superconductor energy gap, the pseudogap, the phonons, the neutron resonance and etc.

Section 1.1 gives a brief introduction of the negative refractive index metamaterials, the motivations and the specific subjects of our studies. In section 1.2, a concise review of the extraordinary properties of the high- T_c superconductors is provided, particularly focused on the electron-boson spectral density (or bosonic spectral

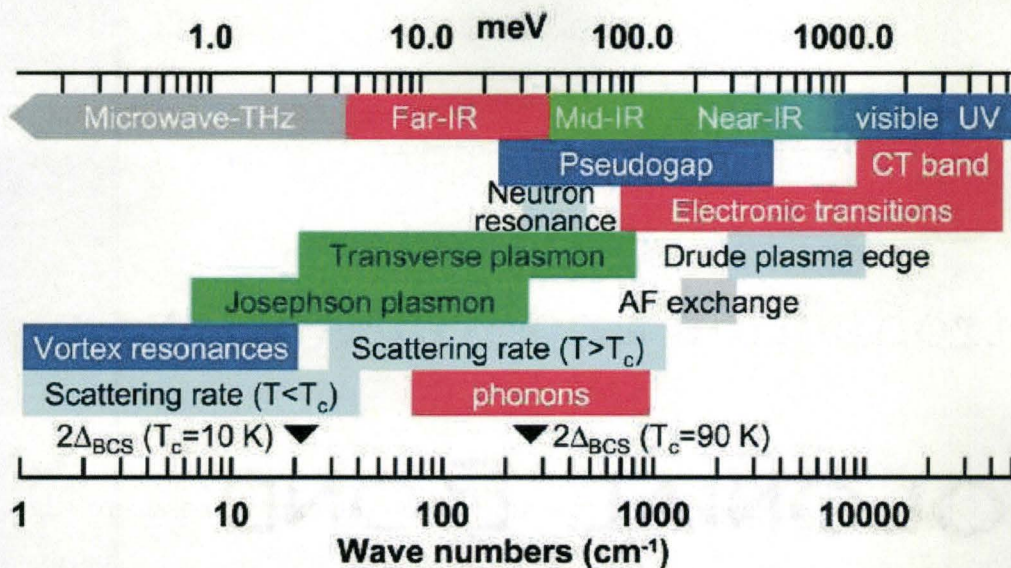


Figure 1.1 An illustration of the intermediate-energy electronic excitations in the high- T_c superconductors (Basov and Timusk, 2005).

density or bosonic spectrum) of the HTSCs.

1.1 Negative Refractive Index Metamaterials

The metamaterials are a group of novel artificial substances, which have sub-wavelength microscopic structures and thus can be treated effectively as homogeneous materials with an effective electric permittivity (ϵ) and an effective magnetic permeability (μ). The artificial structures determine their unusual electromagnetic properties, such as a negative refractive index or left-handed behavior, which is rare in naturally occurring materials.

The concept of the “left-handed substance” was first proposed by Veselago about 40 years ago (Veselago, 1968). He considered a case where a medium has simultaneously a negative relative dielectric permittivity ($\epsilon < 0$) and a negative relative

magnetic permeability ($\mu < 0$). Start with the Maxwell equations,

$$\vec{\nabla} \times \vec{E} = -\mu \frac{\partial \vec{H}}{\partial t} \quad (1.1)$$

$$\vec{\nabla} \times \vec{H} = \epsilon \frac{\partial \vec{E}}{\partial t} \quad (1.2)$$

where \vec{E} and \vec{H} are the electric and magnetic fields. For a plane harmonic wave $\exp[i(\vec{k} \cdot \vec{r} - \omega t)]$, we have $\vec{\nabla} \rightarrow i\vec{k}$ and $\partial/\partial t \rightarrow -i\omega$ and therefore, Equations 1.1 and 1.2 become

$$\vec{k} \times \vec{E} = \mu\omega\vec{H} \quad (1.3)$$

$$\vec{k} \times \vec{H} = -\epsilon\omega\vec{E}. \quad (1.4)$$

For ordinary optical materials with $\epsilon > 0$ and $\mu > 0$, we obtain the well-known right-handed triad $\vec{E} \times \vec{H} \propto \vec{k}$ from Equations 1.3 and 1.4. However, if both ϵ and μ are negative, \vec{E} , \vec{H} and \vec{k} form a left-handed triad $\vec{E} \times \vec{H} \propto -\vec{k}$, which means the directions of light propagation of energy, the Poynting vector $\vec{S} = \vec{E} \times \vec{H}$, and phase \vec{k} are reversed. Meanwhile, the wave vector \vec{k} relates to the refractive index n through $n\hat{n} = c/\omega\vec{k}$, where \hat{n} is the unit vector along $\vec{E} \times \vec{H}$. Whenever \vec{k} is in the opposite direction of $\vec{E} \times \vec{H}$, n becomes negative. Therefore, Veselago concluded that a negative refractive index or a left-handed behavior would happen if a substance had simultaneously a negative ϵ and a negative μ . Furthermore, he deduced a series of unusual electromagnetic phenomena in negative refractive index media, for example, a reversed Doppler shift and a obtuse angle of the Cerenkov radiation, due to the fact that the wave vector \vec{k} is anti-parallel to the Poynting vector. Another more straightforward optical effects due to the negative refractive index one would think of is anomalous refraction, which has been considered as a criterion for experimental

verifications of the existence of the negative refractive index (Shelby et al., 2001, Chen et al., 2004). As we know, when a light is incident onto the interface of two media having different refractive indices n_1 and n_2 , the beam is bent in a way that obeys Snell's law,

$$n_1 \sin \theta = n_2 \sin \phi, \quad (1.5)$$

where θ and ϕ are the angles of incidence and refraction. If $n_1 > 0$ and $n_2 > 0$, the refracted light is on the other side of the surface normal as shown in Figure 1.2 (a). However, if $n_1 > 0$ and $n_2 < 0$, the angle of refraction becomes also negative, in other words, the refracted light is on the same side as the incident wave as seen in Figure 1.2(b). Note that, although the refraction at the interface of a positive and a negative medium is anomalous, it does not violate Snell's law. Despite the various interesting effects of the negative refractive index media predicted by Veselago, there is no naturally occurring material that has been found to have simultaneously a negative ϵ and a negative μ .

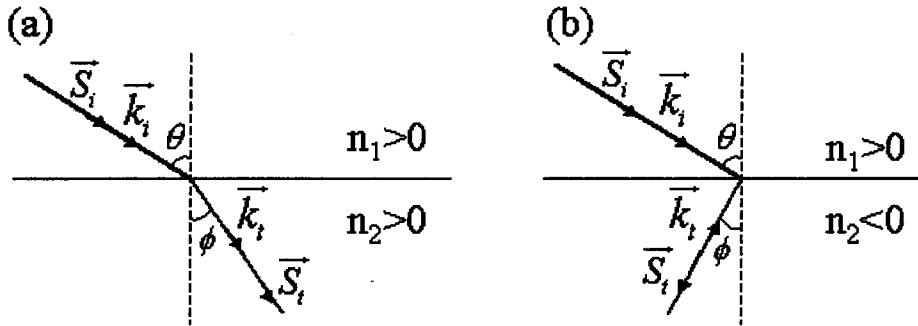


Figure 1.2 (a) The normal refraction for two media which both have positive refractive indices. (b) The anomalous refraction where the second medium has a negative refractive index, but doesn't violate Snell's law.

The materials that have negative electric permittivities are common in nature, because many metals have negative dielectric constant below their plasma frequencies

which are usually in the visible or even ultraviolet frequency ranges. However, the realizations of a negative magnetic permeability and an overlap of the frequencies where ϵ and μ become negative are challenging. It was not until 1999 that Pendry *et al.* suggested an array of double-ring split-ring resonators (SRRs) as one of the candidates that have negative μ , where each resonator consists of two concentric metallic circles with small gaps in each ring as well as between the two rings (Pendry *et al.*, 1999), as shown in Figure 1.3. When the magnetic field component of an incident electromagnetic wave is perpendicular to the SRRs plane, a magnetic resonance is excited and if the resonance is strong enough, it will achieve a region where μ becomes less than zero as seen in Figure 1.3. The magnetic resonance is associated with an LC resonance due to the capacitance and inductance of the SRR structure, so that the resonance frequency is determined by the dimensions of one SRR element. Since the materials having negative ϵ and those having negative μ are both becoming available, in 2000, Smith *et al.* demonstrated that a composite medium, which is a combination of the SRRs and continuous metallic wires, exhibit simultaneous negative ϵ and μ in the microwave regime (Smith *et al.*, 2000). A year after that, Shelby *et al.* fabricated a prism made of this composite medium and verified experimentally the anomalous refraction in a left-handed substance at a frequency of 10 GHz.

One of the most important applications of the negative refractive index metamaterials is for building the superlens. The best resolution of a conventional lens is of the order of the wavelength of the incident light due to the diffraction limit where the evanescent waves that contain the sub-wavelength information of the objective decay exponentially in the positive refractive index media. However, the negative refractive index metamaterials have been verified to give rise to an exponential magnification of the amplitude of the evanescent waves and thus have much higher resolutions than the conventional lenses.

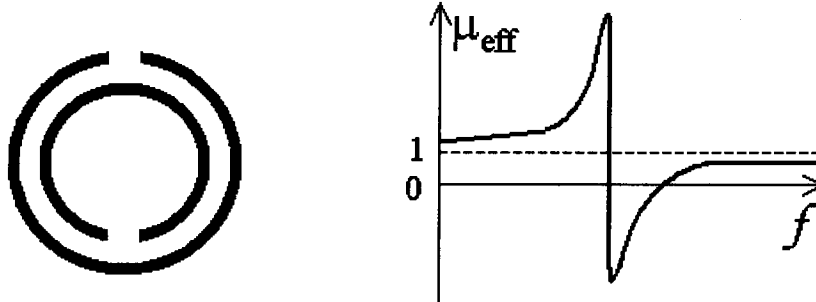


Figure 1.3 The schematic diagrams of one element of the double-ring split-ring resonator array (Left) and the magnetic resonance in it when the magnetic component of the incident light is normal to the array (Right).

In the previous designs of the NRMs, the metallic continuous wires were combined with the SRRs to achieve a negative refractive index because they provide $\epsilon < 0$ below the plasma frequency. However, the wire medium has certain disadvantages as indicated earlier by Schurig *et al.* (Schurig *et al.*, 2006), such as the requirement of an unbroken electrical connection between unit cells, which would be challenging in building contoured devices. But note that, the SRR has electric resonances as well, which result in $\epsilon < 0$ at certain frequencies. One of the electric resonances is from the parallel currents in the two parallel arms of the SRR (Koschny *et al.*, 2004), and another one is related to the electric-field excited LC resonance via asymmetry (Linden *et al.*, 2004, Padilla *et al.*, 2006).

In our studies, we deduced that a double-ring SRR array could have a negative refractive index ($n < 0$) due to a combination of the magnetic and electric resonances of the SRR structure itself, without the aid of additional continuous metallic wires. We experimentally studied the resonances of arrays of double-ring SRR with dimensions of hundreds of nanometers in the mid-infrared frequencies. We observed that the magnetic resonance from the inner ring and the electric resonance from the two

parallel arms of the outer ring exist at similar frequencies in our sample. Although there have been a number of studies on the SRRs over a wide frequency range (Shelby et al., 2001, Padilla et al., 2006, Smith et al., 2000, Linden et al., 2004), there are few studies on the DOUBLE-ring SRRs in the mid-infrared region and, to our knowledge, there is no reported observation of the magnetic resonance from the inner ring in the transmission spectra of a DOUBLE-ring SRR array. From our numerical investigations, we confirmed that the coexistence of the magnetic resonance from the inner ring and the electric resonance from the outer ring could give rise to a left-handed behavior in a DOUBLE-ring SRRs. Furthermore, based on the same idea of a combination of the resonances of the SRR itself as in our first argument, we proposed a simplified structured metamaterial which is composed of single-ring SRRs only, with no metallic wires involved. Numerical studies show that this simple structure has pronounced left-handed behavior due to the magnetic resonance in one of the single-ring SRRs and the electric resonance (E -field excited LC resonance) in the other in each unit cell. Note that, in our designs, we carefully avoided the coupling between the electric and magnetic responses (Padilla et al., 2006), which means the electric and magnetic resonances corresponding to the left-handed behavior are excited by the electric and magnetic fields separately. While there have been studies on the left-handed behavior of the metamaterials composed of resonators only without metallic wires (Chen et al., 2004), the resonances of the metamaterial we discuss in this paper are at much higher frequencies.

1.2 Bosonic Spectral Density of HTSCs: Probed by Optical Spectroscopy

Although discovered more than 20 years ago, the high- T_c superconductors are still attractive to scientists since the underlying mechanisms are not completely clarified yet.

Since the discovery of superconductivity in 1911 (Onnes, 1911), many conventional metals or alloys (*e.g.* Hg, Al, Zn, Nb₃Al, *etc.*) have been found to undergo a phase transition to an ordered superconducting state (having exactly zero dc resistivity and perfect diamagnetism) when cooled to below certain temperatures T_c , the critical temperature or the transition temperature. However, the superconducting transition temperatures were fairly low with a highest value of 23 K in Nb₃Ge, which is much lower than the boiling point of liquid Nitrogen (77 K). It was 75 years later when Bednorz and Muller made a great breakthrough in the history of superconductivity and discovered a new class of superconducting materials which exhibit much higher critical temperatures (Bednorz and Müller, 1968). The high- T_c superconductors are essentially different families of copper oxides (cuprates), *e.g.* La_{2- x} Ba _{x} CuO₄ ($T_c \approx 30$ K), the firstly discovered HTSC and HgBa₂Ca₂Cu₃O_{8+ δ} (Hg1223) which has the highest T_c (~ 135 K, under ambient pressure (Schilling et al., 1993)) to date. One of the striking characteristics of the HTSCs compared to the conventional superconductors is their layered crystal structure, where the conducting CuO₂ planes are well separated by the insulating layers which are considered as the charge reservoir layers, as seen in Figure 1.4. Meanwhile, different families of the HTSC cuprates may contain different number of CuO₂ layers in one unit cell.

Unlike the conventional superconductors, the high- T_c cuprates have variable critical temperatures with a variation of the charge carrier concentration or doping

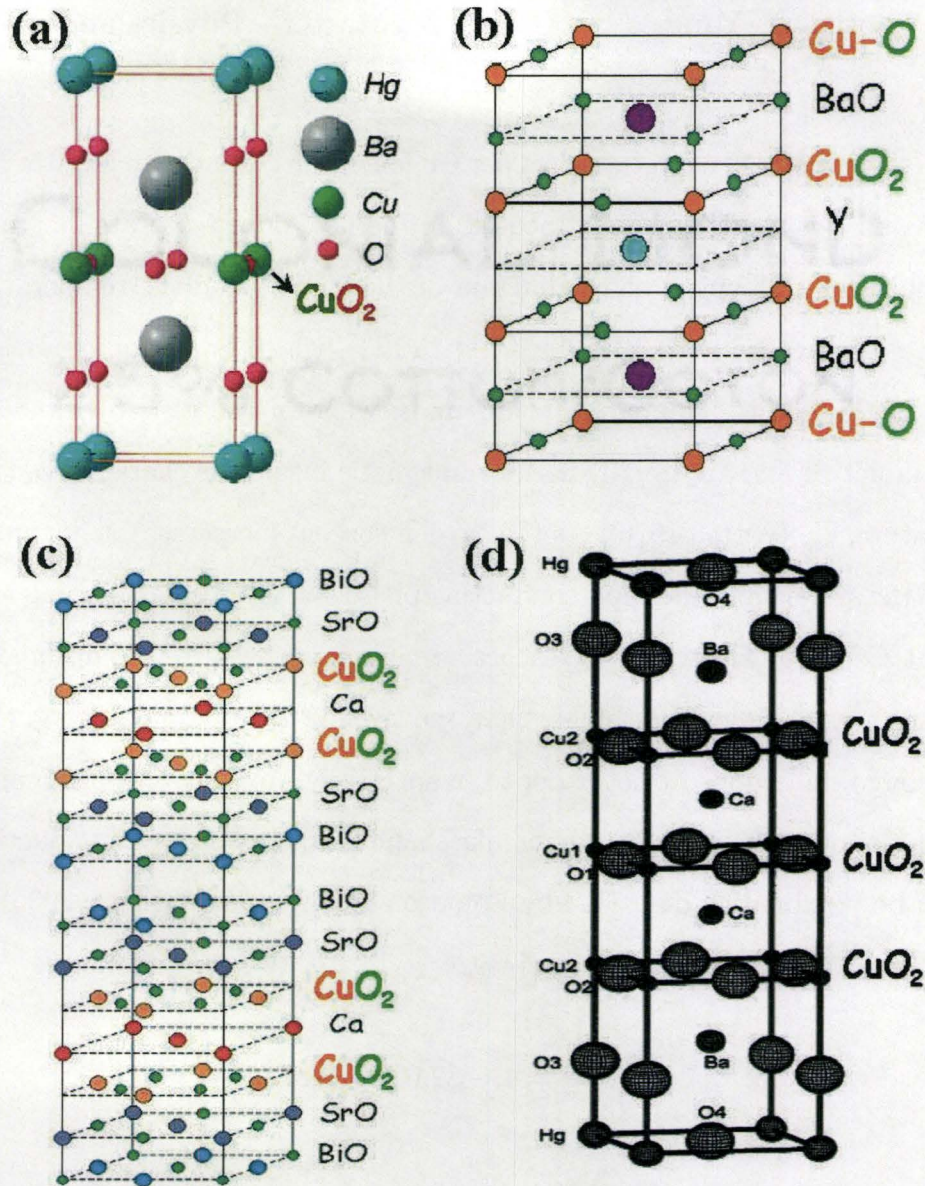


Figure 1.4 Structures of unit cells of high- T_c cuprates with different number of CuO_2 layers. (a) Monolayer $\text{HgBa}_2\text{CuO}_{4+\delta}$ (Zhao et al., 2006); (b) Bilayer $\text{YBa}_2\text{Cu}_3\text{O}_7$ (Note. From Hoffman Lab, Harvard University. (2007). Retrieved from <http://hoffman.physics.harvard.edu/research/SCmaterials.php>); (c) Bilayer $\text{Bi}_2\text{Sr}_2\text{CaCu}_2\text{O}_{8+\delta}$ (Note. From Hoffman Lab, Harvard University. (2007). Retrieved from <http://hoffman.physics.harvard.edu/research/SCmaterials.php>); (d) Trilayer $\text{HgBa}_2\text{Ca}_2\text{Cu}_3\text{O}_{8+\delta}$ (McGuire, 2001).

level, p (the number of charge carriers per Cu ion). The carriers can be either electrons or holes and this thesis is mainly focused on the hole-doped cuprate systems. Figure 1.5 demonstrates a typical phase diagram of the HTSCs and the temperature scales are plotted in accord with $\text{YBa}_2\text{Cu}_3\text{O}_{6+\delta}$ (Y123), which is one of systems that are studied in this thesis. The parent compounds, where $p = 0$ ($\delta = 0$), cannot become superconducting and are usually antiferromagnetic insulators characterized by a Néel temperature, T_N (Kittel, 1976). As the oxygen content increases, the dopant provides holes to the system and the superconducting phase starts at certain doping level of the holes. At a doping level where T_c reaches a maximum, the system is optimally doped. In regions where p is lower or higher than the level for the optimal doping, the system is considered underdoped or over-doped, respectively. As displayed in Figure 1.5, the T_c as a function of doping is in a dome-like shape (namely, the superconducting dome) and can be proximately described by Equation 1.6 (Honma and Hor, 2006), which is conjectured to be universal for the HTSCs.

$$\frac{T_c}{T_c^{max}} = 1 - 82.6(p - 0.16)^2 \quad (1.6)$$

What make the phase diagram of the HTSCs more complicated are the anomalous normal states, where $T > T_c$. Instead of showing a Fermi-liquid behavior (Kittel, 1976) of a simple metal, the normal states of the cuprates exhibit unusual and different behaviors at different doping levels. For example, below a characteristic temperature T^* (normally, $T^* > T_c$ in the underdoped regimes), the normal states have a gap, namely the pseudogap, opening up in the density of states of quasiparticles in the vicinity of the Fermi levels. The size of the pseudogap Δ_{pg} decreases with the hole doping level and the pseudogap seems to disappear at the optimal doping as seen in Figure 1.5. Although whether the pseudogap is gone or not at the optimal doping

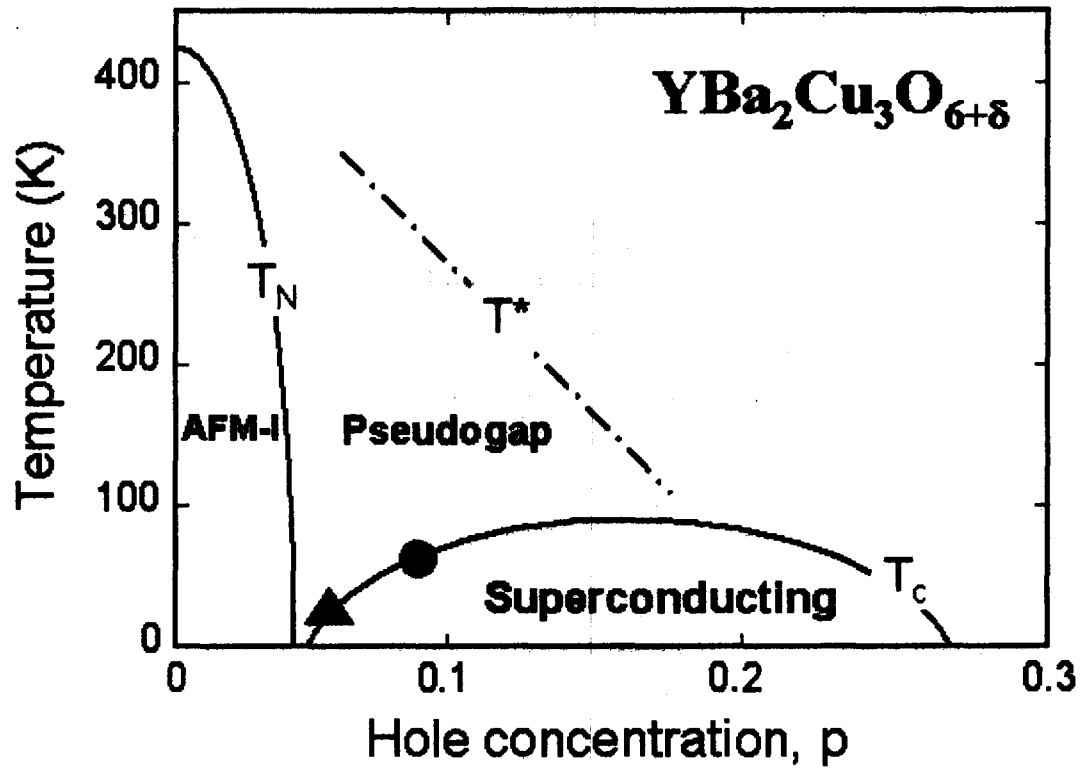


Figure 1.5 The phase diagram of the $\text{YBa}_2\text{Cu}_3\text{O}_{6+\delta}$ system, a representative of the HTSCs families. (Refer to (Ahn et al., 2003)) The circular and triangular symbols represent two of the underdoped Y123 samples that are discussed in this thesis.

level and beyond is still under investigation, in this thesis, the arguments for the optimally doped cuprate systems are made by assuming that there is no pseudogap or the effects of the pseudogap are very small. We do take the pseudogap contributions into account in the analysis of the two underdoped Y123 systems represented by the symbols in Figure 1.5.

The most debated issue of the HTSCs is the nature of the pairing mechanism of the charge carriers in the superconducting condensate. The answer for the conventional superconductors has been successfully given by the famous BCS theory (Bardeen et al., 1957) established in 1957, which describes the superconducting electrons as Cooper pairs that have zero total spin and momentum in each pair, where the electric repulsions are overcome by the interaction between the electrons and the phonons (the quantized lattice vibrations). An electron-phonon spectral function $\alpha^2F(\Omega)$ was a good measure of the electron-phonon interactions in the conventional superconductors, which was obtained via a numerical inversion of the self-energy measured in the tunneling and the optical spectroscopy experiments, based on the Migdal-Eliashberg theory (McMillan and Rowell, 1969, Carbotte, 1990, Farnworth and Timusk, 1976). However, when it comes to the HTSCs, the classic BCS theory failed to explain those unique phenomena in the cuprates. Whether the paired electrons are formed still through the interactions with the phonons or via other channels, *e.g.* via the interactions with the magnons (the magnetic excitations or the spin fluctuations) is puzzling.

In order to get pieces of information on the pairing glue of the HTSCs, we examine carefully the optical self-energy spectra of the cuprates as a function of temperature, doping, number of the CuO_2 layers as well as the magnetic and non-magnetic substitutions and endeavor to extract the electron-boson spectral function $I^2\chi(\Omega)$ through both an analytical and a numerical method. This thesis deals with

the high T_c cuprate systems including the moderately and highly underdoped bilayer Y123, the monolayer and trilayer Hg based cuprates, namely $\text{HgBa}_2\text{CuO}_{4+\delta}$ (Hg1201) and $\text{HgBa}_2\text{Ca}_2\text{Cu}_3\text{O}_{8+\delta}$ (Hg1223), the Ni- and Zn-doped bilayer $\text{Bi}_2\text{Sr}_2\text{CaCu}_2\text{O}_{8+\delta}$ (Bi2212), where the optical results are also compared to those of other techniques, such as the magnetic neutron scattering and the angle-resolved photoemission spectroscopy (ARPES).

Sections 1.2.1 and 1.2.2 provide introductions to the analytical and numerical methods that are used in this thesis, along with descriptions of the background of the studies on the above cuprate systems.

1.2.1 Model Fits Based on Sharapov's Formula

For the highly underdoped Y123 system, we adopt an analytic formula derived by Sharapov (Sharapov and Carbotte, 2005) to relate the measured optical scattering rate $1/\tau(\omega)$, the imaginary part of the complex optical self-energy $\Sigma^{op}(\omega)$ to the electron-boson spectral function $I^2\chi(\Omega)$ for the normal states.

Back to the year of 1971, Allen (Allen, 1971) successfully provided an analytic formula to relate the optical scattering rate to the electron-phonon spectral function for the conventional superconductors. Twenty years later, Shulga *et al.* generalized Allen's formula to finite temperatures (Shulga et al., 1991). While, in both Allen's and Shulga's formulas, the density of states of the quasiparticles is assumed to be constant in the vicinity of the Fermi levels, this is not true for the normal states of the HTSCs, where a pseudogap exists. In order to deal with the energy-dependent electronic density of states, Sharapov *et al.* (Sharapov and Carbotte, 2005) extended the previous studies and developed a formula which can be applied to analyze the optical scattering rate of the the HTSCs in the normal states. Our previous studies

on a moderately underdoped Y123 system $\text{YBa}_2\text{Cu}_3\text{O}_{6.50}$ ($\text{YBCO}_{6.50}$) (Hwang et al., 2006b) showed that the bosonic spectra are dominated by a bosonic mode located around 31 meV with a strong temperature dependent mode intensity, which are consistent with the neutron scattering studies. The recent neutron studies on the highly underdoped $\text{YBa}_2\text{Cu}_3\text{O}_{6.35}$ ($\text{YBCO}_{6.35}$, $T_c=18$ K) (Stock et al., 2006) indicated that the 31 meV mode is gone and is replaced with a central mode at 0 meV. The motivation of our optical study on the highly underdoped Y123 sample, which has the same hole doping level as the sample studied with neutrons, is to compare the bosonic mode to the central mode in the neutron studies and also to compare the optical properties between the two underdoped Y123 systems.

Distinguished from other cuprates, Y123 has an additional Cu-O chain forming as the oxygen content increases as seen in Figure 1.4. Figure 1.6 shows the development of the Cu-O chains with the variation of the oxygen content $6+\delta$. The parent compound has no Cu-O chains and is a Mott insulator. Complete chains form along the b -axis at $\delta=1$ in the ortho-I phase. An ortho-II phase appears when $\delta=0.50$, which has alternating full and empty Cu-O chains and a doubled unit cell along the a direction. When the oxygen content is $\delta=0.35$, the Cu-O chains are not completely ordered in the b direction, but the degree of the ordering determines the hole doping level in the nearby CuO_2 planes and thus tunes the transition temperature T_c . As indicated in a previous study (Veal et al., 1990), the ordering of the Cu-O chains can be controlled by the annealing temperatures. The original $\text{YBCO}_{6.35}$ obtained from the crystal grower had a higher T_c than what we expected, via the annealing process described in Chapter 5, we successfully tuned the T_c to a desired value of 18 K.

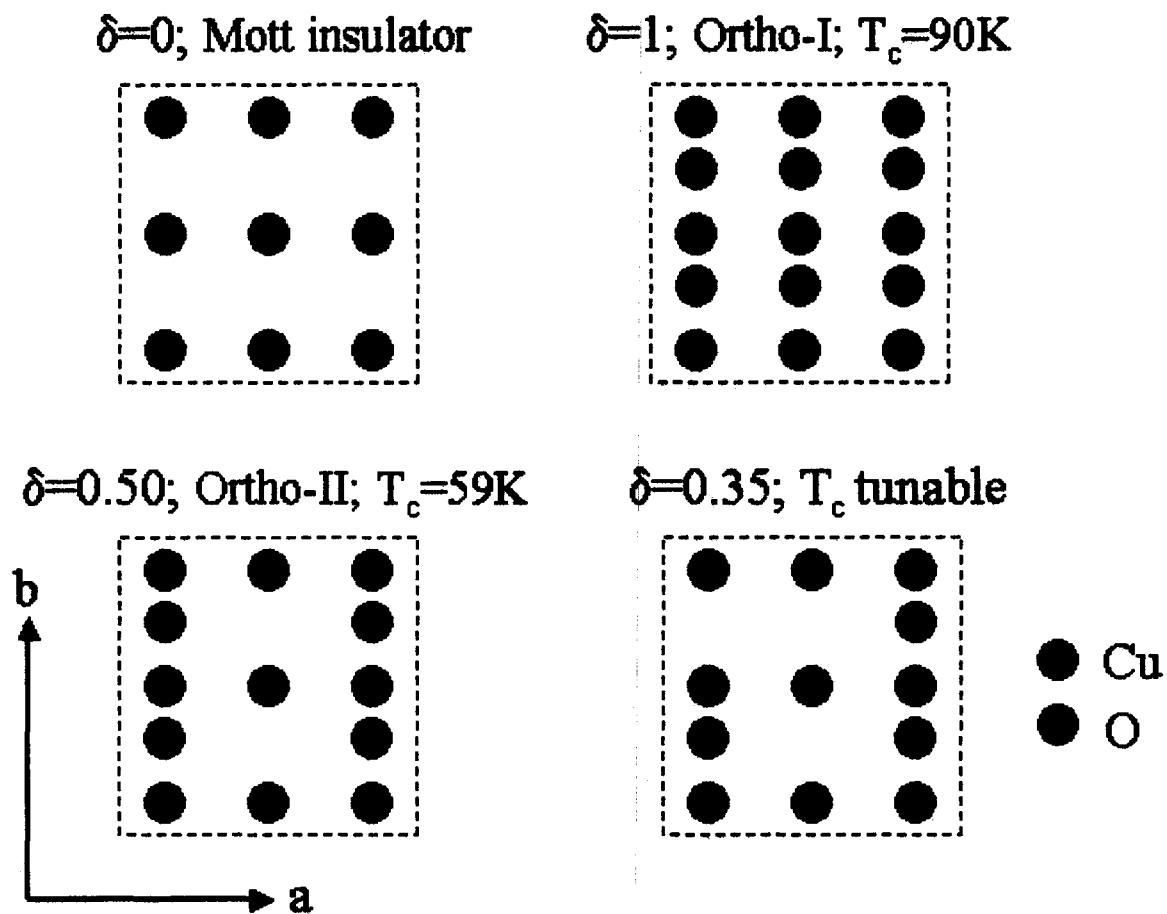


Figure 1.6 A schematic diagram of the evolution the Cu-O chains in $\text{YBa}_2\text{Cu}_3\text{O}_{6+\delta}$ with a variation of the oxygen content $6+\delta$.

1.2.2 Eliashberg Inversion Based on a Maximum Entropy Method

The Eliashberg inversion technique based on a maximum-entropy method applied to extract the bosonic spectral density $I^2\chi$ from the optical self-energy spectra of HTSCs is developed by Schachinger *et al.* (Schachinger et al., 2006). This method works well in both the superconducting and normal states of HTSCs, but without a consideration of the pseudogap in the normal states. Therefore, the numerical inversion method is adopted only for the optimally or nearly optimally doped cuprate systems, *i.e.*, Hg1201 ($T_c \sim 91$ K), Hg1223 ($T_c \sim 130$ K), Zn- and Ni-substituted Bi2212 ($T_c \sim 85$ -80 K).

HgBa₂CuO_{4+ δ} (Hg1201) has the simplest structure in the family of mercury-based high- T_c cuprates HgBa₂Ca _{$n-1$} Cu _{n} O_{2 $n+2+\delta$} , where $n = 1$ and there is only one CuO₂ plane in each unit cell as seen in Figure 1.4. The Hg-based cuprates are notable for their high T_c 's, such as Hg1223 ($n = 3$) which has a highest T_c so far around 130 K at the optimal doping. The Hg1201 sample is nearly optimally doped and the T_c is around 91 K. In this thesis, the optical properties of the single layered Hg1201 will be compared with those of the triple layered Hg1223.

Moreover, inelastic neutron scattering experiments revealed the existence of a magnetic resonance mode corresponding to the spin excitations at low temperatures $T < T_c$ in the bilayer cuprates Y123 (Mook et al., 1993, Fong et al., 1995, Mook et al., 1998, Dai et al., 1999, Stock et al., 2005) and Bi2212 (Fong et al., 1999, He et al., 2001) and also in the monolayer copper oxide Tl₂Ba₂CuO_{6+ δ} (He et al., 2002). However, for another monolayer cuprate La_{2- x} Sr _{x} CuO₄ (LSCO), recent neutron studies showed that the spin excitation spectrum has two components. In addition to the mode that was previously observed in other cuprates, a mode appears at lower energy (Vignolle

et al., 2007). Note that LSCO has a much lower $T_c \sim 30$ K at optimal doping than other cuprate systems. The electron-boson spectra of Y123, LSCO and Bi2212 extracted from the optical self-energy have demonstrated excellent agreement with the neutron data (Hwang et al., 2006a, 2008a, 2007b). In this thesis, we study the self-energy spectrum of the Hg1201 sample, which is another monolayer cuprate, and extract the electron-boson spectral function with the numerical inversion. The optical results are compared with the preliminary inelastic neutron scattering measurements on Hg1201 (Zhao et al., 2006).

The optical studies on the impurity doped Bi2212 samples are motivated by a recently published ARPES experiment (Terashima et al., 2006) on the so called "magnetic isotope" effects in the high- T_c cuprates which is a magnetic analogue of the isotope effects in the conventional superconductors. The direct experimental support for the phonon mediated formation of the electron pairs in the conventional superconductors was the isotope effects, where the change of the nuclear masses altered the transition temperature of the superconductors. For the high- T_c superconductors, a study on the substitution effects of the copper atom with the magnetic and non-magnetic atoms, that could affect the magnetic environment but not the lattice vibration would give us some insights into the role of the magnetic resonance in the superconductivity. Terashima *et al.* substituted copper atoms (spin-1/2) in the CuO_2 planes of Bi2212 with a small amount of non-magnetic Zn (spin-0) and magnetic Ni (spin-1) atoms and observed remarkable changes in the electron self-energy that are consistent with those of the magnetic excitations (Sidis et al., 2000) and thus deduced the importance of the spin fluctuations in pairing the electrons in the high- T_c cuprates. In this thesis, we study the Zn- and Ni- substituted Bi2212 samples from the same source as the ARPES by using the optical spectroscopy and examine the differences among the extracted Bosonic spectra of the bare and impurity-doped

systems. Comparisons are made with the ARPES and neutron studies.

1.3 Thesis Outline

This thesis consists of 8 chapters. Chapter 2 elaborates on the optical experiments, including Fourier transform infrared spectrometry, reflectance and transmittance measurements. A brief review of the theoretical background of the optical response of the solids and descriptions of the ways of analysis for both the HTSCs and the metamaterials are given in Chapter 3. Chapter 4 focuses on the optical studies of the metamaterials and explains in details the sample fabrications, the experimental results and the numerical simulations. The main results of this part have been published recently (Yang et al., 2008). The investigations of the optical properties of the high- T_c cuprate systems are provided in the following three chapters (Chapter 5-7). Finally, in Chapter 8, conclusions are derived. At the end of the thesis, the appendix provides the Matlab programmes that are used for the model fits.

While I did most of the research work included in this thesis, I would like to acknowledge the contributions of the colleagues as well as people from other research groups.

For the project on SRRs, I fabricated the samples and performed the optical measurements with some assistance from Dr. J. Hwang. The simulations were completely done by myself. The manuscript of the published paper on SRRs was written by me with editorial help from Dr. T. Timusk. The single crystal of YBCO_{6.35} was grown by Dr. Ruixing Liang at University of British Columbia. The sample annealing, optical measurements, data analysis as well as model fittings were carried out by myself. The Hg1201 sample was grown by D. Colson at CEA, Saclay. Dr. J. Hwang provided some help with the optical measurements. I did data analysis and

produced the optical constants, including the optical scattering rate on which Dr. E. Schachinger at Graz University of Technology did the maximum entropy inversions. The Zn- and Ni-doped Bi₂Te single crystals were provided by Prof. Kazuo Kadowaki's research group at University of Tsukuba. The optical measurements and data analysis were performed by myself and the maximum entropy inversions were done by Dr. Schachinger.

Chapter 2

Optical Measurements

2.1 Introduction — FT-IR spectrometry

The reflectance and transmittance measurements of the high- T_c superconductors as well as the metamaterials were carried out with the use of a commercial Fourier transform infrared (FT-IR) spectrometer, *i.e.* Bruker IFS 66v/S. The reflectance and transmittance stages have been customized in order to facilitate a variety of advanced measurements of reflectance as a function of temperature and polarization using *in situ* evaporation automation. The interferometer compartment, which is the most important part of the FT-IR spectrometer, is essentially a Michelson type as shown in the right part of Figure 2.1. It primarily comprises an infrared light source, a beamsplitter, two mutually perpendicular plane mirrors (one is fixed while the other one is movable) and a couple of concave mirrors. The light from the infrared source projects onto the beamsplitter after collimation by two of the concave mirrors. Ideally, the beamsplitter is 50% transmissive which results in half of the light traveling to the movable plane mirror with the other half going to the fixed plane mirror. The reflected beams are recombined at the concave mirror G, enter the beam focusing

compartment, focused on the sample in the sample chamber and finally recorded by the detector, either through the reflection or the transmission path.

In the simplest case when the light source is monochromatic (frequency k , in wavenumbers), as the movable mirror travels along the axis perpendicular to its plane, the path difference (x) between the two of the recombined beams would be changing, as well as the optical path difference (kx), which results in a variation of the phase shift between the recombined beams. As the mirror moves back and forth, the recombined beams are in and out of phase periodically and an interference pattern is recorded by the detector. The intensity of the recombined beams as a function of the path difference ($I(x)$), *i.e.* the interferogram, is a cosine function for a monochromatic source. While, for a continuous infrared source, the interferogram is no longer a simple sinusoidal wave, but proportional to an intensity function as shown in Figure 2.2 (a). We define $W(x)$ as $W(x) = 2I(x) - I(0)$, where $I(0)$ is the intensity for zero path difference. If we do a Fourier transform on $W(x)$ (Fowles, 1989),

$$G(k) = \frac{1}{\sqrt{2\pi}} \int_{-\infty}^{\infty} W(x)e^{-ikx} dx, \quad (2.1)$$

we end up with a power spectrum $G(k)$, the intensity as a function of the frequency of incident light. As seen in Figure 2.2 (b), the profile of the power spectrum describes a black body radiation from the infrared light source. For an interferogram of N data points, the integration in Equation 2.1 becomes a summation for each discrete point in the power spectrum and the total number of the computations needed to produce a spectrum of N points would be in the order of N^2 . Practically, a fast Fourier transform algorithm developed by Cooley and Tukey (Griffiths and de Haseth, 2007) is adopted to reduce the number of operations substantially to the order of $N \log N$.

All the experiments have been done within the rapid-scanning mode of the

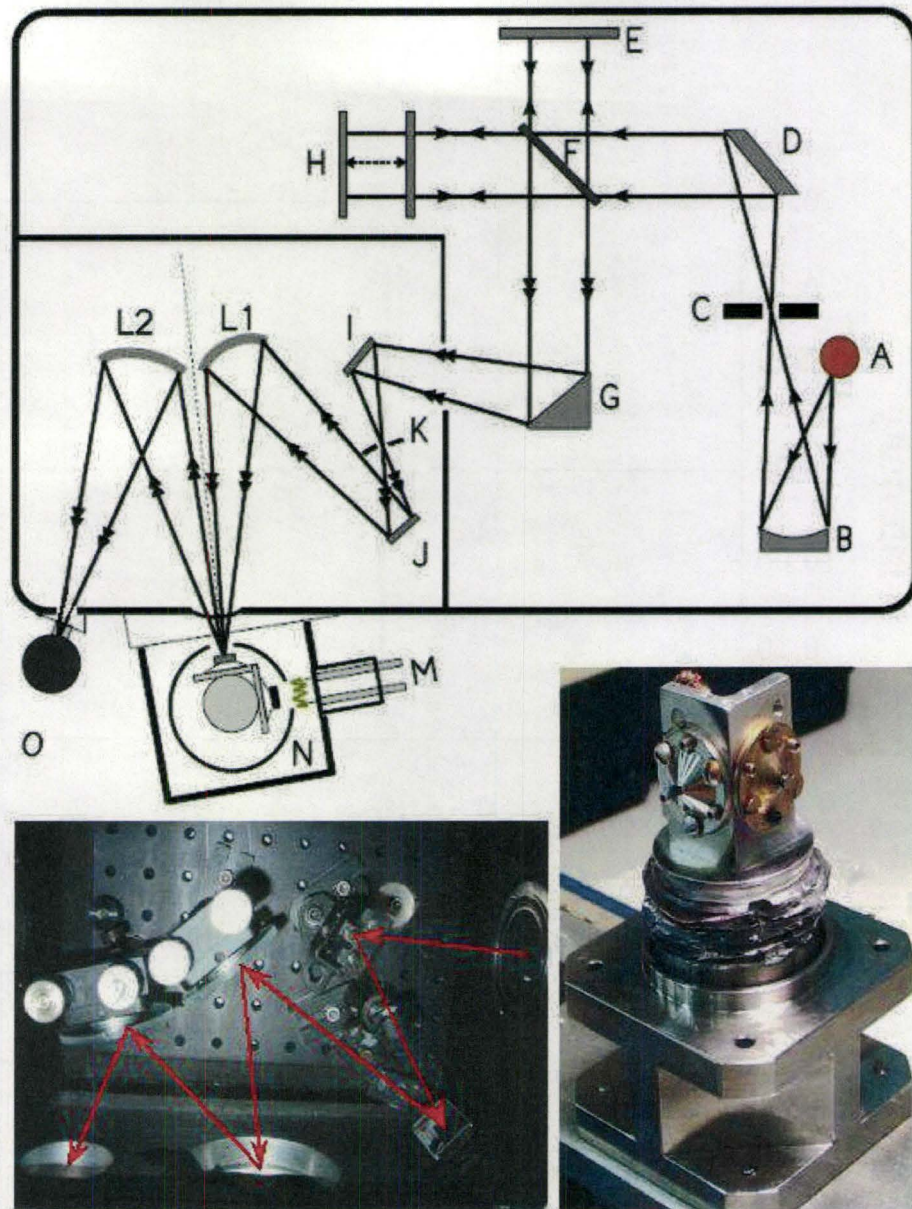


Figure 2.1 Top panel: A schematic diagram of the FTIR spectrometer with the reflectance measurement setups. (A) light source; (B) concave mirror; (C) aperture; (D) concave mirror; (E) fixed plane mirror; (F) beamsplitter; (G) concave mirror; (H) movable plane mirror; (I, J) plane mirror; (K) aperture; (L1, L2) toroidal mirrors; (M) evaporator apparatus; (N) sample stage; (O) detector. Bottom panels: Photographs of the beam focusing compartment (Left) and the sample stage (Right).

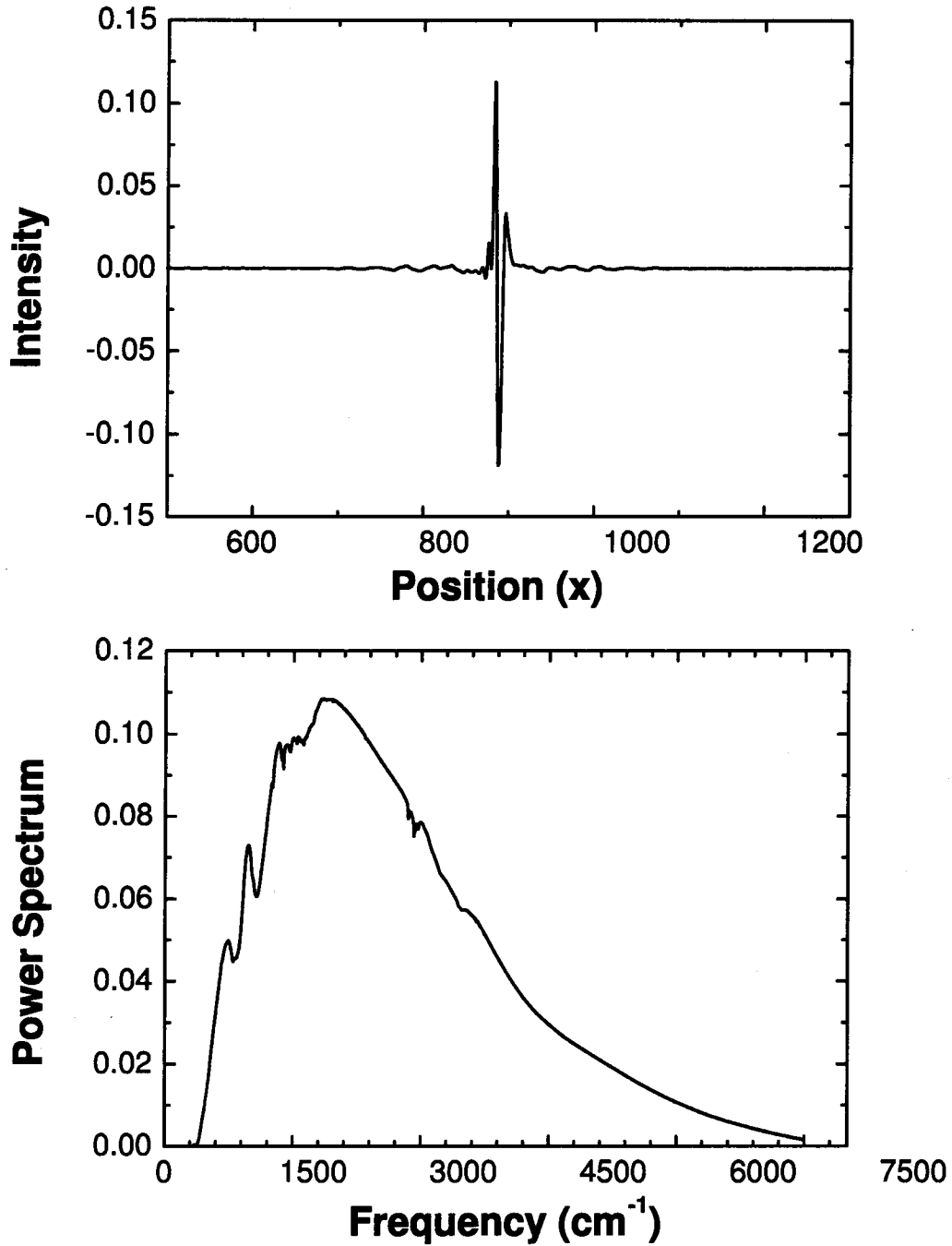


Figure 2.2 The typical interferogram and the power spectrum for a mid-infrared light source.

FT-IR spectrometer, where the moving mirror is scanning at a constant velocity, 0.32 cm/s in our measurements. Repeated scans (usually 100~400 scans) have to be taken and the averaged interferogram is Fourier transformed into the spectrum. Thereby, the signal to noise ratio of the spectrum is increased by the square root of the number of scans, due to the coherence of the signal and the randomness of the experiment noise.

The modulated beams emerging from the interferometer compartment are used for both the reflectance and the transmittance measurements. In Section 2.2 and 2.3, the setups and the important techniques that have been applied to the reflectance and transmittance measurements are explained, respectively. Last but not least, a description of the infrared polarizers used for the anisotropic material studies is presented in Section 2.4.

2.2 Reflectance Measurements

2.2.1 Setups of Reflection Spectrometry

Reflection spectrometry was used for investigating the optical properties of HTSC materials over a wide frequency range and as a function of temperature. The high- T_c cuprates have layered structures and have significantly different properties between the 2D ab -plane (the CuO_2 plane) and the c -axis. In this thesis, we primarily focused on the ab -plane properties of HTSCs. Figure 2.1 shows a schematic diagram of the layout for the reflectance measurement. The mirrors in the beam focusing compartment are arranged in order to realize a small angle of incidence, close to normal incidence, for purpose of the ab -plane studies. An infrared window is located between the sample chamber and the spectrometer in order to isolated the sample

chamber to achieve a high vacuum condition for low-temperature measurements. A continuous ^4He flow cryostat (R. G. Hansen & Associate), which is not shown in Figure 2.1, is attached to the sample stage through a couple of flexible silver bands for low-temperature studies. A direct attachment of the sample stage to the cryostat would cause an unwanted movement of the sample due to thermal expansions. A detailed description of the isolation of the sample stage from the ambient room temperature can be found in the M. Sc. thesis of J. Yang (Yang, 2005). A temperature as low as 20 K can be reached with the current setup. An evaporation apparatus is attached to the sample chamber for an *in situ* evaporation technique (Homes et al., 1993), which is described in Section 2.2.3.

On the sample stage, the sample and a piece of stainless steel mirror are mounted on the tips of two polished brass cones, respectively, which are arranged in an L-shape, as seen in Figure 2.1. The stainless steel mirror has a polished circular surface with a diameter of 2 mm and is used as an intermediate reference for a correction of the drift of the instrument with time and temperatures. With a rotation of the sample stage by 90 degrees, the power spectra of the light reflected from the sample (R_{sam}) and the stainless steel reference (R_{ref}) are measured successively by the detector. In the temperature-dependent measurements, certain changes of the area of the sample surface are expected during a large variation of temperatures, *i.e.* from 295 K to 27 K. And this would result in some errors in the measured temperature-dependent reflectance spectra if the beam spot of the incident light is smaller than the area of the sample surface, since different portions of the sample has been examined at different temperatures. Therefore, in our reflectance measurements, the incident light is always managed to cover the whole sample surface area (the whole reference area as well) and the superfluous light beam that is shined on the brass cone is just scattered away and does not reach the detector. Note that, the sample and the stainless steel

reference normally have different surface areas and that is one of the reasons why the known reflectance of the stainless steel cannot be used directly to calculate the absolute value of the reflectance of the sample. Hence, the stainless steel mirror is considered only as an intermediate reference and the final reference is a thin layer of gold evaporated onto the sample surface during the measurements, *i.e.* the *in situ* evaporation technique (Homes et al., 1993), a detailed description of which is present in the next section.

A wide energy range frequencies of the measured reflectance spectrum of a sample can be achieved by using the FTIR spectrometer, namely from 50 cm^{-1} up to $40,000 \text{ cm}^{-1}$. But the data of the wide-frequency spectrum have to be taken in four sets of measurements which cover four different energy regimes of the spectrum, *i.e.* the far-infrared (FIR), the mid-infrared (MIR), the near-infrared (NIR), the visible and ultraviolet. Four different combinations of the light source, the beamsplitter, the IR window and the detector are used to facilitate the measurements in different energy regimes, as listed in Table 2.1.

Table 2.1 The different combinations of the light source, the beamsplitter, the IR window and the detector for the reflectance measurements in the four different frequency regimes.

Frequency	Light Source	Beamsplitter	IR Window	Detector
FIR ($50\text{-}650 \text{ cm}^{-1}$)	Hg arc	$6\mu\text{m}$ Mylar (Coated with Ge)	Polypropylene	4K Bolometer
MIR ($400\text{-}6,000 \text{ cm}^{-1}$)	Globar	KBr (Coated with Ge)	KBr	77K MCT
NIR ($3,000\text{-}14,000 \text{ cm}^{-1}$)	Tungsten	UV(CaF_2)	KBr	77K MCT
NIR, VIS, UV ($12,000\text{-}45,000 \text{ cm}^{-1}$)	D ₂ lamp	UV(CaF_2)	KBr	PMT

2.2.2 The *In Situ* Evaporation Technique

In order to eliminate the size effects discussed previously and also to correct the geometrical effects due to rough sample surfaces, we applied an *in situ* evaporation technique developed by Homes *et al.*, (Homes et al., 1993). The procedures are listed as the followings. As mentioned in Section 2.2.2, at the beginning, the stainless steel mirror is used as the intermediate reference to obtain the ratio R_{sam}/R_{ref} at different temperatures we are interested in. And then, a uniform thin layer of metal (gold or aluminum, depending on the frequency regime studied) is evaporated onto the sample surface at room temperature by using the evaporator apparatus attached to the right side of the sample chamber, as shown in Figure 2.1, and the measurements at low temperatures are repeated on the Au or Al surface. The structure of the evaporator apparatus is quite straightforward. A tungsten filament about 1 cm long made from W wires is connected to the two electrodes of the evaporator. The W wires must be cleaned with the sand papers as well as acetone to remove the oxides on the surface of the tungsten before being made into filaments. Three short segments of thin Au or Al wires, each of which is about 7 mm long and with a diameter of 0.25 mm, are wrapped around the coils of the filament. A current running through the filament is slowly increased from 0 to nearly 2 A (1.5 A for aluminum) to let the gold pieces start to melt. Then the current is increased all the way to nearly 4 A (3.5 A for aluminum) and held for about 10 seconds for a complete evaporation of the gold pieces onto the sample surface. The thickness of the Au or Al layer coated onto the surface of the sample is estimated to be about 200 nm, which is thick enough to eliminate the unwanted reflection from the sample-Au (sample-Al) interface since the thickness of the metal is larger than its skin depth. On the other hand, the thickness of the evaporated metallic layer should not be too thick, for that would obscure any

fine roughness on the sample surface. The *in situ* evaporation technique is carried out in a vacuum condition of $\sim 10^{-6}$ Torr, and at a room temperature.

The power spectra of the reflected light from the coated sample (R_{coat}^{Au}) and the stainless steel mirror (R_{ref}) are measured to obtain the ratio (R_{coat}^{Au}/R_{ref}) at different temperatures. Finally, the absolute value of the reflectance of the sample is obtained through a simple relation as the following:

$$R_{sam}^{abs} = \left(\frac{R_{sam}/R_{ref}}{R_{coat}^{Au}/R_{ref}} \right) \times R_{Au}^{abs} \quad (2.2)$$

R_{Au}^{abs} is the absolute value of the reflectance of gold, which is easy to measure by using another material of known reflectance as reference.

Gold is used for evaporation at FIR, MIR and NIR frequencies, because of its high reflectance (>0.98). However, the reflectance of gold reduces dramatically by more than 60 % at frequencies above $20,000 \text{ cm}^{-1}$. Therefore, aluminum is used instead for evaporation at visible and UV frequencies since its reflectance is still as high as 0.93. The accuracy of the reflectance measured by using the *in situ* evaporation technique was estimated to be better than $\pm 0.5\%$.

2.2.3 Steps Towards Good Optical Alignments

In order to achieve a good optical alignment, the following three steps are taken before performing the reflectance measurements.

Step #1: Adjustments of the position and the orientation of the sample. In the reflectance measurements of single crystals, the samples with shiny surfaces are always preferred to maximize the signal intensity. Fortunately, the HTSC single crystals usually can be easily cleaved to expose a shiny surface of *ab*-plane since the unit cells have graphite-like layered structures and the *ab* planes are weakly coupled along

the c-axis direction. In a good alignment of the sample position, after a rotation of the sample stage by 90 degrees, the sample should be located where the stainless steel mirror was and more important, the surface of the sample after rotating should be parallel to the surface of the mirror before rotating. The L-shaped sample stage guarantees a good position match of the sample and the mirror before and after the rotation. To calibrate the angle of the sample surface after it has been glued to the tip of a brass cone, a fine adjustment of the angle of the sample cone can be made through three set screws in it with a laser alignment process. First of all, a laser is shined on the stainless steel mirror (the reference position) and the location of the reflected laser spot on a white screen is recorded. And then the sample stage is rotated to the sample position with the surface of the sample being illuminated by the laser. In the case of a bad alignment, the laser spot reflected from the sample surface would deviate from the original spot for the stainless steel mirror. The three set screws in the sample cone are then finely adjusted to achieve a perfect match of the two laser spots of the reference and sample positions.

Step #2: Adjustments of the orientation of the toroidal mirrors. After the well-aligned sample stage has been loaded in the sample chamber, fine adjustments of the angles of the two toroidal mirror (L1 and L2), as shown in Figure 2.1, are required to get the incident light perfectly focused on the sample surface and the reflected light focused in the detector. The W lamp (NIR source) and the UV (CaF_2) beamsplitter are used to generate the visible incident light for the alignments with eyes. Normally, after these preliminary adjustments have been done, we would get a signal in the Bruker program with the correct light source and the beamsplitter. A finer adjustment of the angle of the toroidal mirror L2 is made later on to obtain a maximum of the signal intensity.

Step #3: Adjustment of the orientation of the interferometer fixed mirror.

Last but not least, an adjustment of the orientation of the fixed mirror is required for achieving the best alignment of the interferometer. Each time the beamsplitter is exchanged for different spectral domains, the adjustment of the fixed mirror has to be made due to the different physical properties of different beamsplitters. There are two stepper motors (knobs X and Y) in the Bruker spectrometer that control the two degrees of freedom of the fixed plane mirror. An auto-adjustment of the two motors can be done within the Bruker program to maximize the spectrum amplitude. However, if the fixed mirror is completely misaligned, the movable mirror (the scanner) would stop scanning and the auto-alignment option wouldn't help any more. This happened during the FIR measurements with the 6 μm Mylar/Ge beamsplitter. In the Bruker spectrometer, one HeNe laser is used to control the position of the scanner, for example, the position for the zero path difference. The monochromatic light beam from the laser is modulated by the interferometer as well and the sine wave shaped signal can be monitored with an oscilloscope connected to two of the testpoints (LSA2 and LSB2). If the signal amplitude is lower than the threshold for the beamsplitter installed (*e.g.*, 0.6V for the 6 μm Mylar/Ge beamsplitter), the scanner would stop. At this point, a manual adjustment of the fixed mirror has to be performed. While moving the scanner by hand, gently turned X- and Y- knobs one by one to maximize the amplitude of the sinusoidal wave observed on the oscilloscope. Once the signal exceeds the threshold value, the scanner would start scanning normally. Then the auto-adjustment can be run for a finer alignment of the fixed mirror.

2.2.4 Summary of Temperature-dependent Measurements

The temperature-dependent reflectance measurements on the HTSC samples are carried out at a variety of temperatures (usually 7-9 different temperature points)

between 28 K and 295 K. Two cycles of the temperature variation are performed in each of the spectral regions. The strategies we adopt for the consistence and reproducibility of our data are the followings.

First of all, the power spectra ratio of the sample and the stainless steel reference R_{sam}/R_{ref} is measured at room temperature. We repeat the measurement for 5 times to check whether the data are reproducible and average them to increase the signal-to-noise ratio. Secondly, the temperature is reduced all the way down to 28 K and the averaged ratio R_{sam}/R_{ref} is taken at 28 K. Next, the temperature is increased step by step and stabilized at each temperature that we are interested in and the averaged ratio R_{sam}/R_{ref} is taken. When the sample is back up to room temperature, the ratio R_{sam}/R_{ref} is recorded once again and compared with the data measured before the thermal cycle. Normally, the variation of the data is within 0.5 %, which is also used as a criterion for monitoring any changes in the surface properties of the sample during the temperature changes. At this point, half of the measurements have been done and the *in situ* Au/Al evaporation can be performed under the conditions described in Section 2.2.3. After the sample has been coated with a layer of gold or aluminum, the room temperature data R_{coat}^{Au}/R_{ref} is taken as before. Then the second thermal cycle starts and the procedures of the measurements at different temperatures are repeated. Finally, the measured quantities R_{sam}/R_{ref} and R_{coat}^{Au}/R_{ref} for different temperatures are plugged into Equation 2.2 and the temperature-dependent absolute reflectance of the sample are obtained. Note that, the absolute reflectance at room temperature is calculated with the measured R_{sam}/R_{ref} and R_{coat}^{Au}/R_{ref} right before and after evaporating Au/Al onto the sample surface.

During each thermal cycle, the data are taken once the temperature has been stabilized within 0.5 K for 5 minutes. Closer to the room temperature, the time needed for the stabilization of the temperature becomes longer and longer. Therefore,

the whole temperature-dependent measurement in each spectral domain usually lasts for more than 11 hours.

2.2.5 Low-temperature Detectors Preparations

Two low-temperature detectors have been used for the FIR, MIR and NIR measurements, as seen in Table 2.1. The MCT (Mercury-Cadmium-Telluride) detector is cooled with liquid nitrogen (L-N₂) and has to be pumped twice a year to maintain a good vacuum environment inside.

The 4K Si bolometer detector is cooled with liquid helium (L-He), which requires a more complicated preparation procedure. Before the transfer of L-He into the bolometer, the detector has to be pumped until the vacuum level becomes better than 5×10^{-6} Torr. Secondly, pre-cooling is done by transferring L-N₂ into the lower tank of the detector. The materials used for the sensors in the low-temperature detectors are basically semiconductors, which has an energy gap that opens at low temperature and a dramatic growth of resistance as a temperature decrease takes place. Once the bolometer is full of liquid N₂, the resistance, monitored by a multimeter rises from 104 Ω to 136 Ω . The upper tank should be filled with L-N₂ as well to provide a low temperature environment for a successful L-He transfer later on. The L-N₂ in the lower tank is then blown completely out with He gas and the L-He is transferred into the same tank immediately. As the can is filled with L-He, the resistance of the bolometer climbs rapidly and finally arrives at a value about 900 Ω . The L-N₂ in the upper tank has to be refilled every 9 or 10 hours to slow down the evaporation rate of the L-He in the lower tank. Normally, the holding time of the L-He in the 4K bolometer is as long as 40 hours.

2.3 Transmittance Measurements

2.3.1 Setups of Transmission Spectrometry

The transmittance of the metamaterials were measured with the transmission setups as shown in Figure 2.3 in the MIR spectral regime at the room temperature. In order to accommodate the original reflection setups to transmission spectrometry, we fabricate new sample holders to allow light to pass through and add a beam-focusing chamber to the sample chamber to focus the transmitted light onto a MCT detector. The sample holder for the transmittance measurements is also made of brass, but has a counter-cone shape with a small hole in the center. The Si wafer with the metamaterial patterns on it is loaded into the square space at the back of the sample holder and the patterns are exposed to the incident light through the central hole. The transmitted beam is focused on the detector by three of ZnSe spherical lenses inside in the beam-focusing tube (about 9 cm in length). A piece of the Si wafer is used as the reference.

2.3.2 Area Correction

The metamaterial patterns we studied have small areas less than 0.5 mm^2 . In order to maximize the signal intensity, the hole in the sample holder has been made a bit larger than the pattern area. Therefore, an area correction has to be taken into account when calculating the transmittance of the patterns from the measured spectra.

Take one of the split-ring resonators sample as an example, the area fraction of the pattern to the whole illuminated area is $f = 0.5$. For an incident light with an

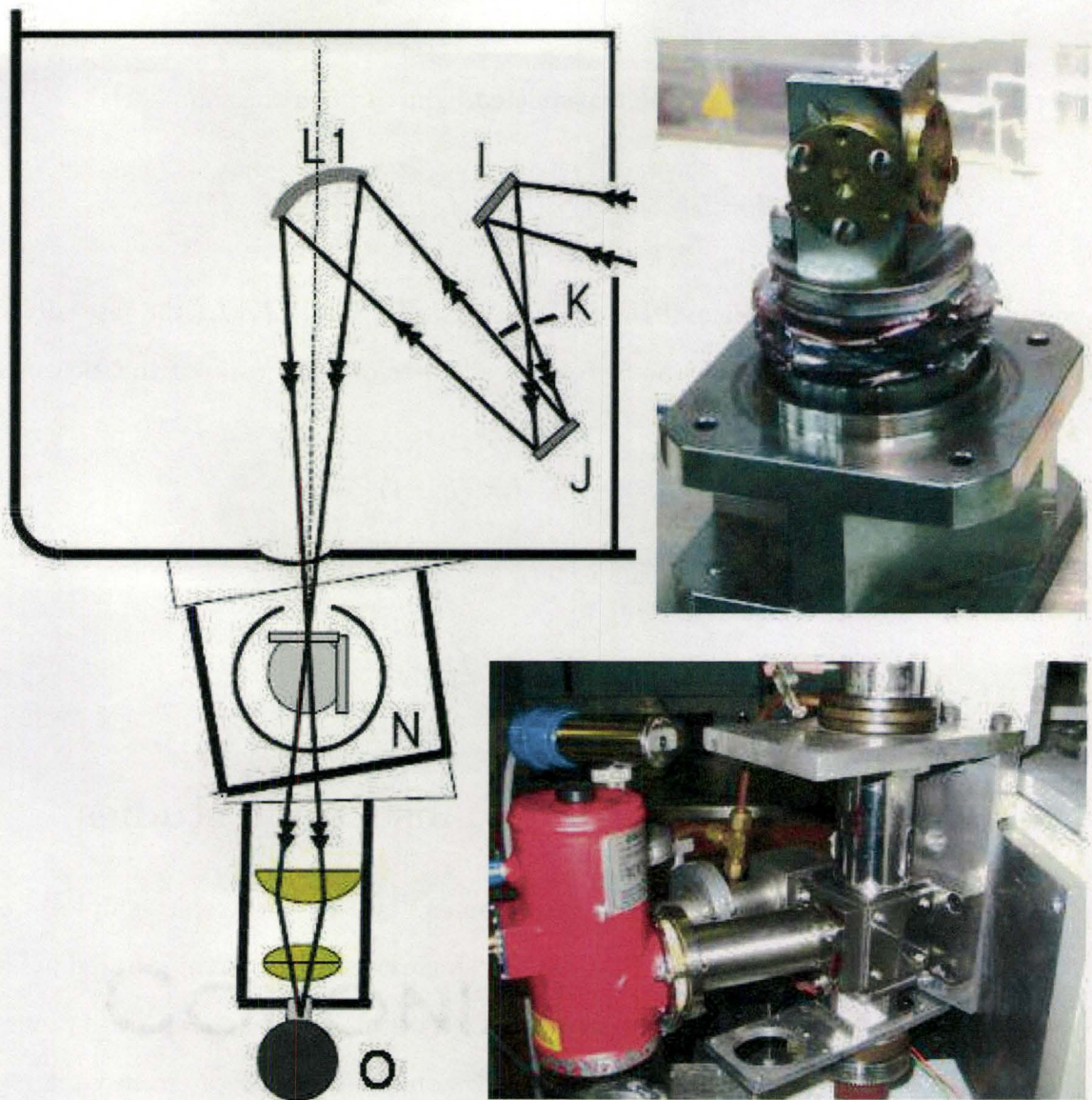


Figure 2.3 Left panel: A schematic diagram of the setups for transmission measurements. Right panel: The photographs of the sample stage for transmission (Top) and the beam-focusing chamber to focus the transmitted light to the MCT detector (Bottom).

intensity of I_o , the intensity of the transmitted light through the sample is

$$I = I_o \times f \times T \times T_{Si} + f \times I_o \times T_{Si}, \quad (2.3)$$

where T is the transmittance of the SRR pattern, $T_{Si} = I_{Si}/I_o$, I_{Si} the intensity of the transmitted light through the Si reference. Therefore, the ratio of the measured I and I_{Si} is

$$T_m = \frac{I}{I_{Si}} = f \times (T + 1) \quad (2.4)$$

and finally the transmittance of the pattern is

$$T = \frac{T_m - f}{f} \quad (2.5)$$

2.4 Infrared polarizers for anisotropic studies

In the polarization-dependent measurements on the anisotropic samples, *i.e.*, the split-ring resonators and the $\text{YBa}_2\text{Cu}_3\text{O}_{6.35}$ single crystals, different infrared polarizers have been used to generate linearly polarized beams in different spectral ranges. The rotation of the polarizer can be controlled within the Bruker program via a motor. Note that, the MIR polarizer has three strong absorption bands located around 720 cm^{-1} , $1,460 \text{ cm}^{-1}$ and $2,800\text{-}3,000 \text{ cm}^{-1}$, which give rise to the noises in those frequency ranges in the reflectance and transmittance data. The first two absorption bands are fairly narrow and the corresponding noise can be simply smoothed away. The noisy part above $2,800 \text{ cm}^{-1}$ caused by the broad absorption band can be cut off, since the NIR spectral region starts from $2,500 \text{ cm}^{-1}$ and the NIR polarizer has no absorptions in this region. The visible polarizer cuts off the spectrum above $26,000 \text{ cm}^{-1}$.

Chapter 3

Theory and Methods of Analysis

3.1 Introduction

This chapter includes three parts, the classical electromagnetic theory of the optical response of solids, the analytical and numerical inversion techniques employed to extract the electron-boson spectral functions from the optical data, and the way of numerical simulations for the metamaterials.

3.2 Optical Response of Solids

3.2.1 Optical Parameters

As mentioned in Chapter 2, what we measure in the optical studies on the single crystals of high- T_c cuprates is essentially the reflectance spectra in a wide frequency regime, which is macroscopic but can provide us with the microscopic information of materials through classical electromagnetic theory. Here we only show a concise derivation of the optical constants based on Maxwell's equations. Detailed

principles and derivations can be found in a number of books (Kittel, 1976, Fowles, 1989, Born and Wolf, 1999). Note that the situation discussed here is for non-magnetic media, where $\mu = 1$. The following equations are in the CGS units.

The wave equation of light propagating in an isotropic dielectric material, given by Maxwell's equations, is

$$\nabla^2 \vec{E} = \frac{\epsilon_1}{c^2} \frac{\partial^2 \vec{E}}{\partial t^2} + \frac{4\pi\sigma_1}{c^2} \frac{\partial \vec{E}}{\partial t}, \quad (3.1)$$

where \vec{E} is the electric component of light, ϵ_1 is the real part of the dielectric function, σ_1 the real part of the conductivity, and c the light velocity.

For a plane wave solution of Equation 3.1

$$\vec{E} = \vec{E}_0 e^{i(\vec{k}\cdot\vec{r}-\omega t)}, \quad (3.2)$$

we obtain a dispersion relation as

$$k = \frac{\omega}{c} \sqrt{\epsilon_1 + i \frac{4\pi\sigma_1}{\omega}}. \quad (3.3)$$

The complex refractive index \tilde{N} is defined as

$$\tilde{N} \equiv \frac{ck}{\omega} = n + i\kappa, \quad (3.4)$$

where n is the index of refraction and κ is the extinction coefficient. It is also known that

$$\tilde{N}^2 = \tilde{\epsilon} = \epsilon_1 + i\epsilon_2, \quad (3.5)$$

where ϵ_1 and ϵ_2 are the real and imaginary parts of the complex dielectric function $\tilde{\epsilon}$.

Alternatively, the complex refractive index \tilde{N} has another form in terms of the

real and imaginary parts of the optical conductivity $\tilde{\sigma} = \sigma_1 + i\sigma_2$,

$$\tilde{N}^2 = \epsilon_\infty + \frac{4\pi i}{\omega}(\sigma_1 + i\sigma_2), \quad (3.6)$$

where $\epsilon_\infty = 1$.

Therefore, we end up with the following relations between different optical constants.

$$\epsilon_1 = n^2 - \kappa^2, \quad \epsilon_2 = 2n\kappa. \quad (3.7)$$

and

$$\sigma_1 = \frac{\omega}{4\pi}\epsilon_2, \quad \sigma_2 = \frac{\omega}{4\pi}(\epsilon_\infty - \epsilon_1). \quad (3.8)$$

For a normal incidence in vacuum, as is the case in our experiments, the complex reflection coefficient r obtained from the electromagnetic boundary conditions is

$$r = \frac{\vec{E}_r}{\vec{E}_i} = \frac{\tilde{N} - 1}{\tilde{N} + 1} = \frac{n + i\kappa - 1}{n + i\kappa + 1}, \quad (3.9)$$

where \vec{E}_i and \vec{E}_r are the electric fields of the incident and reflected waves, respectively.

If r is expressed by its amplitude R which is measured by experiment and phase factor θ ,

$$r = \sqrt{R}e^{i\theta}, \quad (3.10)$$

the complex refractive index is determined by R and θ through Equation 3.11

$$n = \frac{1 - R}{1 + R - 2\sqrt{R}\cos\theta}, \quad \kappa = \frac{-2\sqrt{R}\sin\theta}{1 + R - 2\sqrt{R}\cos\theta}. \quad (3.11)$$

Furthermore, other optical constants, *e.g.* the dielectric function and the optical conductivity can be derived in terms of R and θ based on Equations 3.7 and 3.8. Note that the optical constants are all frequency-dependent quantities. In fact, in reflectance

spectroscopy we only detect the amplitude of the complex reflection coefficient, and the phase factor is obtained through a Kramers-Kronig relation as discussed in Section 3.2.2.

3.2.2 Kramers-Kronig Relations

We are able to relate the real and imaginary parts of a response function of a linear passive system, $\alpha(\omega) = \alpha_1(\omega) + i\alpha_2(\omega)$, by using the Kramer-Kronig (KK) relations (Kittel, 1976),

$$\alpha_1(\omega) = \frac{2}{\pi} P \int_0^{\infty} \frac{s\alpha_2(s)}{s^2 - \omega^2} ds, \quad (3.12)$$

$$\alpha_2(\omega) = -\frac{2\omega}{\pi} P \int_0^{\infty} \frac{\alpha_1(s)}{s^2 - \omega^2} ds, \quad (3.13)$$

where P represents the principle integral.

One of the most important applications of the KK relations is to find the phase information of the complex reflectance coefficient $r(\omega)$, which is a response function between the incident and reflected waves.

$$\theta(\omega) = \frac{\omega}{\pi} P \int_0^{\infty} \frac{\ln R(\omega')}{\omega^2 - \omega'^2} d\omega'. \quad (3.14)$$

Note that the KK relation as in Equation 3.14 requires an integration from 0 to infinity. However, only a finite spectral range of reflectance can be obtained in our experiments. Therefore, extensions of the reflectance data beyond the detectable frequency region are needed.

3.2.3 Low- and High- Frequency Extrapolations

For the low-frequency extrapolations, *i.e.* extrapolating the reflectance data at the lowest frequency toward zero frequency, different models are used for insulators, normal metals and superconductors.

In the case of insulators, the low-frequency reflectance is assumed to be constant towards DC, while for the normal metals, we apply the Hagen-Rubens approximation

$$R(\omega) = 1 - A\sqrt{\omega}. \quad (3.15)$$

where A is a constant that can be determined by the low-frequency part of the reflectance data. Equation 3.15 is a low-frequency approximation of the reflectance of a Drude metal where the electrons are scattered by static defects, for $\omega < 1/\tau$ where $1/\tau$ is the scattering rate. The Hagen-Rubens approximation is used for the low-frequency extrapolations for the normal states of HTSCs; while for the superconducting states, a 4th order approximation $R(\omega) = 1 - A'\omega^4$ is applied, which is the reflectance of a system with a delta function conductivity at the origin.

Beyond the upper limit of our experiments, namely $40,000 \text{ cm}^{-1}$, we use the reflectance data obtained using synchrotron radiation or high-energy electron energy-loss spectroscopy. Data at a different doping levels (Romberg et al., 1990, Terasaki et al., 1990) are employed between $40,000 \text{ cm}^{-1}$ and $100,000 \text{ cm}^{-1}$. There is not much difference in reflectance of HTSCs in the UV range and a small shift of high-frequency reflectance will not affect the optical conductivity spectra below $10,000 \text{ cm}^{-1}$. Above $100,000 \text{ cm}^{-1}$, a free carrier response, $R = \omega^{-4}$, is assumed for all the HTSC samples.

3.2.4 Drude Model, Extended Drude Model and Drude-Lorentz model

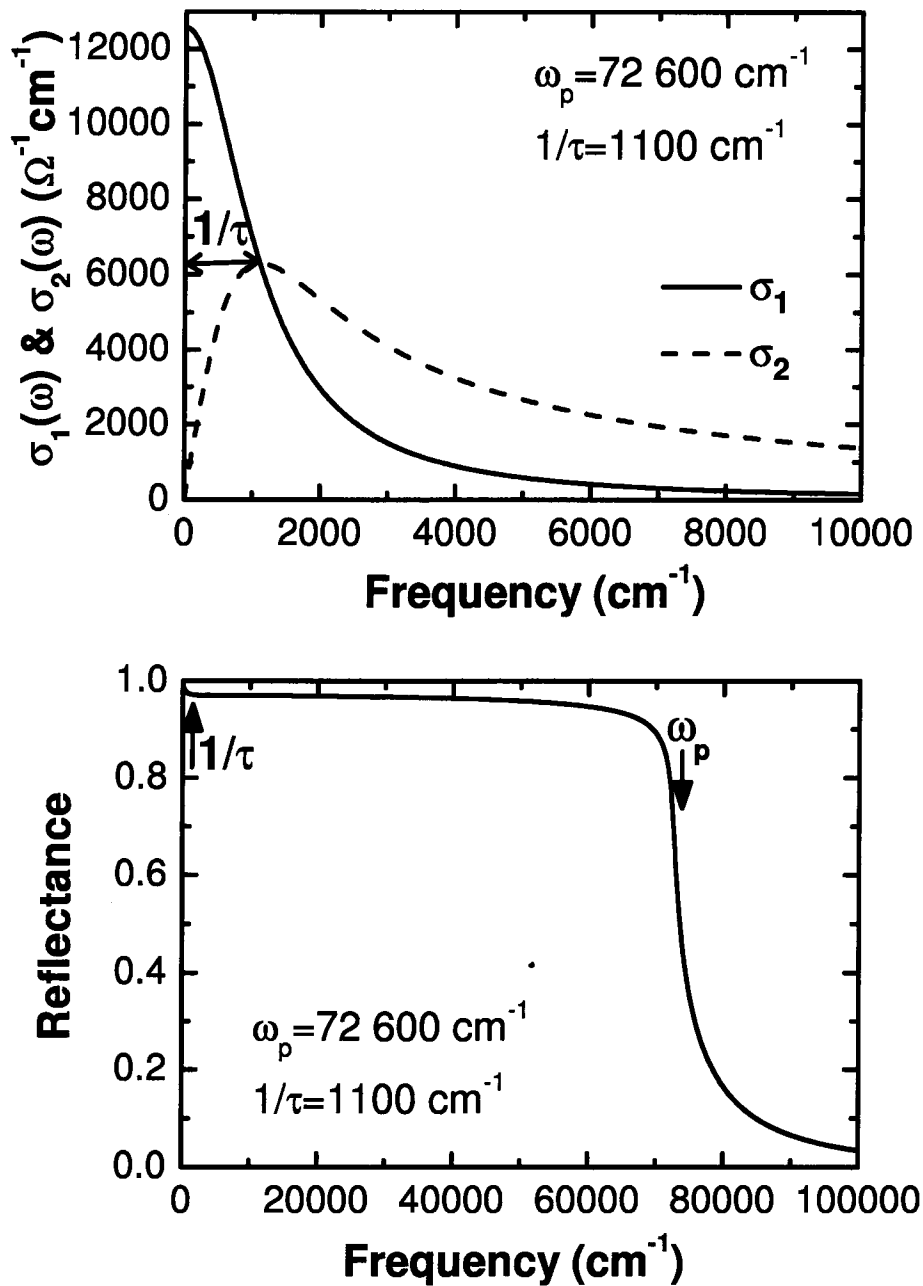


Figure 3.1 The real and imaginary parts of the optical conductivity (a) and reflectance (b) of a typical Drude metal.

The optical conductivity is of great importance in analyzing the optical data. The earliest and simplest theoretical model that describes the behavior of the conducting electrons in a metal was proposed by Drude in 1900. In the Drude model the electron-electron interactions and the electron-ion core interactions are ignored. The optical conductivity is given by,

$$\bar{\sigma}(\omega) = \frac{i}{4\pi} \frac{\omega_p^2}{\omega + i/\tau} \quad (3.16)$$

where ω_p denotes the plasma frequency and $1/\tau$ is the scattering rate. In the Drude model, only the elastic scattering of electrons from the lattice defects or impurities are taken into account, thus the scattering rate is a constant and not frequency-dependent. Figure 3.1 displays the optical conductivity of a Drude model and the corresponding reflectance derived based on the relations among the optical constants as mentioned in Section 3.2.1.

In a system where the electrons are strongly correlated, such as HTSCs, the Drude model does not apply. There are two analytical approaches that can be adopted to describe the non-Drude like optical responses. One is the extended Drude model and the other is the Drude-Lorentz model.

The extended Drude model is often used to describe the optical responses of a correlated-electron system in the low frequency regime. The electron correlations are described by two frequency-dependent parameters, $\lambda(\omega)$ and $\tau(\omega)$, as in Equation 3.17,

$$\bar{\sigma}(\omega) = \frac{i}{4\pi} \frac{\omega_p^2}{\omega[1 + \lambda(\omega)] + i/\tau(\omega)} \quad (3.17)$$

where $1 + \lambda(\omega) \equiv m^*(\omega)/m(\omega)$ is the ratio of the effective electron mass to the free

electron mass. The optical self-energy $\tilde{\Sigma}^{op}(\omega) = \Sigma_1^{op}(\omega) + i\Sigma_2^{op}(\omega)$ is defined as

$$-2\Sigma_1^{op}(\omega) \equiv \omega\lambda(\omega) = -\frac{\omega_p^2}{4\pi}\text{Im}\left(\frac{1}{\tilde{\sigma}(\omega)}\right) - \omega, \quad (3.18)$$

$$-2\Sigma_2^{op}(\omega) \equiv \frac{1}{\tau(\omega)} = \frac{\omega_p^2}{4\pi}\text{Re}\left(\frac{1}{\tilde{\sigma}(\omega)}\right). \quad (3.19)$$

The frequency-dependent optical scattering rate $1/\tau(\omega)$ represents the inelastic scattering process of the electrons from the bosonic collective excitations. In this thesis, the analysis of the bosonic spectral function of the HTSC systems is mainly within the extended Drude model frame work.

The Drude-Lorentz model ascribes the optical-activated excitations in solids to a combination of free electrons and the bound carriers which are related to the high-energy interband transitions. As shown in Equation 3.20, the dielectric function is a summation of the Drude component and a series of Lorentz oscillators,

$$\tilde{\epsilon}(\omega) = 1 + \sum_{k=0}^{m-1} \frac{\omega_{pk}^2}{\omega_k^2 - \omega^2 - i\omega/\tau_k} \quad (3.20)$$

where ω_k is the resonance frequency which stems from the corresponding restoring force (analogous to the spring force). The behavior of the free electrons is described by the first term of the oscillators where $k=0$ and there is no restoring force, $\omega_0=0$, which is exactly the dielectric function derived from the Drude model. The rest of the terms where $k > 0$ are attributed to the bound electrons with higher resonance frequencies. The Drude-Lorentz model enables us to assign the high-frequency optical responses to the interband transitions, although the underlying physics of the transitions cannot be resolved within this model. In this thesis, the Drude-Lorentz model is adopted to quantitatively characterize the optical phonons in the highly underdoped YBCO_{6.35}

sample in order to generate phonon-free optical constants for further analysis.

3.2.5 Estimations of ϵ_H and ω_p

The estimations of the values of the parameters ϵ_H and ω_p are critical in deriving the optical scattering rate. ϵ_H by its definition is the contribution of the high-frequency interband transitions to the dielectric function. The cutoff frequency which separates the Drude component and the high-energy components has to be known. However, the components are usually not well separated and one can approximately find the cutoff frequency by extrapolating the room-temperature absorption coefficient curve in a way proposed by Hwang *et al.* (Hwang et al., 2007a). As shown in Figure 3.2, we define the frequency where the absorption coefficient curve intersects with the x -axis the cutoff frequency ω_c . Therefore, ϵ_H is defined as

$$\epsilon_H \equiv \epsilon_1(\omega)|_{\omega \rightarrow 0} = 1 + \frac{120}{\pi} (P \int_{\omega_c}^{\infty} \frac{\sigma_1(\omega')}{\omega'^2 - \omega^2} d\omega')|_{\omega \rightarrow 0}. \quad (3.21)$$

And the plasma frequency ω_p is defined as

$$\omega_p = \sqrt{\frac{120}{\pi} \int_0^{\omega_c} \sigma_1(\omega') d\omega'}. \quad (3.22)$$

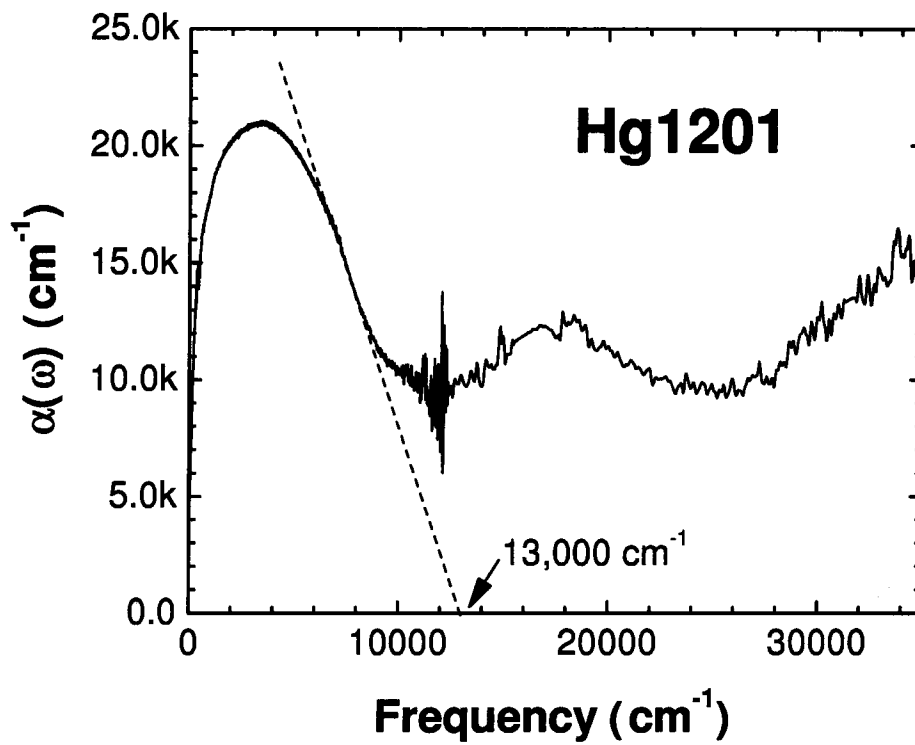


Figure 3.2 In this example the cutoff frequency ω_c is defined as the point where $\alpha(\omega)$, the absorption coefficient of the low frequency Drude conductivity, extrapolates to zero.

3.3 Bosonic Spectra Extracted From Optical Scattering Rate

3.3.1 Sharapov's Formula (Model Fits)

We adopted an analytic formula derived by Sharapov *et al.* (Sharapov and Carbotte, 2005), as mentioned in Section 1.2.1, to relate the optical scattering rate with the electron-boson spectral function $I^2\chi(\Omega)$ of the normal states of highly underdoped YBCO_{6.35}, as displayed in Equation 3.23.

$$\begin{aligned} \frac{1}{\tau(\omega, T)} &= \frac{\pi}{\omega} \int_0^{+\infty} d\Omega I^2\chi(\Omega) \int_{-\infty}^{+\infty} dz [N(z - \Omega) + N(-z + \Omega)] \\ &\quad \times [n_B(\Omega) + 1 - f(z - \Omega)][f(z - \omega) - f(z + \omega)] + \frac{1}{\tau_{elastic}} \end{aligned} \quad (3.23)$$

where $N(z)$ is the density of states (DOS) of the quasiparticles, $n_B(\Omega)$ and $f(z)$ are Boson and Fermion occupation numbers, $n_B(\Omega) = 1/(e^{\beta\Omega} - 1)$, $f(z) = 1/(e^{\beta z} + 1)$ and $\beta = 1/(k_B T)$. For the underdoped cuprate systems, $N(z)$ is not constant in the vicinity of Fermi levels for the normal states due to the presence of the pseudogap. In our model, the DOS of the highly underdoped YBCO_{6.35} system is described by a function as shown in Figure 3.3, a pseudogap plus a recovery right above the pseudogap to conserve the DOS (Hwang *et al.*, 2008b). The function form of DOS used is given by

$$\begin{aligned} N(z) &= [N(0) + [1 - N(0)] \frac{z^\alpha}{\Delta_{pg}^\alpha}] \theta(\Delta_{pg} - |z|) + [1 + \frac{\alpha}{\alpha + 1} (1 - N(0))] \\ &\quad \times \theta(2\Delta_{pg} - |z|) \theta(|z| - \Delta_{pg}) + \theta(|z| - 2\Delta_{pg}), \end{aligned} \quad (3.24)$$

where $\theta(x)$ is Heaviside step function and α corresponds to the shape of the pseudogap. One critical parameter in the DOS function is the size of the pseudogap Δ_{pg} , which is estimated to be $550 \pm 80 \text{ cm}^{-1}$ for our sample of highly underdoped $\text{YBCO}_{6.35}$ shown in Figure 3.3, from a summary of the pseudogap energy scale as a function of hole doping based on different experiments (Hüfner et al., 2008).

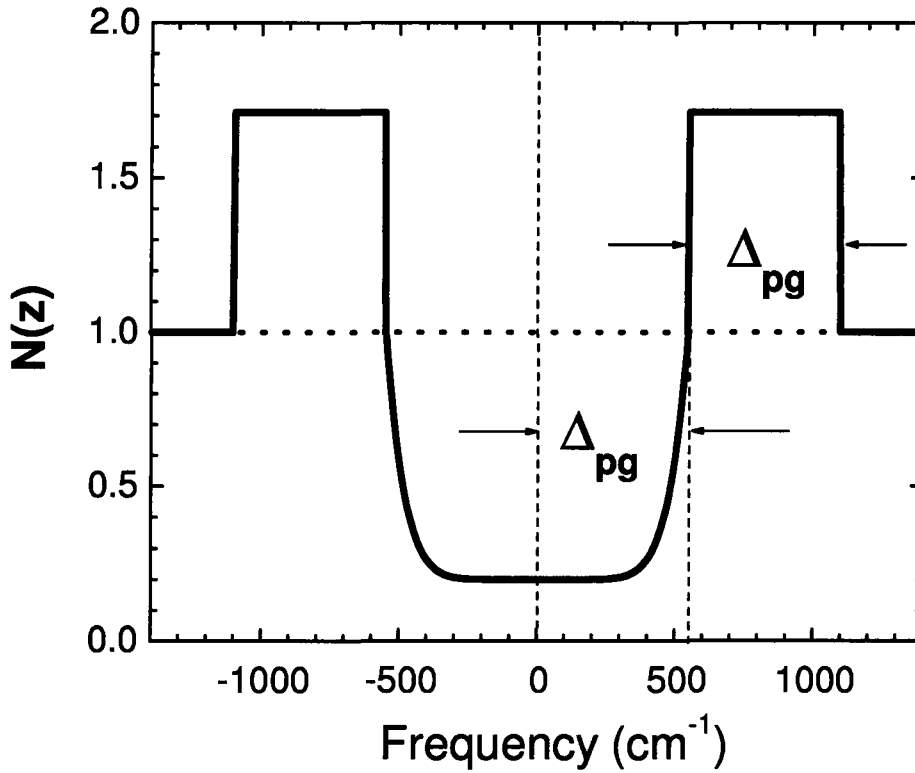


Figure 3.3 The density of states of the quasiparticles in vicinity of the Fermi energy for the normal states of the highly underdoped $\text{YBCO}_{6.35}$.

In our model fits, the bosonic spectrum $I^2\chi(\Omega)$ of YBCO is assumed to be composed of a bosonic mode and a broad background, based on the corresponding local magnetic spin susceptibility spectrum determined by neutron studies. Specific functions are adopted to describe the mode and the background, which are given in Chapter 5. By fitting the experimental curves of optical scattering rate with Equation 3.23, we determine the values of the unknown parameters in the functions of the mode

and the background of $I^2\chi(\Omega)$.

3.3.2 Maximum Entropy Inversion

As seen in Equation 3.23, the extraction of the bosonic spectral function $I^2\chi(\Omega)$ from the optical scattering rate $1/\tau(\omega)$ involves the inversion of an integral equation. Besides the model fits, there are other inversion methods that can be used (Schachinger et al., 2006), such as the second derivative method, the singular value decomposition, and the maximum entropy method. Details about the maximum entropy inversion technique can be found in a paper by Schachinger *et al.* (Schachinger et al., 2006). Here, we only give a general description of this inversion method.

The method of inversion starts with a deconvolution of an approximate relation

$$\frac{1}{\tau_{op}(\omega; T)} = \int_0^\infty d\Omega K(\omega, \Omega; T) I^2\chi(\Omega), \quad (3.25)$$

where $\tau_{op}^{-1}(\omega; T)$ denotes the optical scattering rate and T is temperature. $K(\omega, \Omega; T)$ is a kernel that can be determined from theory. For the kernel of the normal states of HTSCs, Shulga *et al.* extended Allen formula (Allen, 1971) to finite temperatures and obtained an approximate form based on a full Eliashberg theory, (Carbotte, 1990),

$$K(\omega, \Omega; T) = \frac{\pi}{\omega} \left[2\omega \coth\left(\frac{\Omega}{2T}\right) - (\omega + \Omega) \coth\left(\frac{\omega + \Omega}{2T}\right) + (\omega - \Omega) \coth\left(\frac{\omega - \Omega}{2T}\right) \right]. \quad (3.26)$$

Equation 3.26 deals with the case where no pseudogap opens in the density of states. And with $n(z)$ taken as a constant in Equation 3.24, Equation 3.25 reduces to Equation 3.23. For the kernel of the superconducting states, Allen derived a formula within the BCS theory which is appropriate for the superconducting transitions with s -wave symmetry. For HTSCs that have d -wave symmetry of superconducting order para-

meters, Carbotte *et al.* (Carbotte and Schachinger, 2006) revised Allen formula and simulated the effect of d -wave in a first approximation,

$$K(\omega, \Omega; T = 0) = \frac{2\pi}{\omega} \langle (\omega - \Omega) \theta(\omega + 2\Delta_0(\vartheta) - \Omega) E(\sqrt{1 - \frac{4\Delta_0^2(\vartheta)}{(\omega - \Omega)^2}}) \rangle_{\vartheta}. \quad (3.27)$$

In Equation 3.27, the size of the maximum of a d -wave gap, $\Delta_0(\vartheta) = \Delta_0 \cos(2\vartheta)$, which reflects the d -wave symmetry, $\langle \dots \rangle_{\vartheta}$ represents an angular average over a distribution of the d -wave superconducting gaps and $E(x)$ denotes a complete elliptic integral of the second kind. Since Equation 3.27 is for zero temperature, an approximation of the variation of Δ_0 with temperature based on the BCS theory is adopted for finite temperature cases.

The approach utilized to deconvolute Equation 3.25 is a maximum entropy method (Carbotte and Schachinger, 2006) suggested originally by Jaynes (Jaynes, 1957). This method is based on a discretization of the integral in Equation 3.25 and provides the most likely solution of $I^2\chi(\Omega)$ within the constrain that $I^2\chi(\Omega) \geq 0$ based on the Bayesian probability theory. The most uninformative prior probability distribution in Bayes's theorem is given by the maximum entropy prior in the particular case discussed here. The electron-boson spectral function $I^2\chi(\Omega)$ obtained from the deconvolution is further refined within the frame of a full Eliashberg formulism and based on a least-square fit of the calculated optical scattering rate to the experimental data .

3.4 Numerical Simulations for Metamaterials

3.4.1 Calculations of S -Parameters

The simulations of the S -parameters (*i.e.*, the complex reflection and transmission coefficients, $S_{11}, S_{12}, S_{21}, S_{22}$) and the surface current densities of the metamaterials are performed by using a finite element method with a commercial software High-Frequency Structure Simulator (HFSS)¹.

In the simulation of the transmission spectra $T(\omega)$ of the SRRs on a Si substrate for a normal incidence, the fringes due to the multiple reflection between the silicon-air interfaces create complications. The Si substrate has to be taken into account in the simulations, since the resonance positions of the SRR structure are proportional to $1/\sqrt{\epsilon_{Si}}$. The periodicity of the fringes is proportional to $\frac{1}{2\sqrt{\epsilon_{Si}d}}$, where d is the thickness of the Si substrate. If d is assumed small enough in the simulations, we will not see the fringes in the spectral range of calculation, since the periodicity of fringes is larger than the spectral range we look at. However, theoretical tests for different values of d reveal that the resonance of the SRRs shift to lower frequencies as the Si substrate gets thicker. One cannot use the real thickness of the Si substrate, which is $450 \mu\text{m}$ in the simulations, since the area of one unit cell of SRRs in the simulations is only $2.0 \times 2.0 \mu\text{m}^2$. As a result, in the simulations, the Si substrate has to be present and its thickness can be neither too small nor too large. Fortunately, tests for different thickness also demonstrate that the shift of SRR resonances due to the thickness of substrate saturates at certain value of d . In our simulations, the appropriate value of d is set to be $1,300 \text{ nm}$. The fringes due to the multiple reflection at the Si-air interface can be successfully eliminated by adding the perfectly matched

¹The software HFSS is provided by Prof. N. Nikolova of the department of electrical & computer engineering, McMaster University.

layer (PML) boundary, which are simulate materials that absorb outgoing waves, to one side of the Si substrate in HFSS.

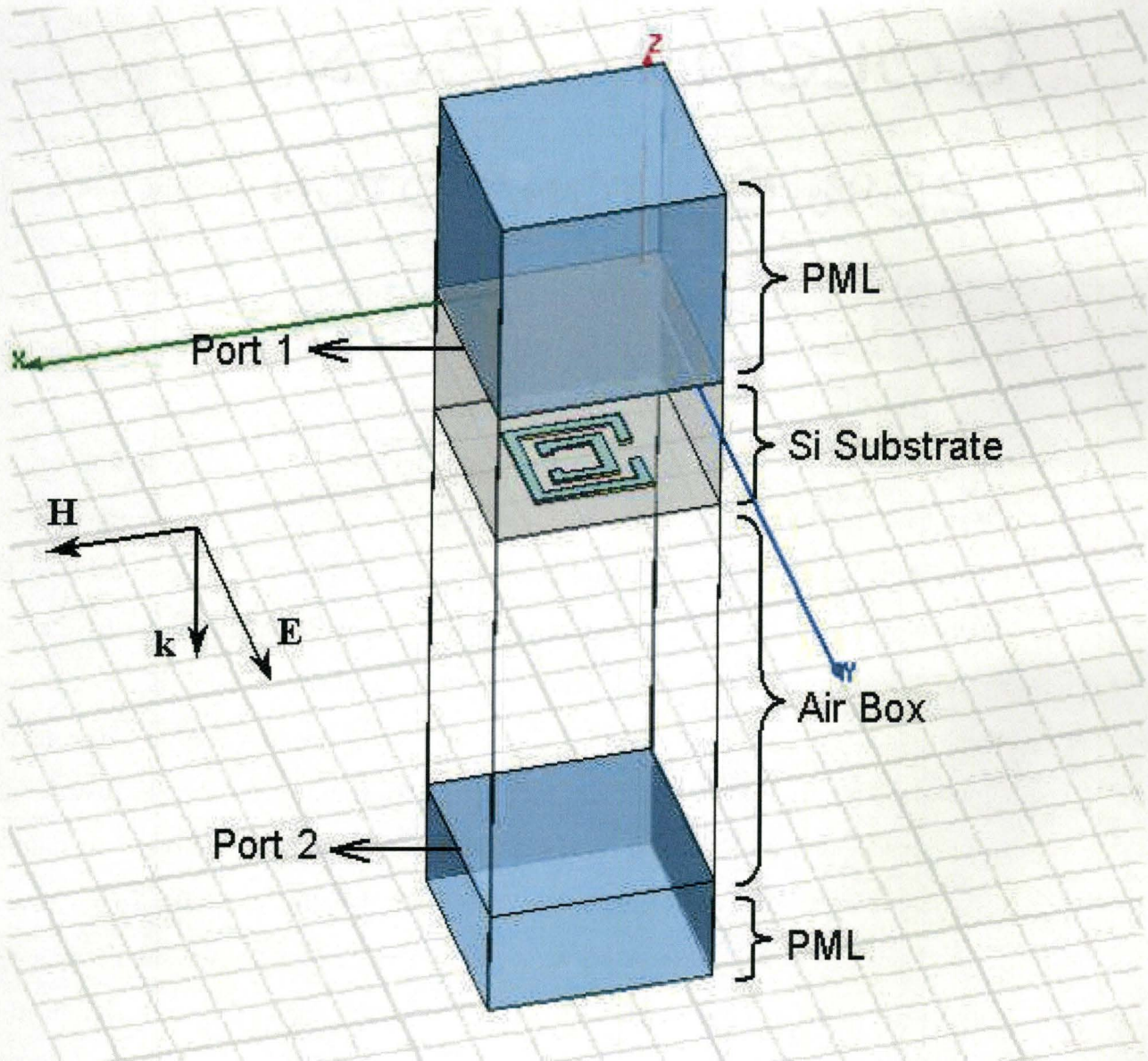


Figure 3.4 The model used to calculate the transmission of a periodic SRR array on a Si substrate.

Figure 3.4 illustrates the model used to calculate the transmission coefficient of the SRRs on a Si substrate for normal incidence. The perfectly matched layers

next to the Si substrate eliminate the reflection at the Si-PML interface, so that no radiation from the multi reflections reaches Port 2. Port 1 and 2 are assigned to be the radiation boundaries for convenient calculations of transmission $T \equiv |S_{21}|^2$. Two pairs of master/slave boundaries which are analogous to the periodic boundary conditions are assigned to the four side surfaces parallel to the z -direction. Two of the most important material parameters for the simulations are the relative permittivity and dc conductivity. We use the Drude model to determine the frequency-dependent permittivity of gold and the dc conductivity of the thin gold film is found to be 0.5×10^7 Siemens/m, which is measured by performing the Van de Pauw measurement on a 30 nm thick gold layer deposited on a Si wafer.

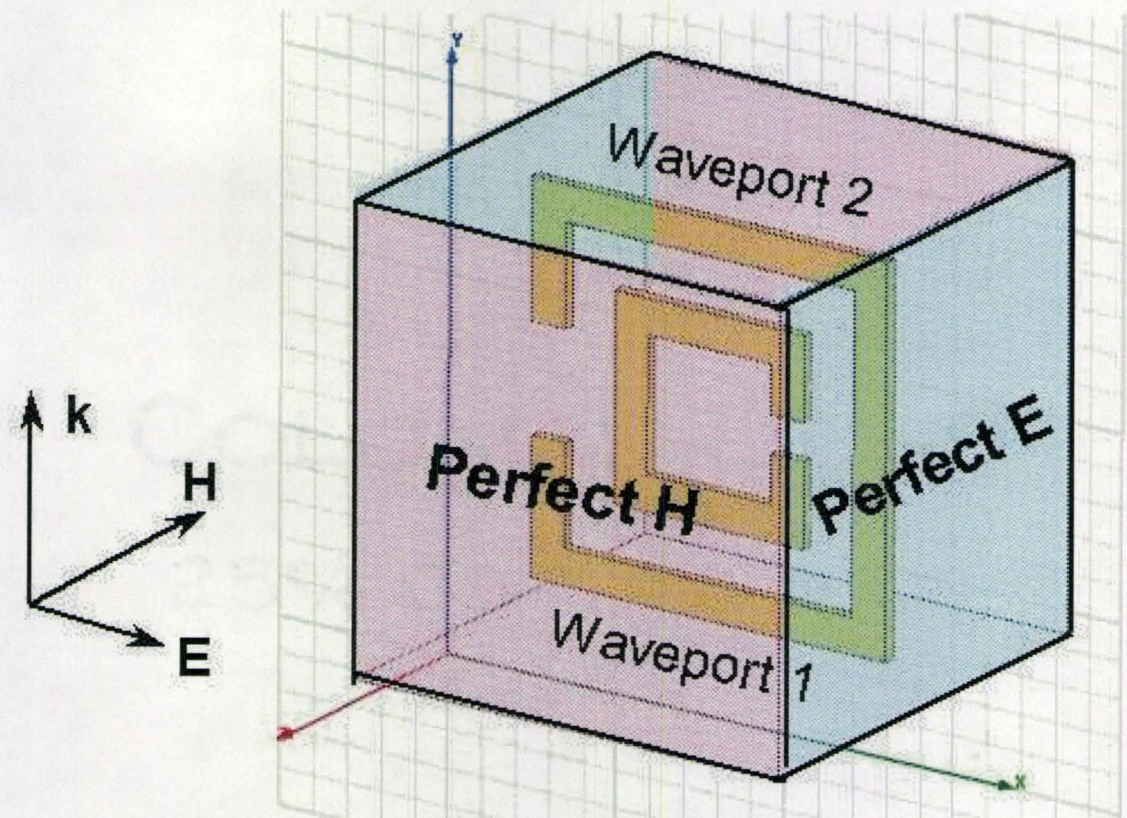


Figure 3.5 The model for simulations of the S -parameters of a periodic SRR array.

Another variation of the boundary conditions and the excitations are also used for calculation of the S -parameters more conveniently as illustrated in Figure 3.5, where the radiation and master/slave boundaries in Figure 3.4 have been replaced with the waveports and the perfect E and perfect H boundaries. In this model, the magnitude and the phase of the reflection and transmission coefficients, S_{11} and S_{21} , can be obtained automatically for all the frequency points at the same time in the simulation results, whereas for the model in Figure 3.4, one has to calculate the phase part manually for each of the frequency points individually. We have verified the perfect E and H boundary conditions are equivalent to the periodic boundary conditions in our studies, as they generate the same results.

3.4.2 Effective Material Parameters Retrieval

The effective permittivity ϵ and permeability μ are related to the refractive index n and impedance z of a metamaterial as

$$\epsilon = n/z, \mu = nz. \quad (3.28)$$

For a symmetric structure, n and z can be retrieved from the S -parameters by a standard retrieval method (Smith et al., 2002, 2005),

$$z = \pm \sqrt{\frac{(1 + S_{11})^2 - S_{21}^2}{(1 - S_{11})^2 - S_{21}^2}}, \quad (3.29)$$

and

$$\text{Im}(n) = \pm \text{Im}\left\{\frac{1}{kd} \cos^{-1}\left[\frac{1}{2S_{21}}(1 - S_{11}^2 + S_{21}^2)\right]\right\}, \quad (3.30)$$

$$\text{Re}(n) = \pm \text{Re}\left\{\frac{1}{kd} \cos^{-1}\left[\frac{1}{2S_{21}}(1 - S_{11}^2 + S_{21}^2)\right]\right\} + \frac{2\pi m}{kd}, \quad (3.31)$$

where d is the size of side along the direction of the incident wave and m is an integer that represents different branches of the arccosine function. For a passive material, additional requirements that $\text{Re}(z) > 0$ and $\text{Im}(n) > 0$ determine the choice of the + and - signs in the above functions. The choice of the right branch in Function 3.31 can be determined easily by the result itself.

For an asymmetric structure, where $S_{12} = S_{21}$ but $S_{11} \neq S_{22}$, we use a modified full S -parameter retrieval method to obtain the material parameters (Smith et al., 2005),

$$z = \pm \sqrt{\frac{(1 + S_{11})(1 + S_{22}) - S_{21}^2}{(1 - S_{11})(1 - S_{11}) - S_{21}^2}}, \quad (3.32)$$

and

$$\text{Im}(n) = \pm \text{Im}\left\{\frac{1}{kd} \cos^{-1}\left[\frac{1}{2S_{21}}(1 - S_{11}S_{22} + S_{21}^2)\right]\right\}, \quad (3.33)$$

$$\text{Re}(n) = \pm \text{Re}\left\{\frac{1}{kd} \cos^{-1}\left[\frac{1}{2S_{21}}(1 - S_{11}S_{22} + S_{21}^2)\right]\right\} + \frac{2\pi m}{kd}. \quad (3.34)$$

Chapter 4

Optical Studies of Metamaterials

4.1 Introduction

This chapter presents optical studies of left-handed behavior of the SRR metamaterials. Section 4.2 demonstrates the sample fabrication processes using the electron-beam lithography (EBL) technique and sample characterizations. Chapter 4.3 elaborates on the experimental and numerical results of the left-handed behavior of one of the double-ring SRR array samples and discusses numerically the left-handed behavior in a proposed single-ring SRR cubic structure. A summary of these studies is given in Section 4.4.

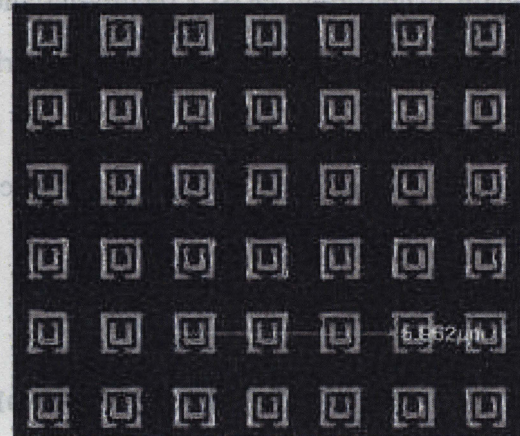
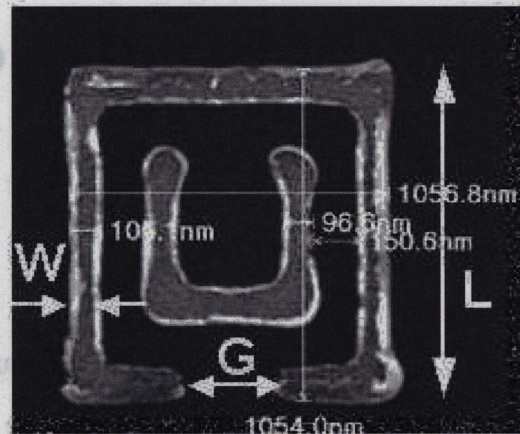
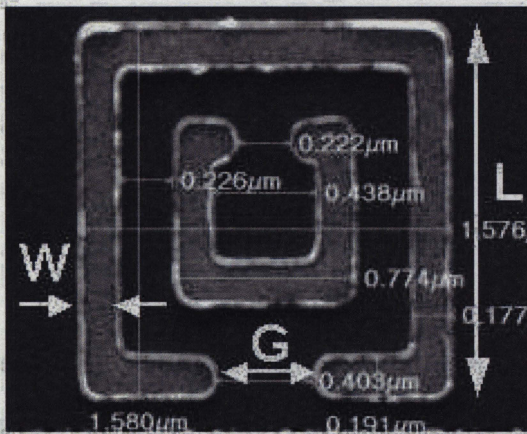
4.2 Sample Fabrications and Characterizations

We fabricate periodic double-ring SRR arrays on silicon substrates by using the EBL technique. The fabrication processes include five steps. First of all, a layer of positive photoresist PMMA, which is about 200 nm thick, is spun on a double-side polished silicon wafer (450 μm in thickness). Second, we design our pattern with the

Chapter 4

SRRs # 1

SRRs # 2



We fabricate periodic double-ring SRR arrays on silicon substrates by using

Figure 4.1 The SEM pictures of the overview and the individual element of the double-ring SRRs samples, SRRs #1 and SRRs #2. L , G and W represent the length, the gap width and the ring width for each of the split rings, respectively.

Table 4.1 The dimensions of SRRs #1 and SRRs #2, the length L , the gap width G and the ring width W for the outer and inner rings, measured with the SEM. The values are in nm.

SRRs #1	L	G	W	SRRs #2	L	G	W
Outer Ring	1,580	400	177	Outer Ring	1,056	270	105
Inner Ring	774	200	177	Inner Ring	583	250	105

software DesignCAD and setup appropriate parameters for electron-beam writing. The PMMA coated Si wafer is then mounted into the scanning electron microscope (SEM) facility for electron exposure. Only the pattern areas of the PMMA are exposed during the electron-beam writing. Before exposure to the electron beams, the four corners of the square shaped Si wafer are attached to the sample plate with a small amount of silver paste in order to avoid electron charging. After the electron-beam writing is done, the exposed PMMA areas are dissolved in a special developer (3:1 IPA:MIBK), whereas the unexposed PMMA parts are left on the Si substrate. Next, an extremely thin layer of chromium is deposited on top of the developed PMMA and then a thicker layer of gold is deposited on top of the chromium layer. The deposition of the thin layer of Cr allows better adhesion between the gold film and the Si substrate. The final step is the lift-off process where the remaining unexposed PMMA part is removed from the Si wafer by acetone. Figure 4.1 displays the SEM pictures of two of the resulting high quality patterns SRRs #1 and SRRs #2, with total areas of the SRR arrays as large as $400 \times 400 \mu\text{m}^2$. The periodicity of both samples is $2.0 \mu\text{m}$. The elements of SRRs #1 are a little larger than those of SRRs #2, as shown in Table 4.1. Atomic-force microscopy shows that the thickness of the metallic layers (including Au and Cr) is about 30 nm.

4.3 Left-Handed Behavior of Split-Ring Resonators

4.3.1 Left-Handed Behavior in A Double-Ring SRR Array

A. The Experimental Results

We measured the normal-incident transmission of the double SRRs samples at mid-infrared frequencies, between 500 and 6,000 cm^{-1} . Two mutually orthogonal polarizations of the incident light were generated by an infrared polarizer. A bare Si substrate was used as a reference to normalize the transmission of the samples. Figure 4.2(a) and Figure 4.3(a) show the frequency-dependent transmission data of SRRs #1 and SRRs #2 for two orthogonal polarizations below 3,000 cm^{-1} , where there is strong polarization dependence. The solid curves correspond to the polarization where the electric field of the incident light is parallel to the sides featuring gap of the SRRs. We call this polarization E_{\parallel} . The dashed curves are for the case wherein the E field is perpendicular to the sides featuring gap (E_{\perp}). Note that in the case of E_{\perp} , the transmissions of SRRs #1 and SRRs #2 both have two dips, whereas in the case of E_{\parallel} , SRRs #1 has one dip and SRRs #2 has three. For both polarizations, the magnetic field is in the SRRs plane.

B. Numerical Simulations and Material Parameters Retrievals

In order to find the physical origin of those features in the transmission data, we numerically simulated the transmission of one unit cell of SRRs #1 and SRRs #2 with periodic boundary conditions by using a finite element method with a commercial software High-Frequency Structure Simulator (HFSS). The simulation results for the two orthogonal polarizations of light are exhibited in Figure 4.2(b) and Figure 4.3(b) (see the solid and dashed curves). Due to the lower-limit of our experiments, the dip

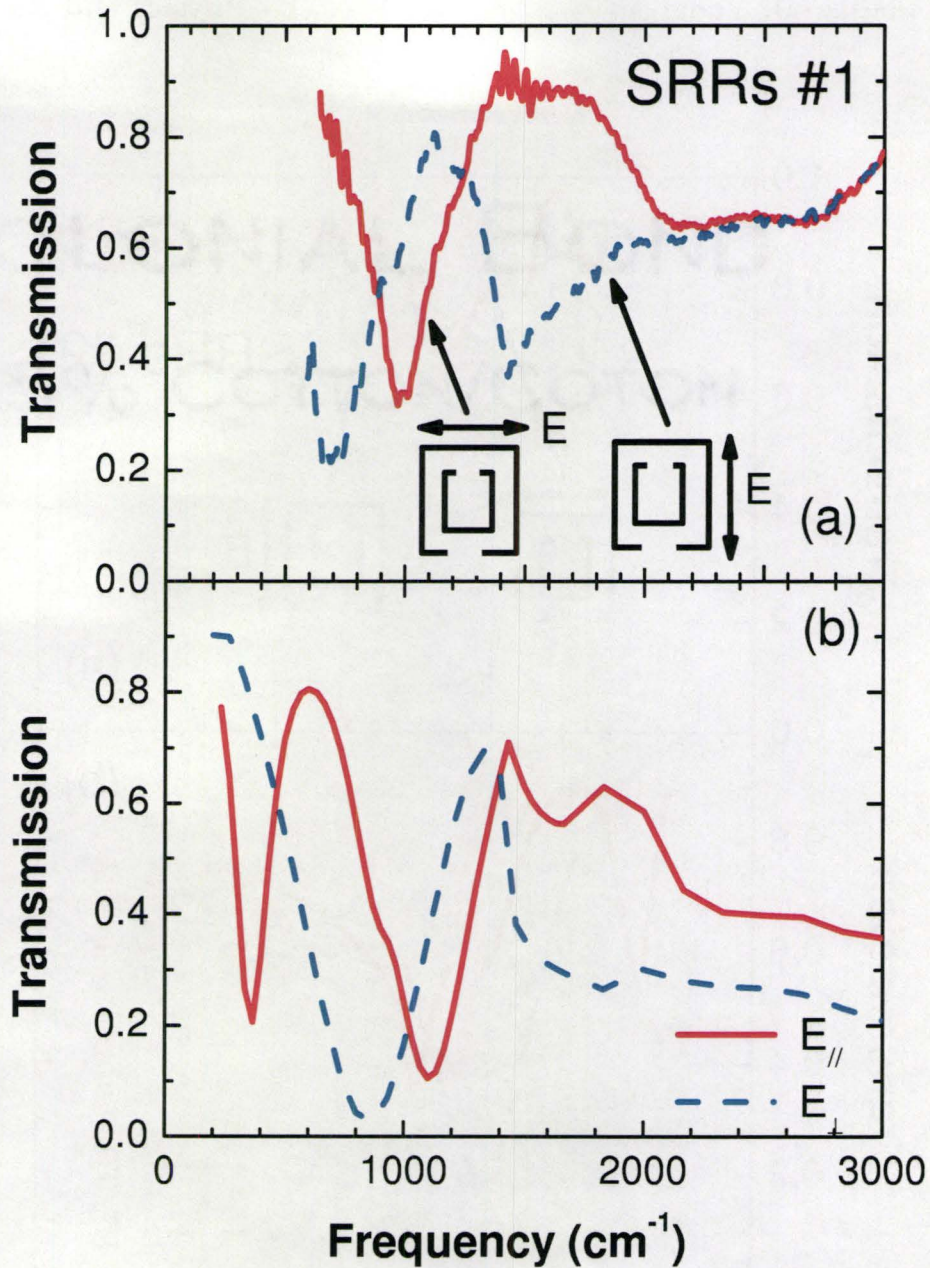


Figure 4.2 (a) The measured transmission spectra of the SRRs #1 sample for two orthogonal polarizations of light, E parallel to the sides featuring gap of the SRRs (solid red curve, for short, E_{\parallel}) and E perpendicular to the sides featuring gap (dashed blue curve, for short, E_{\perp}). (b) The numerically simulated transmission spectra for E_{\parallel} (solid red curve) and E_{\perp} (dashed blue curve).

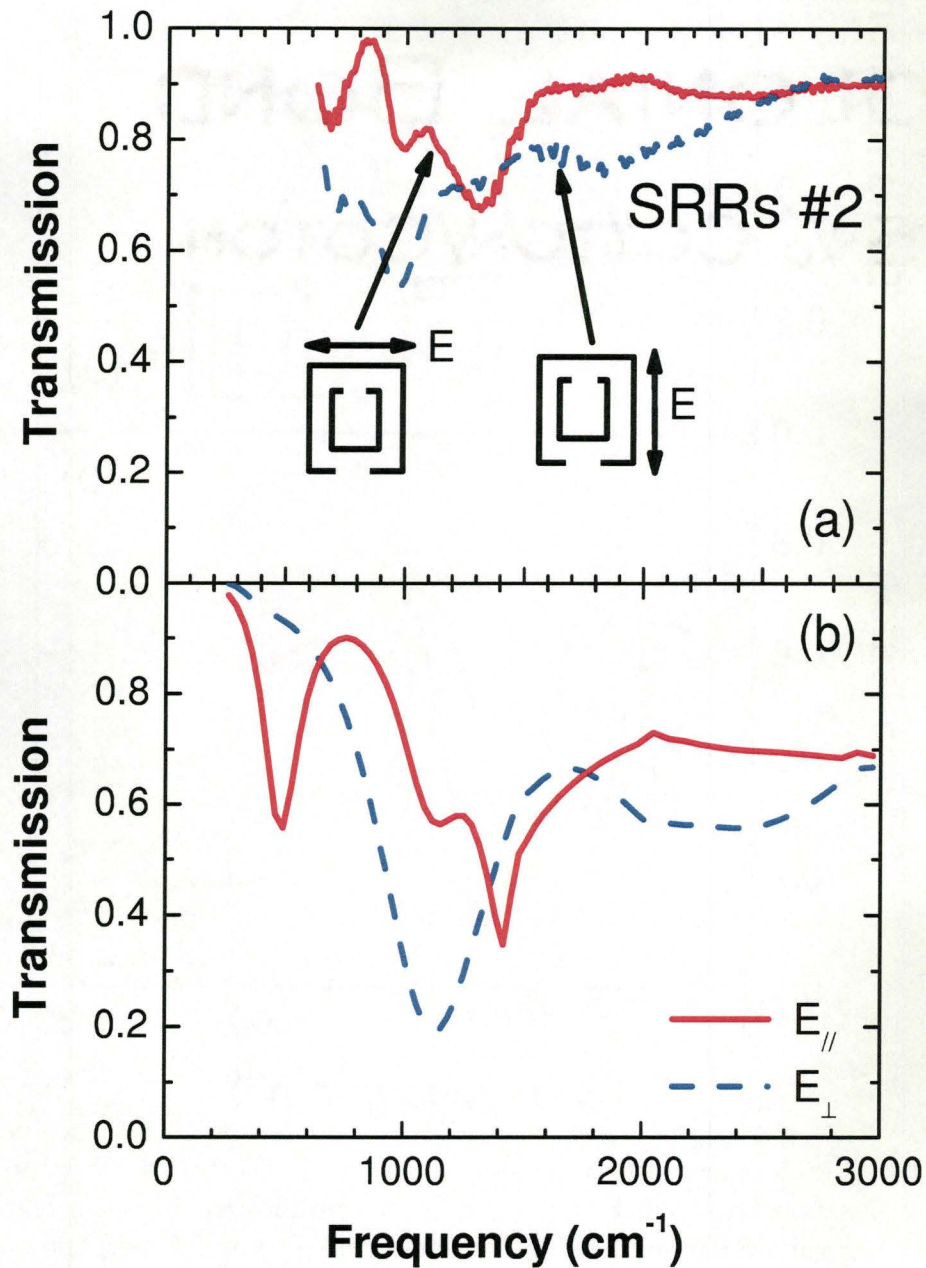


Figure 4.3 (a) The measured transmission spectra of the SRRs #2 sample for two orthogonal polarizations of light, E parallel to the sides featuring gap of the SRRs (solid red curve, for short, E_{\parallel}) and E perpendicular to the sides featuring gap (dashed blue curve, for short, E_{\perp}). (b) The numerically simulated transmission spectra for E_{\parallel} (solid red curve) and E_{\perp} (dashed blue curve).

around 367 cm^{-1} for E_{\parallel} in the simulation of SRR #1 is not seen in the experimental data, whereas the rest of the parts of the curves show good agreements with the data. However, the calculated transmissions of SRR #2 are in excellent agreement with the experimental data in terms of the overall shape and the positions of the dips. Since the two SRRs samples have similar features, we use SRR #2 for further analysis.

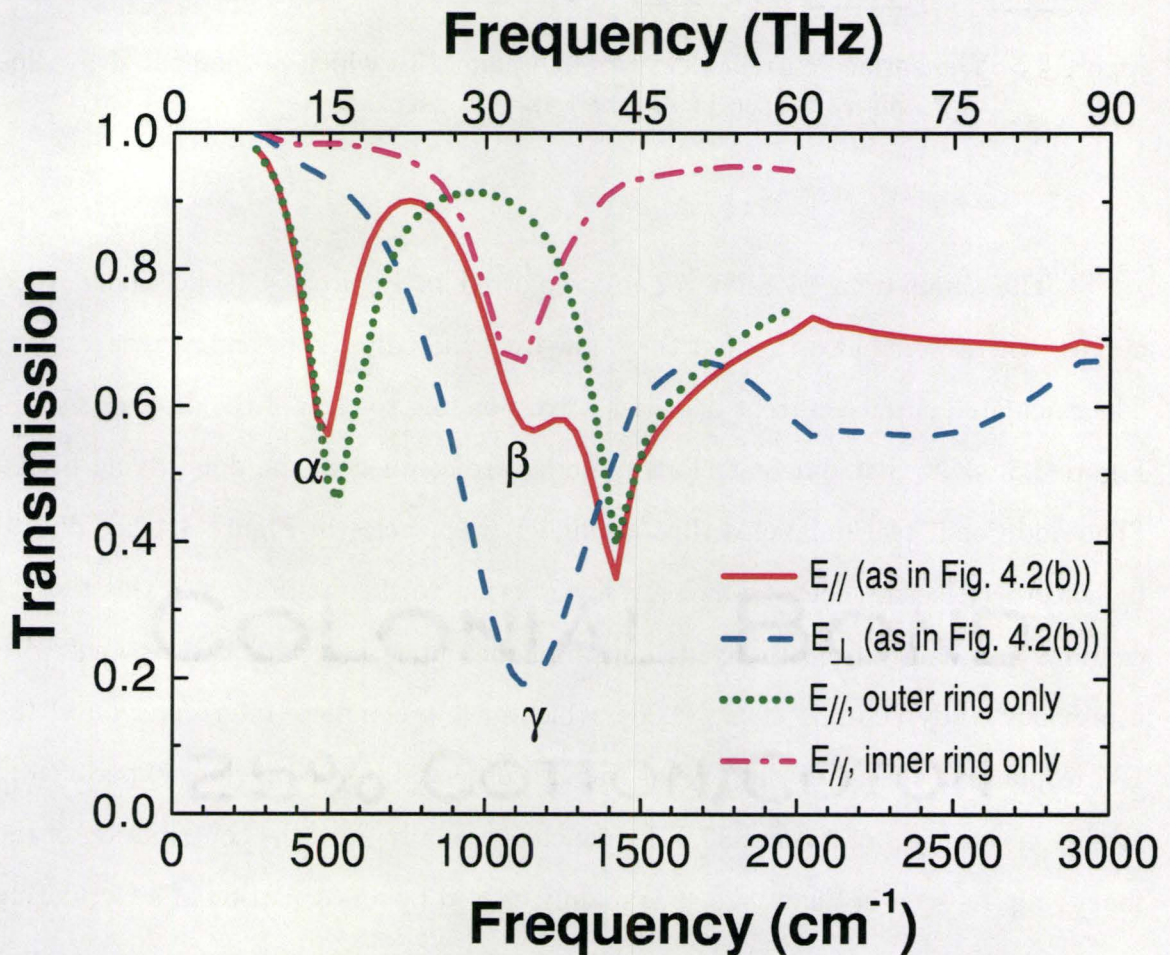


Figure 4.4 The simulated transmission spectra of SRRs #2 for E_{\parallel} (solid red curve) and E_{\perp} (dashed blue curve), replotted from Fig. 2(b). The dash-dotted (pink) and dotted (green) curves are for E_{\parallel} for the inner ring only and outer ring only, respectively.

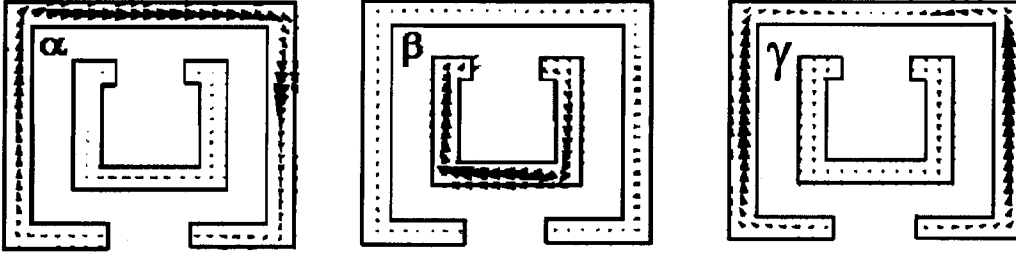


Figure 4.5 The surface current densities at frequencies which are indicated by dips α , β and γ , as seen in Figure 4.4.

The simulations of SRR #2 are replotted in Figure 4.4 (solid and dashed curves) where we labeled the first three low-frequency dips α , β , and γ , respectively. The calculated surface current densities corresponding to each of the dips, as seen in Figure 4.5, show that different electric modes are coupled to the double-ring SRRs. (The additional two unlabeled dips at higher frequencies in Figure 4.4 are due to higher-order electric modes, which are not relevant to the main ideas in this thesis.) α and γ are mainly from the contribution of the outer ring. This is consistent with a previous study (Padilla et al., 2006), which gave a complete interpretation of the EM response of the outer ring. What was not observed in the previous experimental studies is the dip β of around 35 THz, which is actually from the contribution of the inner ring. As seen in Figure 4.5, β is mainly caused by an oscillation of a circulating current in the inner ring. This is analogous to the circulating current in the outer ring at a lower frequency, as seen in Figure 4.5(α), which has been attributed to a LC resonance excited by the E component of the incident light via the asymmetry of the SRRs for E_{\parallel} (Linden et al., 2004). Analytically, the LC resonance frequency is determined by the dimensions of the SRR via (Soukoulis et al., 2006)

$$\omega_{LC} \sim \sqrt{G/WL^2}. \quad (4.1)$$

The LC resonance frequency of inner ring is estimated to be 1.8 times larger than that of the outer ring according to the dimensions obtained from the SEM. This is consistent with the corresponding experimental value of ~ 1.5 estimated from Figure 4.3(a) within the experimental errors. Furthermore, the numerically calculated transmission of the inner ring only and the outer ring only for E_{\parallel} in Figure 4.4 (dashed-dotted and dotted curves) also confirm that dip β results from the EM response of the inner ring. In the case of SRRs #1, according to Equation 4.1, the LC resonance in the outer ring is supposed to be located at a frequency 0.67 times lower than that of SRR #2, which agrees with the simulation results shown in Figure 4.2(b) and 4.3(b). The LC resonance in the inner ring of SRRs #1 for E_{\parallel} is absent in the data, which is in agreement with the simulation result where the corresponding feature is barely resolved.

As we know, at the frequency where the dip β is, a magnetic resonance in the inner ring, which corresponds to the magnetic-field excited LC resonance, could be excited as well if the H component of the incident light is perpendicular to the inner ring plane (Linden et al., 2004, Padilla et al., 2006). This yields a negative permeability [$\text{Re}(\mu) < 0$] just above the magnetic resonance frequency. On the other hand, our data show that when the E component is parallel to the symmetric arms of the SRR there is an electric resonance associated with the oscillations of the linear currents in the two arms of the outer ring, which is indicated by γ in Figure 4.4 (dashed curve) and Figure 4.5. This electric resonance is related to the plasmon resonance in the thin metallic continuous wires (Linden et al., 2004) that have been used to provide a negative permittivity [$\text{Re}(\epsilon) < 0$] (Shelby et al., 2001). Here, the electric resonance in the outer ring gives a negative $\text{Re}(\epsilon)$. In our double-ring SRR sample, the LC resonance in the inner ring and the electric resonance in the outer ring exist at similar frequencies, which suggests simultaneous $\text{Re}(\epsilon) < 0$ and $\text{Re}(\mu) < 0$

and, thus, $\text{Re}(n) < 0$ in a simple double-ring SRRs, without any additional metallic continuous wires.

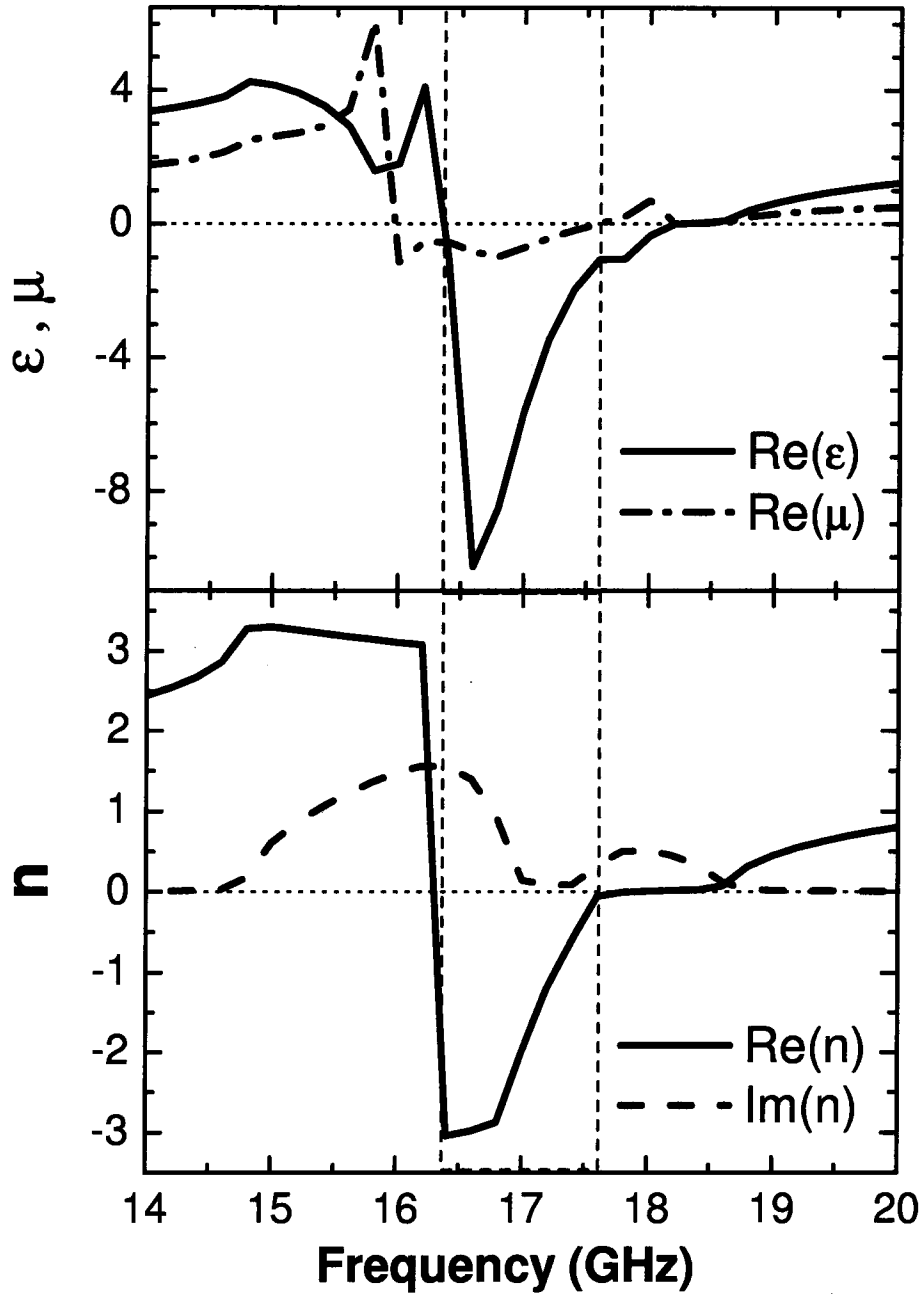


Figure 4.6 The retrieved effective parameters of the double-ring SRRs whose dimensions have been increased by 1000 times in order to increase the strength of the magnetic resonance in the inner ring.

To verify the above conjecture, we calculated the effective material parameters of the double-ring SRRs from the calculated S -parameters for the case where the H field is perpendicular to the SRRs plane and the E field is parallel to the symmetric arms of the SRRs by using a standard retrieval method (Smith et al., 2002). However, the retrieved effective μ showed that the magnetic resonance in the inner ring was not strong enough to give rise to a negative value of $\text{Re}(\mu)$ (not shown here) in our sample. This is due to the small filling factor of the inner ring in one unit cell (Rockstuhl et al., 2006), as well as the fact that the magnetic resonance amplitude is proportional to the size of the unit cell (Zhou et al., 2005). The filling factor of the inner ring cannot be significantly increased by reducing the periodicity since the outer ring surrounds the inner ring. In order to strengthen the magnetic resonance in the inner ring to achieve a negative $\text{Re}(\mu)$, we enlarged the whole unit cells by 1000 times and the resonance frequencies are reduced by 1000 times to the gigahertz range in the simulations. It turned out that the magnetic resonance in the inner ring became much stronger for the enlarged unit cell and a negative $\text{Re}(\mu)$ was achieved as shown in Figure 4.6. The retrieved $\text{Re}(\epsilon)$ is also present to be less than zero in a wide frequency regime in Figure 4.6. We should point out that, in the retrieval processes in the gigahertz range, the Si substrate has been removed. Silicon has no absorptions in the mid-infrared region; that's why we chose it as the substrate of our SRRs sample in the experiments. However, in terms of producing negative index of refraction, silicon is not a good choice for the substrates due to its high dielectric constant, which will give a background of $\text{Re}(\epsilon) \approx 11$ for the metamaterials. In Figure 4.6, the effective $\text{Re}(\epsilon)$ exhibits the pure effects of the electric resonance from the outer ring without a substrate. The gap width of the inner ring has been increased by 40% to optimize the results. When both $\text{Re}(\epsilon)$ and $\text{Re}(\mu)$ are less than zero, in the dashed box range, $\text{Re}(n)$ becomes negative. The antiresonance in $\text{Re}(\epsilon)$ due to the finite unit cell size is

present near the magnetic resonance (Koschny et al., 2003). For applications, a low ϵ material would be chosen for the substrates, but it may not affect our results shown in Figure 4.6 much.

In summary, we verified a left-handed behavior of the double-ring SRRs in the gigahertz frequencies by retrieving the effective parameters of the metamaterials. The left-handed behavior results from a combination of the magnetic resonance from the inner ring and an electric resonance from the outer ring. However, this idea breaks down in the mid-infrared frequencies since the magnetic resonance from the inner ring becomes very weak due to the small filling factor and the small size of the unit cell.

4.3.2 Left-Handed Behavior in A Single-Ring SRR Cubic Structure

In Section 4.3.1, a combination of the magnetic resonance in the inner ring and the electric resonance from the two parallel arms of the outer ring was verified to give rise to a left-handed behavior in the double-ring SRRs. In this section, the magnetic resonance will be combined with another mode of electric resonances, which is the E -field excited LC resonance of the SRRs to realize a left-handed behavior in a proposed single-ring SRR cubic structure.

Figure 4.7 shows one unit cell of the proposed metamaterial, which consists of two single-ring SRRs on two orthogonal faces of a cube. The dimensions of the single-ring SRRs are similar to those of the outer ring of the double-ring SRRs in a previous design, which was the first experimental verification of the negative index of refraction (Smith et al., 2005, Shelby et al., 2001). The dimensions of our design were chosen to be similar to the previous design on purpose in order to demonstrate the feasibility of fabrication. Compared to the design of Shelby *et al.*, our structured metamaterial does

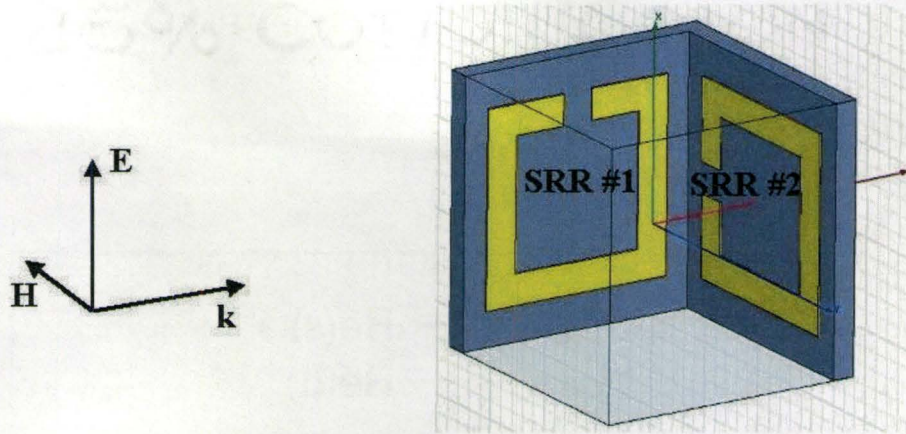


Figure 4.7 One unit cell of the single-ring SRR cubic structure and the configuration of the incident EM wave.

not contain any continuous wires and the wire media is replaced with another single-ring SRR, which gives rise to a negative $\text{Re}(\epsilon)$ due to the E -field excited LC resonance in it. We would show in following, based on the simulations, that our simplified design has a pronounced left-handed behavior as well. With the configuration of the incident light shown in Figure 4.7, SRR 1 has a magnetic resonance related to the H -field excited LC resonance which leads to a negative $\text{Re}(\mu)$. Meanwhile, SRR 2 gives a negative $\text{Re}(\epsilon)$ as the E field is parallel to its gap and excites the LC resonance in it. A modified full S -parameter retrieval method for asymmetric structures (Smith et al., 2005) was used to obtain the effective material parameters, as seen in Figure 4.8. In the dashed box regime, negative values for $\text{Re}(n)$, $\text{Re}(\epsilon)$, and $\text{Re}(\mu)$ are present, which correspond to left-handed behavior. The gap width of SRR 1 is slightly larger than that of SRR 2 to enlarge the frequency regime where $\text{Re}(\epsilon) < 0$ and $\text{Re}(\mu) < 0$ overlap, since a larger gap of the split ring results in a smaller capacitance and, therefore, increases the LC resonance frequency. The amplitude of $\text{Im}(n)$ is relatively small compared to the real part, which suggests a low loss in the proposed left-handed metamaterial.

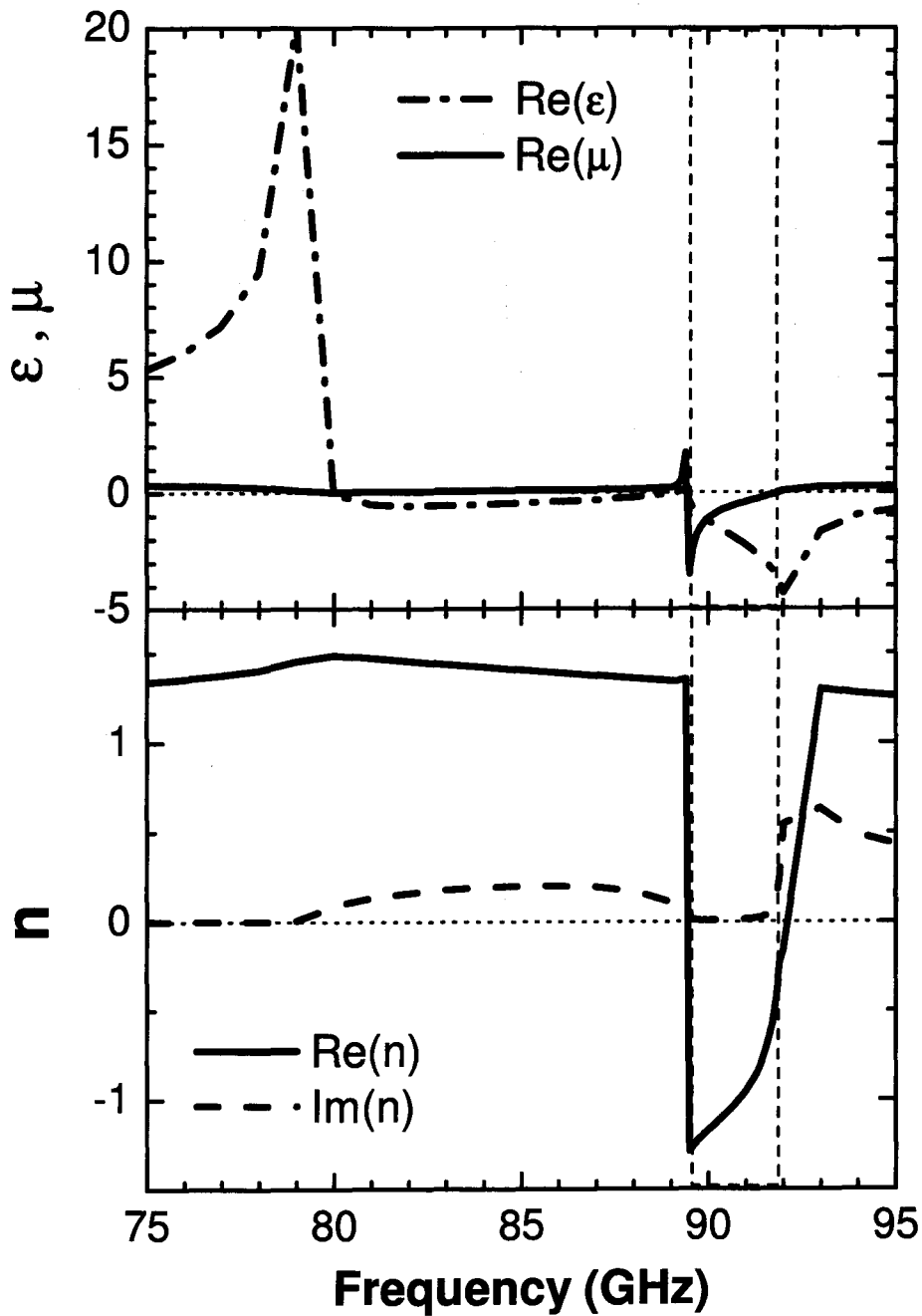


Figure 4.8 The retrieved effective parameters of the proposed single-ring SRR cubic structure.

The proposed metamaterial has a simpler structure than the previous designs (Shelby et al., 2001) in the microwave frequencies and avoids using any continuous metallic wires. The LC resonances in the two single-ring SRRs are fairly strong and can guarantee negative values for $\text{Re}(\epsilon)$ and $\text{Re}(\mu)$ up to very high frequencies (Enkrich et al., 2005).

4.4 Summary

In conclusion, different from in the conventional designs of SRR left-handed metamaterials that contains continuous wires, the electric resonances of the SRR itself, instead, provide a negative effective $\text{Re}(\epsilon)$ in our designs. In the case of double-ring SRRs, a combination of the electric resonance from the two parallel arms of the outer ring and the magnetic resonance from the inner ring results in a left-handed behavior in the double-ring SRRs. In the proposed single-ring SRR metamaterial, the electric and magnetic resonances that originate from the E - and H -field excited LC resonances in two single-ring SRRs, respectively, give rise to a left-handed behavior. We verified from numerical simulations that these two devices are both working well at low frequencies. However, for higher frequencies, the first case becomes impractical due to the weakened magnetic resonance from the inner ring. Note that, there is no coupling between the electric and magnetic responses in our designs.

Chapter 5

Bosonic Spectra of Highly Underdoped Y123

5.1 Introduction

This chapter elaborates on the experimental results of the highly underdoped Y123 sample and the numerical inversion of the optical scattering rate based on Sharapov's formula. The optical properties of the highly underdoped Y123 are compared with those of the ortho-II Y123 as well. Section 5.2 shows the annealing processes taken to lower the T_c of the original sample to 18 K. The experimental results and the model fits are included in Section 5.3. Finally, Section 5.4 gives the conclusions.

5.2 Annealing Processes

The YBCO_{6.35} single crystal was grown by a self-flux method (Liang et al., 2002). The original sample had a T_c around 26.6 K, 8.6 K higher than what we are interested in, since we want to compare our results with those of neutron scattering by

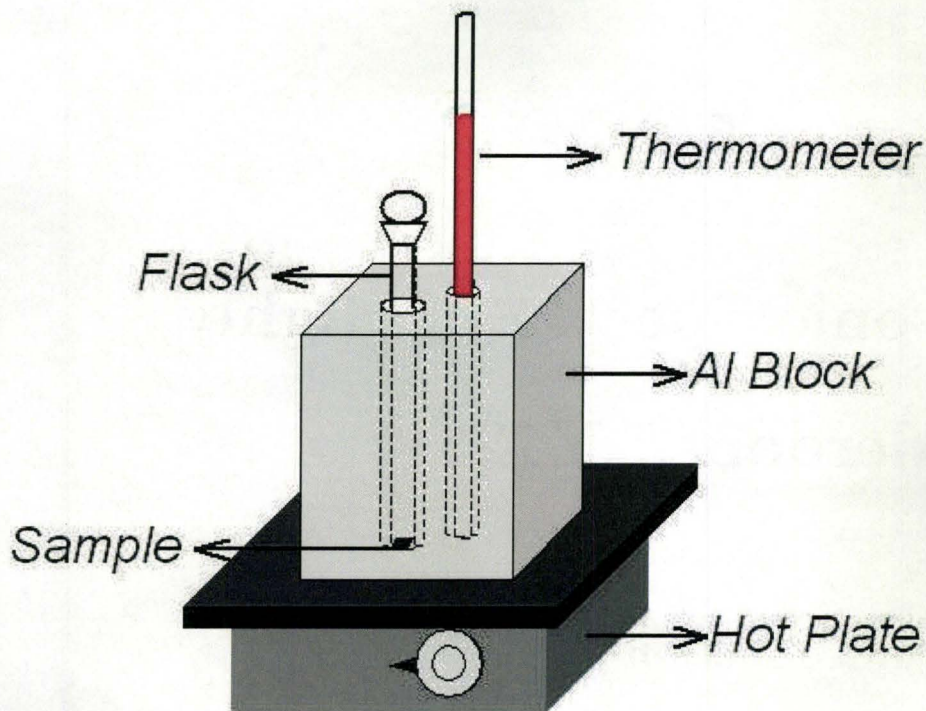


Figure 5.1 Sketch of the home-made annealing facility.

Stock *et al.* (Stock *et al.*, 2006) and on a sample from the same source but with a $T_c=18$ K. However, as mentioned in the preceding chapter, the transition temperature T_c of $\text{YBCO}_{6.35}$ can be tuned by the annealing temperature through varying the degree of the oxygen ordering in the Cu-O chain layers. We successfully lowered the T_c to 18 K by annealing in two steps. Figure 5.1 shows the home-made facility used for annealing. An aluminum block drilled with two cylinder-shape cavities is located on top of a hot plate. One of the cavities is for holding the glass flask containing a piece of sample and the other one is where a thermometer is located for calibrating the temperature of the sample. While annealing, the flask is filled with Argon to avoid a change of oxygen concentration in the sample. A previous study showed a decrease of T_c as a function of annealing temperatures, for a higher content of oxygen, *i.e.* 6.45, as shown in Figure 5.2. We shift the curve downwards to cross the point which represents our

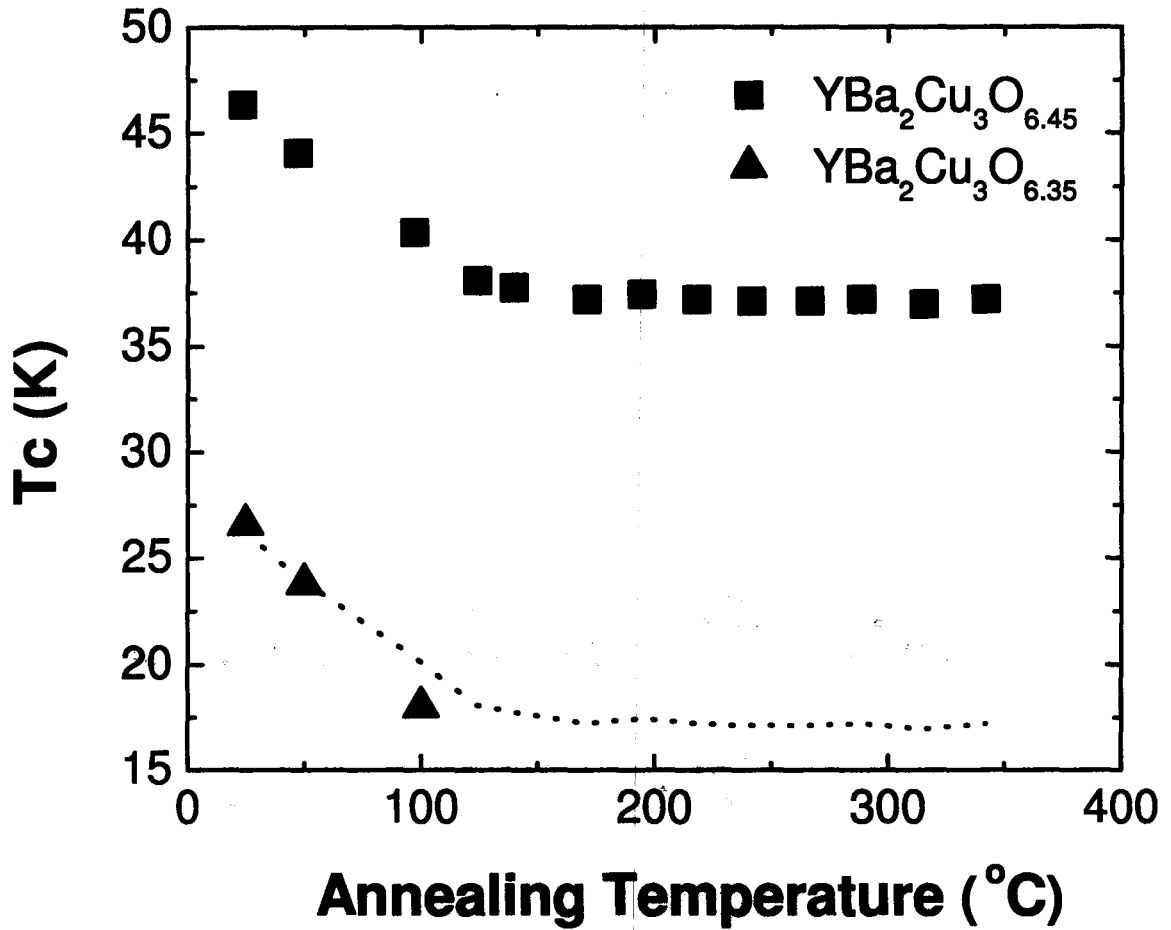


Figure 5.2 The transition temperature T_c as a function of the annealing temperature for $\text{YBCO}_{6.45}$ (Veal et al., 1990) (squares) and our $\text{YBCO}_{6.35}$ sample (triangles). The dotted line is a parallel shift of the literature curve for $\text{YBCO}_{6.45}$.

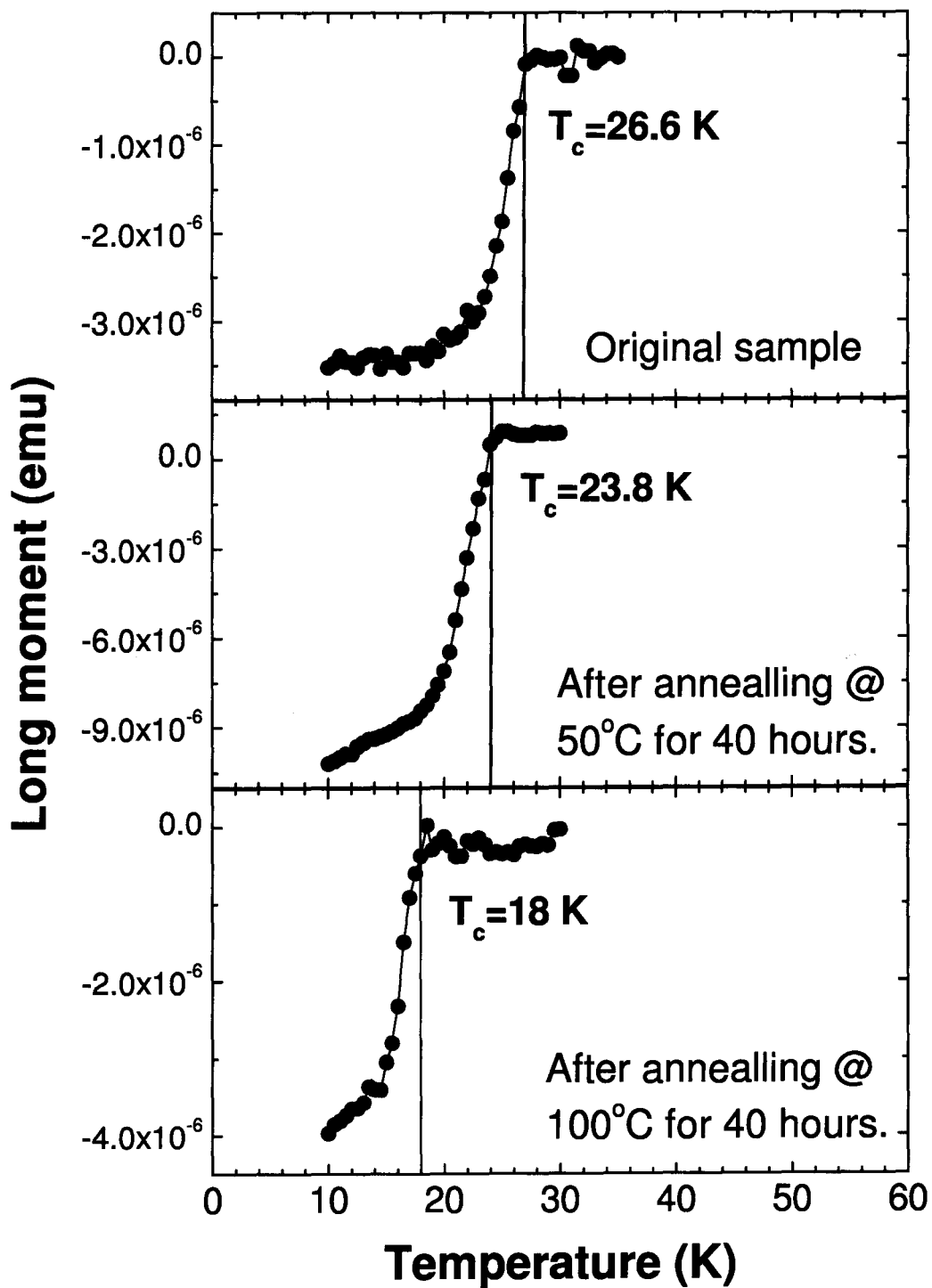


Figure 5.3 The magnetic susceptibilities of the original YBCO123 sample and the sample annealed at two different temperatures.

original sample of $\text{YBCO}_{6.35}$ where $T_c=26.6$ K and the annealing temperature is 25 °C, as shown by the dotted curve in Figure 5.2. The shifted curve is used as a guide for our annealing process. Firstly, the sample was annealed at 50 °C for about 40 hours and then quenched to -20 °C. After this process, the T_c of the sample was found to be 23.8 K in the magnetic susceptibility measurement. This result approximately follows the shifted curve of annealing. Further, in the second step, the sample was annealed again, but at a higher temperature, *i.e.* 100 °C, for another 40 hours, and quenched as well. After these two annealing steps, we were able to lower the T_c to 18 K. Figure 5.3 shows the magnetic susceptibility measurements of the original sample and the sample after two annealing steps.

However, in order to keep the T_c at 18 K, the sample had to be kept at a temperature below the freezing temperature of water at all times during the optical measurements. When no measurements were being performed, the sample was kept in a freezer and during the optical measurements, the sample temperature was kept below 0 °C in the flow cryostat.

5.3 The Experimental Results

The $\text{YBCO}_{6.35}$ sample has an area of about 1.5 mm². The reflectance of $\text{YBCO}_{6.35}$ is anisotropic in the ab -plane, which reaches a maximum along the b -axis due to the ordering of Cu-O chains and a minimum along the a -axis. We use the reflectance anisotropy as a criterion to orient our sample for measurements with $E||a$. Figure 5.4(a) shows the a -axis reflectance data of the highly underdoped $\text{YBCO}_{6.35}$ sample at 9 different temperatures, all above T_c . For this sample, our equipment restricts us to the normal state. Four transverse optical phonons are discernible in the spectra at low frequencies as seen in Figure 5.4(b). By performing KK transformations

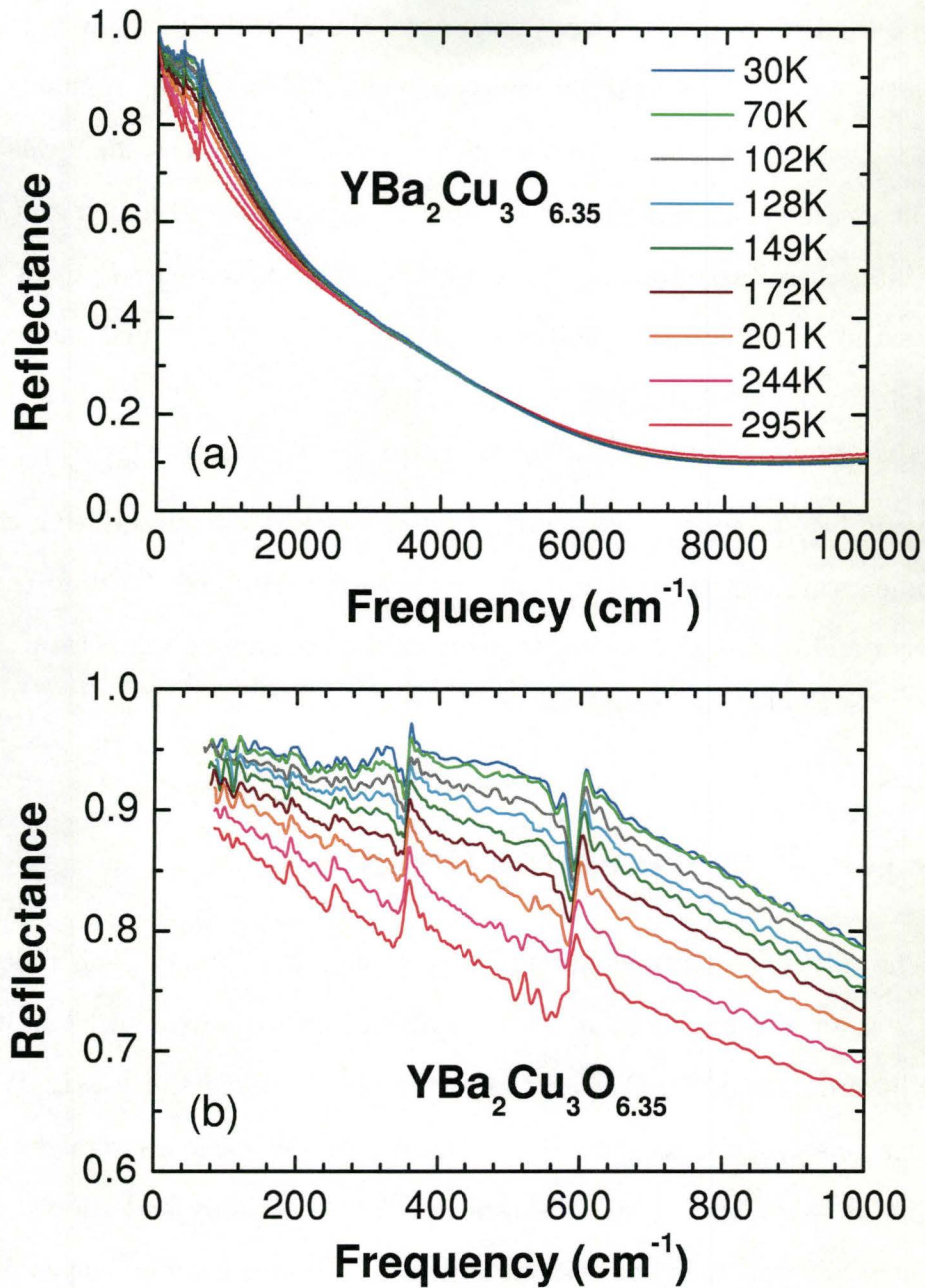


Figure 5.4 (a) a -axis reflectance data of the highly underdoped $\text{YBCO}_{6.35}$ sample at 9 different temperatures above T_c , up to 10,000 cm^{-1} . (b) The expanded view of the low-frequency reflectance. Note that even at the lowest temperature, the reflectance is only 0.95, evidence of strong elastic scattering. The sharp features are due to transverse optical phonons.

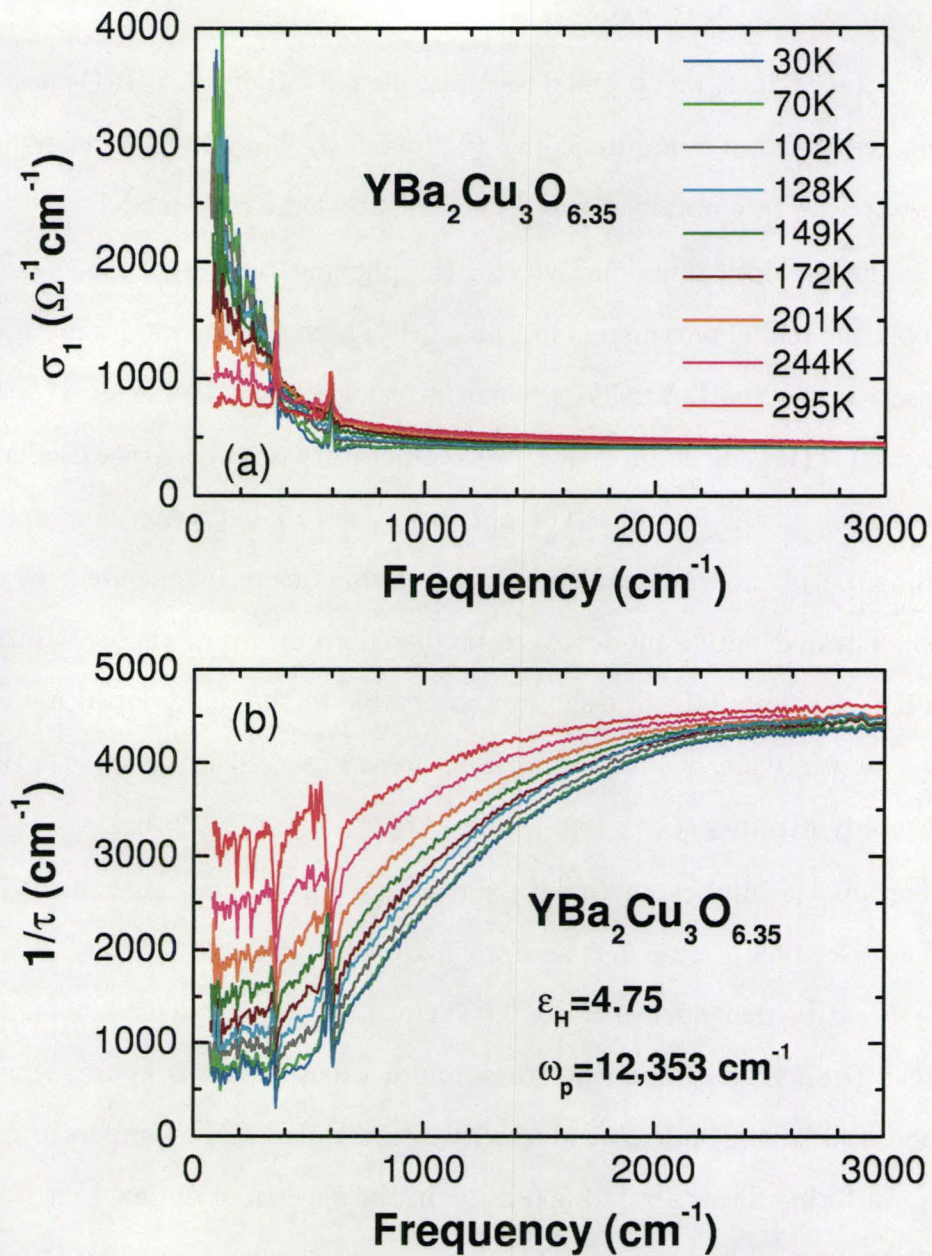


Figure 5.5 The optical conductivity (a) and the optical scattering rate (b) of the highly underdoped $\text{YBCO}_{6.35}$ sample at 9 different temperatures above T_c .

on the reflectance data, we obtained the optical conductivity of $\text{YBCO}_{6.35}$ at different temperatures as shown in Figure 5.5(a). Figure 5.5(b) shows the frequency-dependent optical scattering rate obtained based on the extended Drude model.

We fit the optical conductivity of the phonons with a Drude-Lorentz model and display the model parameters in Table 5.1. These phonon modes are identical to those observed in ortho-II $\text{YBCO}_{6.50}$ which has a higher hole doping level ($p=0.09$) and higher $T_c=59$ K (Hwang et al., 2006a). As temperature is reduced, the oscillator width gets smaller for all the four observed phonons, due to less thermal fluctuations. The strength of the phonon modes, however, are temperature independent as expected. While six infrared active modes were predicted from group theory (Burns et al., 1987) for $E \perp c$, only four of them are observable in the underdoped materials, *i.e.* $\text{YBCO}_{6.35}$ and $\text{YBCO}_{6.50}$, and five of them were observed in undoped YBCO_6 in a previous study (Tajima et al., 1991).

For a better understanding of the features, the phonons are removed from the spectra as seen in Figure 5.6. The optical conductivity and scattering rate barely show temperature dependence above $2,000 \text{ cm}^{-1}$. At low frequencies, as temperature lowers, the Drude-like component grows and a valley develops at frequencies above the Drude peak in the optical conductivity. Meanwhile, at low temperatures, a sharp onset of scattering forms around 560 cm^{-1} in the spectra of optical scattering rate.

Figure 5.7 displays a comparison of the optical scattering rate of $\text{YBCO}_{6.35}$ and $\text{YBCO}_{6.50}$. Note that, at $T=28$ K, $\text{YBCO}_{6.50}$ is in the superconducting state which we ignore for the comparison. There are three notable differences in these two sets of spectra. First of all, the scattering rate at high frequencies is flatter for the highly underdoped sample $\text{YBCO}_{6.35}$, resulting from a larger ϵ_H . Second, $\text{YBCO}_{6.35}$ has a better defined onset of scattering at low temperatures. Last but not least, there is a residue of about 500 cm^{-1} in the optical scattering rate of $\text{YBCO}_{6.35}$ at the lowest

Table 5.1 Parameters of the Drude-Lorentz model fit at different temperatures for the YBCO_{6.35} sample. $\epsilon_\infty = 4.75$. $\omega_{p,D}$ and Γ_D represent the plasma frequency and scattering rate in the Drude mode, while ω_k , $\omega_{p,k}$ and Γ_k are center frequency, strength and width of the k th Lorentz oscillator.

Temperature		295 K	244K	201 K	172 K	149 K	128 K	102 K	70 K	30 K
Drude (cm ⁻¹)	$\omega_{p,D}$	8,160	7,350	7,100	6,850	6,560	6,530	6,530	6,530	6,530
	Γ_D	1,430	900	650	500	360	320	270	220	200
Phonons (cm ⁻¹)	$\omega_{p,1}$	286.5	289	300	302	322	328	367	358	377
	ω_1	188	189	189.3	189.8	189	189.8	188.9	187.5	188.5
	Γ_1	7.5	7	6.5	6	5.5	5.5	6	6	6
	$\omega_{p,2}$	356	317	277	365	349	400	409	445	539
	ω_2	251.4	249.7	251.5	250	250	251	251.3	250.8	251.3
	Γ_2	11	8	8	9.5	9.5	11.5	9	9	9
	$\omega_{p,3}$	608	639	616	575	590	604	605.9	623	580
	ω_3	353.5	354.5	354	354.5	354.5	354.5	354.5	354	354.6
	Γ_3	15	12.5	10	8	7	7	7	6.5	6.5
	$\omega_{p,4}$	717	515	523	541	639	625	656	666	643.0
	ω_4	585	589	592	593.5	594.1	595.4	596.8	596.8	596.8
	Γ_4	22	14	13	12.5	15	15	14.5	14.5	14.0

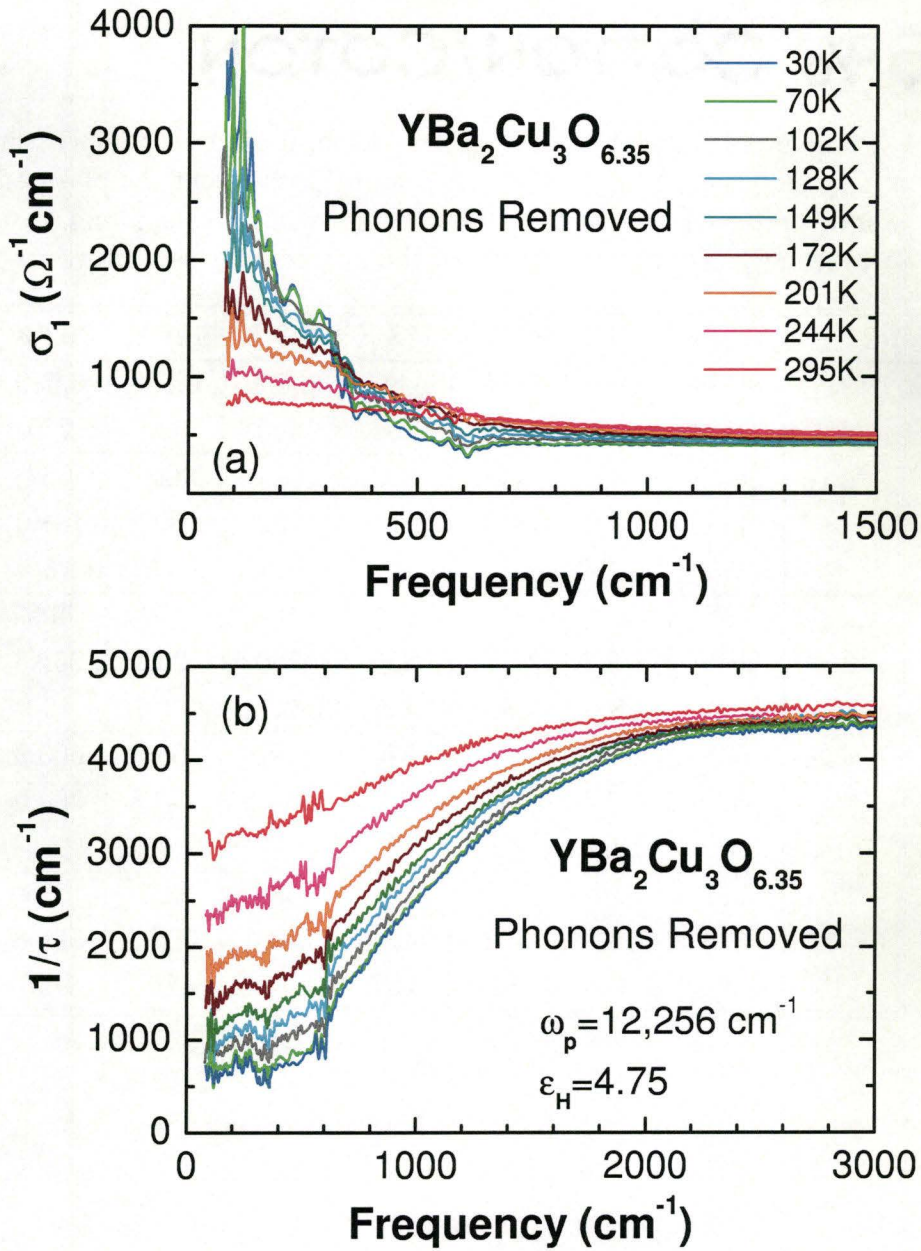


Figure 5.6 The optical conductivity (a) and the optical scattering rate (b) of the highly underdoped $\text{YBCO}_{6.35}$ sample at different temperatures above T_c , after the phonons have been removed.

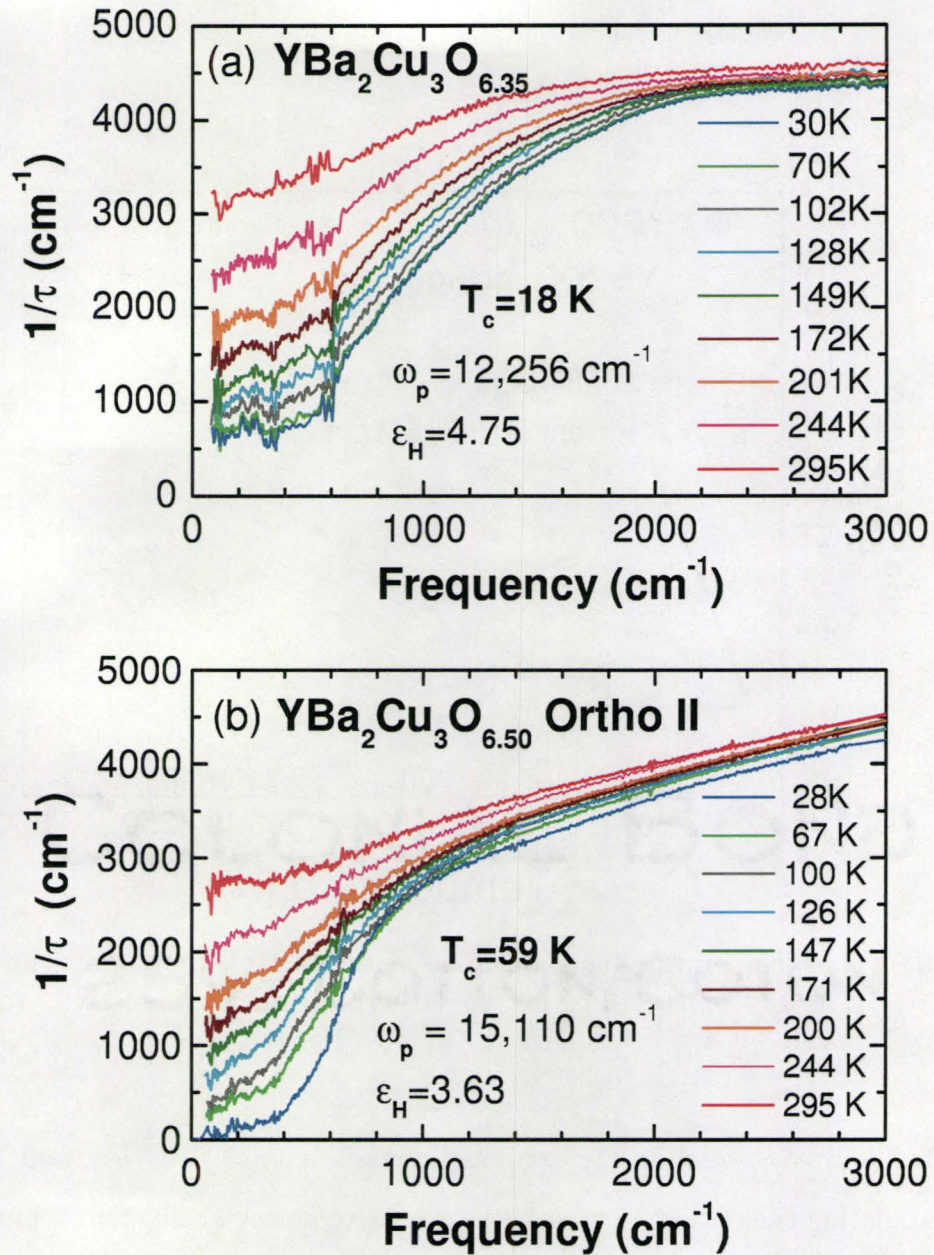


Figure 5.7 A comparison of the optical scattering rate between $\text{YBCO}_{6.35}$ (a) and ortho-II $\text{YBCO}_{6.50}$ (Hwang et al., 2006a) (b) at different temperatures, with phonons removed. Note that, at $T=28 \text{ K}$, $\text{YBCO}_{6.50}$ is in the superconducting state.

temperature.

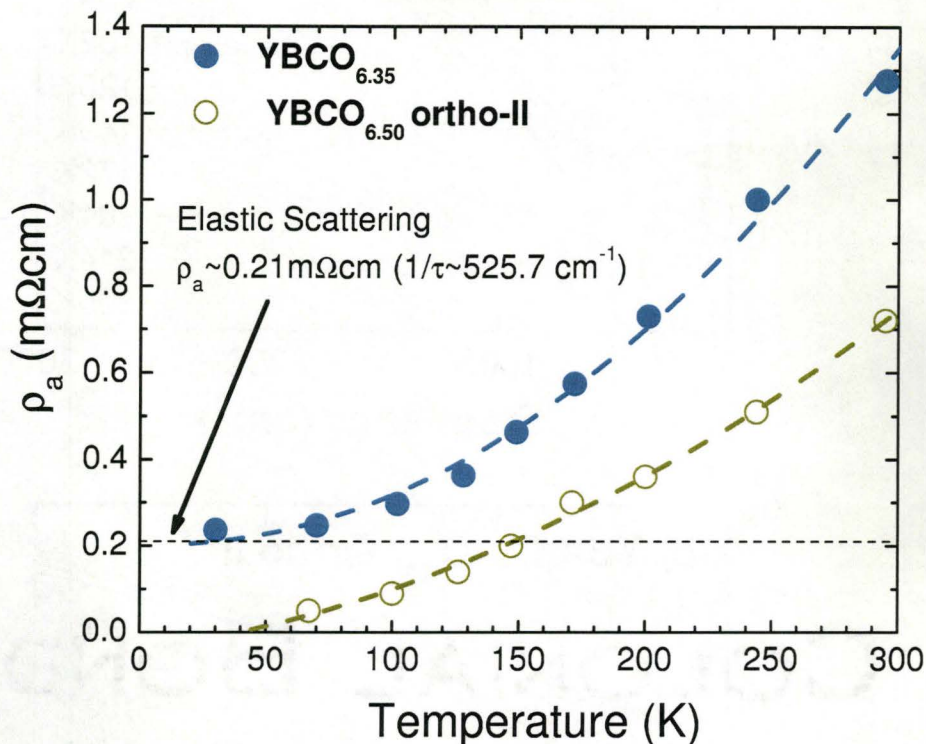


Figure 5.8 The temperature-dependent dc resistivity of the highly underdoped YBCO_{6.35} extracted by extrapolating the optical conductivity to zero frequency.

In Figure 5.8, we show the extracted dc resistivity of YBCO_{6.35} and YBCO_{6.50} by extrapolating the optical conductivity to zero frequency at different temperatures. The low-temperature extrapolation of the curve for YBCO_{6.35} has a residual resistivity of about 0.21 mΩ·cm at $T=0$, which corresponds to strong elastic scattering in the highly underdoped sample. Recent microwave spectroscopy studies on YBCO_{6.35} also indicated a residual dc resistivity about 0.20 mΩ·cm (Broun, 2008), which completely agrees with our result. Such consistency provides us strong evidence for the accuracy of our reflectance data. The elastic scattering gives rise to the residue in the optical scattering rate in Figure 5.7(a), which is estimated to be $1/\tau_{\text{elastic}} \sim 525.7 \text{ cm}^{-1}$. We

presume that the elastic scattering in $\text{YBCO}_{6.35}$ is due to the O disordering in the Cu-O chains. In agreement with this view, there is no elastic scattering in $\text{YBCO}_{6.50}$ since it has completely ordered Cu-O chains.

5.4 Model Fits of $1/\tau(\omega)$ and Discussion

We use the analytic formula derived by Sharapov as shown in Equation 3.21 to extract the electron-boson spectral function from the optical scattering rate of $\text{YBCO}_{6.35}$. The elastic scattering $1/\tau_{\text{elastic}} \sim 525.7 \text{ cm}^{-1}$ as determined in the preceding section is taken into account in Equation 3.23. In our model, the electron-boson spectral function $I^2\chi(\Omega)$ is described by $I^2\chi(\Omega) = PK(\Omega) + BG(\Omega)$, a bosonic mode plus a broad background. The mode is described by a Gaussian function,

$$PK(\Omega) = \frac{A}{\sqrt{2\pi}(d/2.35)} e^{-(\Omega - \Omega_{\text{mode}})^2 / [2(d/2.35)^2]}, \quad (5.1)$$

where A , Ω_{mode} , and d represent the area, center frequency, and width of the Gaussian peak. The width of the Gaussian peaks at different temperatures are assumed to be same and are taken to be 25 cm^{-1} based on the shape of the central mode at $T=30 \text{ K}$ in neutron studies (Stock et al., 2006). Our calculations based on the above model reveal that the onset frequency (ω_{onset}) of resulting $1/\tau(\omega)$ is determined by $\omega_{\text{onset}} = \Omega_{\text{mode}} + \Delta_{\text{pg}}$. For example, as shown in Figure 5.9, as we shift the Gaussian peak to higher frequencies, the onset of resulting $1/\tau$ curves also moves towards higher frequencies in a same amount. In our model fitting, we take the size of pseudogap $\Delta_{\text{pg}} \approx 550 \text{ cm}^{-1}$ estimated from the review paper (Hüfner et al., 2008) and the position of the central mode in the local magnetic spin susceptibility spectrum determined by neutron studies (Stock et al., 2006) and end up with an excellent fit to the sharp onset

of the optical scattering rate, *e.g.* for $T=30$ K, as shown by the triangle symbols in Figure 5.9. What should be mentioned is that, since Equation 3.21 diverges if $I^2\chi(\Omega = 0) \neq 0$, the Gaussian peak centered at 0 cm^{-1} for the bosonic mode is cut off at 5 cm^{-1} to avoid diverging results. Therefore, the bosonic mode in the calculations actually peaks at 5 cm^{-1} or 0.6 meV . In the calculations, the parameter α , related to the shape of the pseudogap as shown in Equation 3.22, is taken to be 8 based on the curvature of the experimental data of $1/\tau(\omega)$ below 800 cm^{-1} or 100 meV . In figure 5.9, the deviation of the calculated $1/\tau(\omega)$ with triangle symbols from the data above 150 meV is due to the contribution from the broad background that is not included in the $I^2\chi(\Omega)$ in this calculation. Neutron studies (Stock et al., 2006) do not provide enough information on the background of the spin susceptibility spectra at high frequencies, namely above 30 meV or 240 cm^{-1} . Therefore in our model fit, the background in $I^2\chi(\Omega)$ at different temperatures are described by the simple Heaviside step functions as

$$BG(\Omega) = H_1 \cdot \theta(\Omega - \Omega_1)\theta(\Omega_2 - \Omega) + H_2 \cdot \theta(\Omega - \Omega_3)\theta(\Omega_4 - \Omega), \quad (5.2)$$

where $H_{1 \text{ or } 2}$ and $\Omega_{1,2,3 \text{ or } 4}$ are the height and the beginning or end of each step function. To summarize, in the model fits, all of the parameters are adjustable and can be determined by fitting to the optical data of $1/\tau(\omega)$, except for the mode width and the size of the pseudogap Δ_{pg} which are put in by hand.

Figure 5.10(a) shows the bosonic spectra $I^2\chi(\Omega)$, including the low-frequency bosonic mode and the broad background, at different temperatures. And the resulting fits to the optical scattering rate are displayed in Figure 5.10 (b). The inset exhibits a rapid growth of the mode intensity as the temperature is lowered. The parameters of the Gaussian functions for the bosonic mode ($PK(\Omega)$) and the Heaviside step

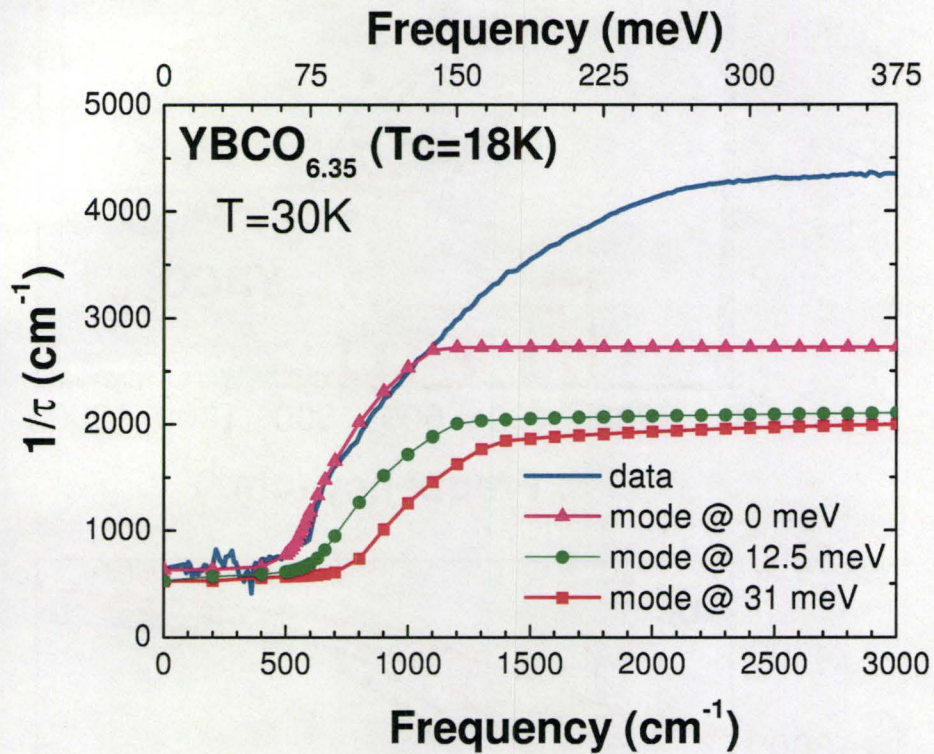


Figure 5.9 The model fittings to the experimental data of optical scattering rate at $T=30$ K with only bosonic mode in $I^2\chi(\Omega)$. A shift of the mode position results in an equivalent shift of the onset frequency of the resulting $1/\tau(\omega)$.

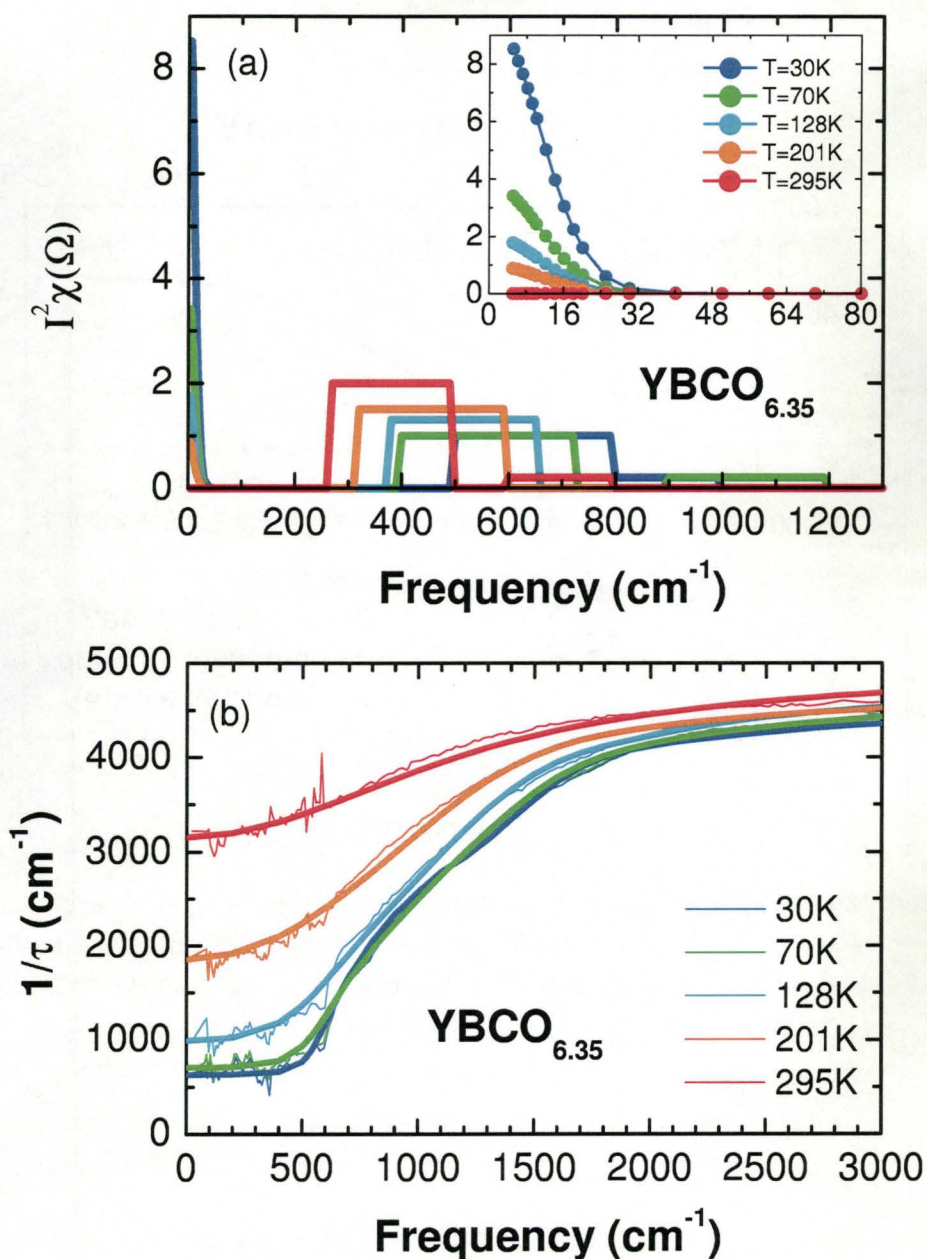


Figure 5.10 (a) The bosonic spectra of $\text{YBCO}_{6.35}$ at different temperatures. Inset shows an expanded view of the low-frequency mode. (b) The resulting fits to the optical scattering rate.

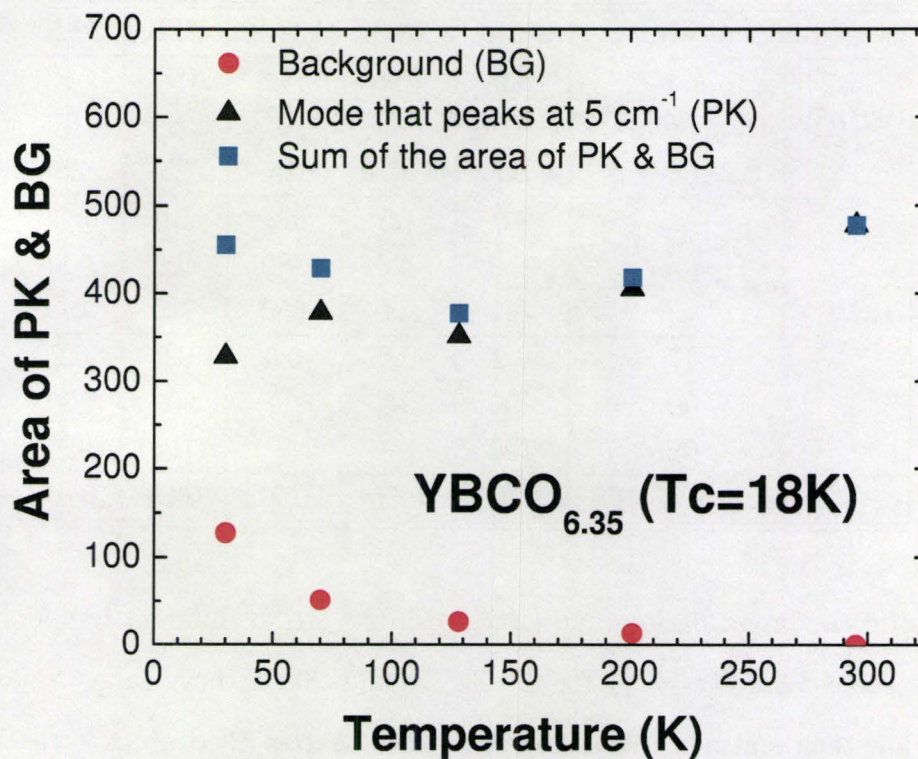


Figure 5.11 The area of the mode that peaks at 5 cm^{-1} , the area of the step-like background, and the total area of $I^2\chi(\Omega)$ shown in Figure 5.10.

Table 5.2 Parameters of the Gaussian functions for the bosonic mode (PK(Ω)) and the Heaviside step functions for the broad background (BG(Ω)) in $I^2\chi(\Omega)$ at different temperatures. $1 - N(z = 0)$ is the depth of the pseudogap at Fermi surface in the density of state.

Temperature		295 K	201 K	128 K	70 K	30 K
PK(Ω)	A	0.0	26.5	53.0	102.0	255.0
	Ω_{mode} (cm^{-1})	0	0	0	0	0
	d (cm^{-1})	25	25	25	25	25
BG(Ω)	H_1	2.0	1.5	1.3	1.0	1.0
	Ω_1 (cm^{-1})	270	320	380	400	500
	Ω_2 (cm^{-1})	490	590	650	720	790
	H_2	0.2	0.0	0.0	0.2	0.2
	Ω_3 (cm^{-1})	600	—	—	900	800
	Ω_4 (cm^{-1})	790	—	—	1,190	990
$N(z = 0)$		0.98	0.50	0.21	0.09	0.05

functions for the broad background (BG(Ω)) in $I^2\chi(\Omega)$ at different temperatures are listed in Table 5.2. $N(z = 0)$ for $T=201$ K and 295 K have larger uncertainties than for low temperatures. We assume the pseudogap is filled up as T reaches room temperature. In Figure 5.11, we plot the area of the mode that peaks at 5 cm^{-1} and the area of the step-like background in $I^2\chi(\Omega)$ and the sum of those two components as well, calculated based on the parameters shown in Table 5.2. As temperature goes up, the spectral weight (proportional to the area) of the mode reduces whereas the spectral weight of the broad background grows. The total spectral weight of those two components of $I^2\chi(\Omega)$ is approximately conserved up to $1,200 \text{ cm}^{-1}$.

Figure 5.12 illustrates comparisons between the bosonic mode of $I^2\chi$ determined by our study and the central mode of the local magnetic spin susceptibility spectrum determined by neutrons (Stock et al., 2006). The two modes have similar shapes, and the intensity of the modes as a function of temperature also follow

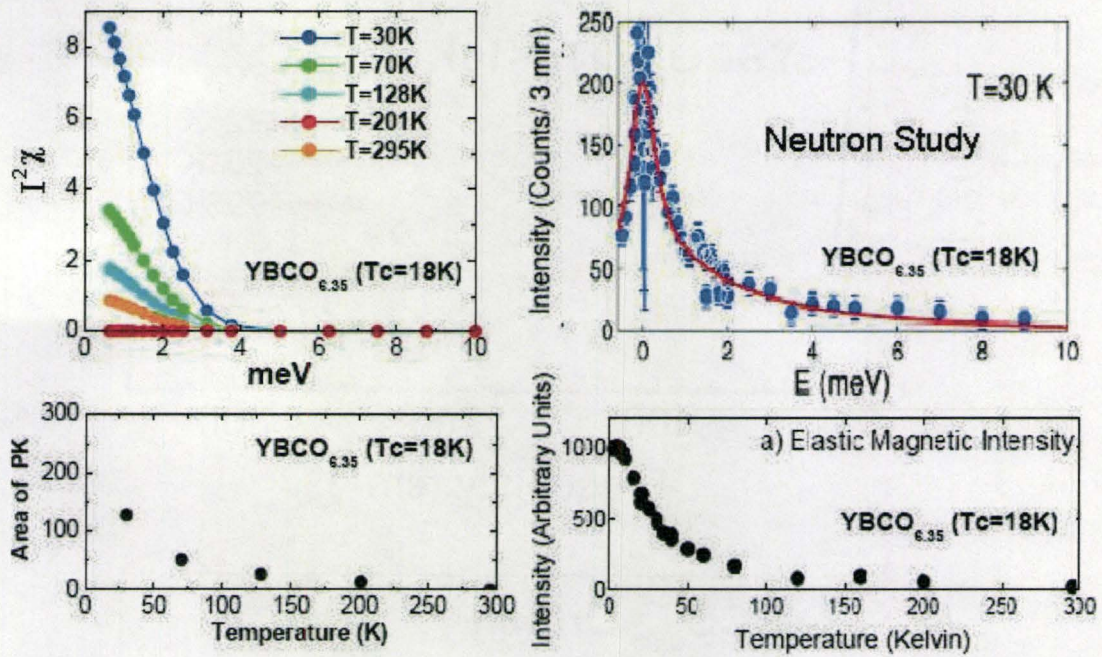


Figure 5.12 Comparisons between the bosonic mode of $I^2\chi$ determined by our study (left panels) and the central mode of the local magnetic spin susceptibility spectrum determined by neutrons (right panels) (Stock et al., 2006, 2008).

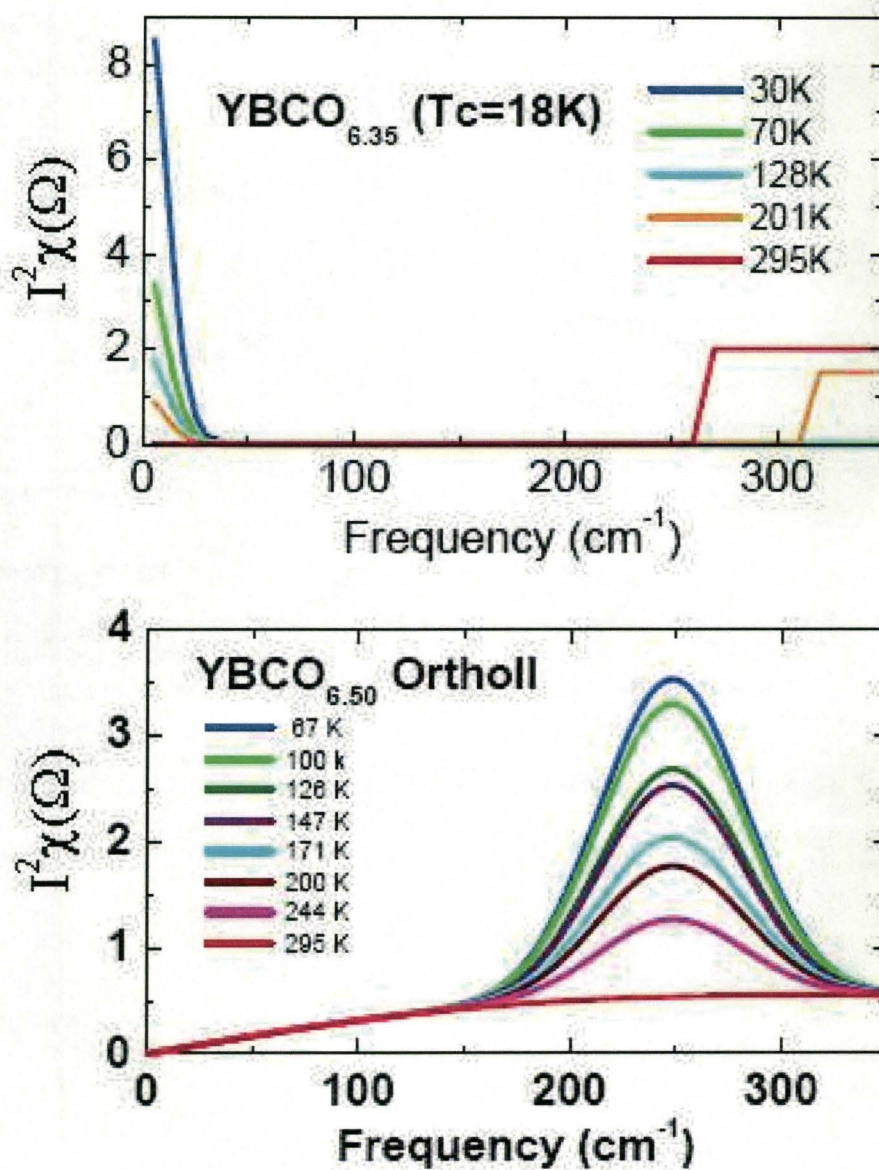


Figure 5.13 A comparison of the Bosonic spectral density of the YBCO_{6.35} (a) and the ortho-II YBCO_{6.50}.

similar trends. When we compare our data for $\text{YBCO}_{6.35}$ to the bosonic spectra of $\text{YBCO}_{6.50}$, which is also underdoped system, we see dramatic differences. Figure 5.13 shows the neutron mode at 31 meV in $\text{YBCO}_{6.50}$ disappears completely in the highly underdoped YBCO system.

5.5 Summary

The optical scattering rate of highly underdoped $\text{YBCO}_{6.35}$ is dominated by a bosonic mode situated at very low frequencies, opposed to the bosonic mode that locates at 31 meV in $\text{YBCO}_{6.50}$. The intensity of the low-frequency mode grows rapidly as temperature reduces and the characteristics of this mode are consistent with the central mode in the neutron scattering studies.

Chapter 6

Bosonic Spectra of Optimally doped Hg1201 and Hg1223

6.1 Introduction

In this chapter, we focus on the optical properties of the optimally doped Hg1201 sample. The experimental results are given in Section 6.2. Section 6.3 shows the bosonic spectra as a function of temperature as obtained by the maximum entropy inversion technique mentioned in Section 3.3.2, as well as a comparison of the bosonic spectra between monolayer Hg1201 and trilayer Hg1223.

6.2 The Experimental Results

The nearly optimally doped Hg1201 single crystal used was grown by a flux growth technique (Colson, 2008). It was a $1.0 \times 1.0 \text{ mm}^2$ platelet with a well oriented *ab*-plane. Figure 6.1(a) shows the reflectance data of Hg1201 at eight different temperatures, three of which are in the superconducting states. As the temperature

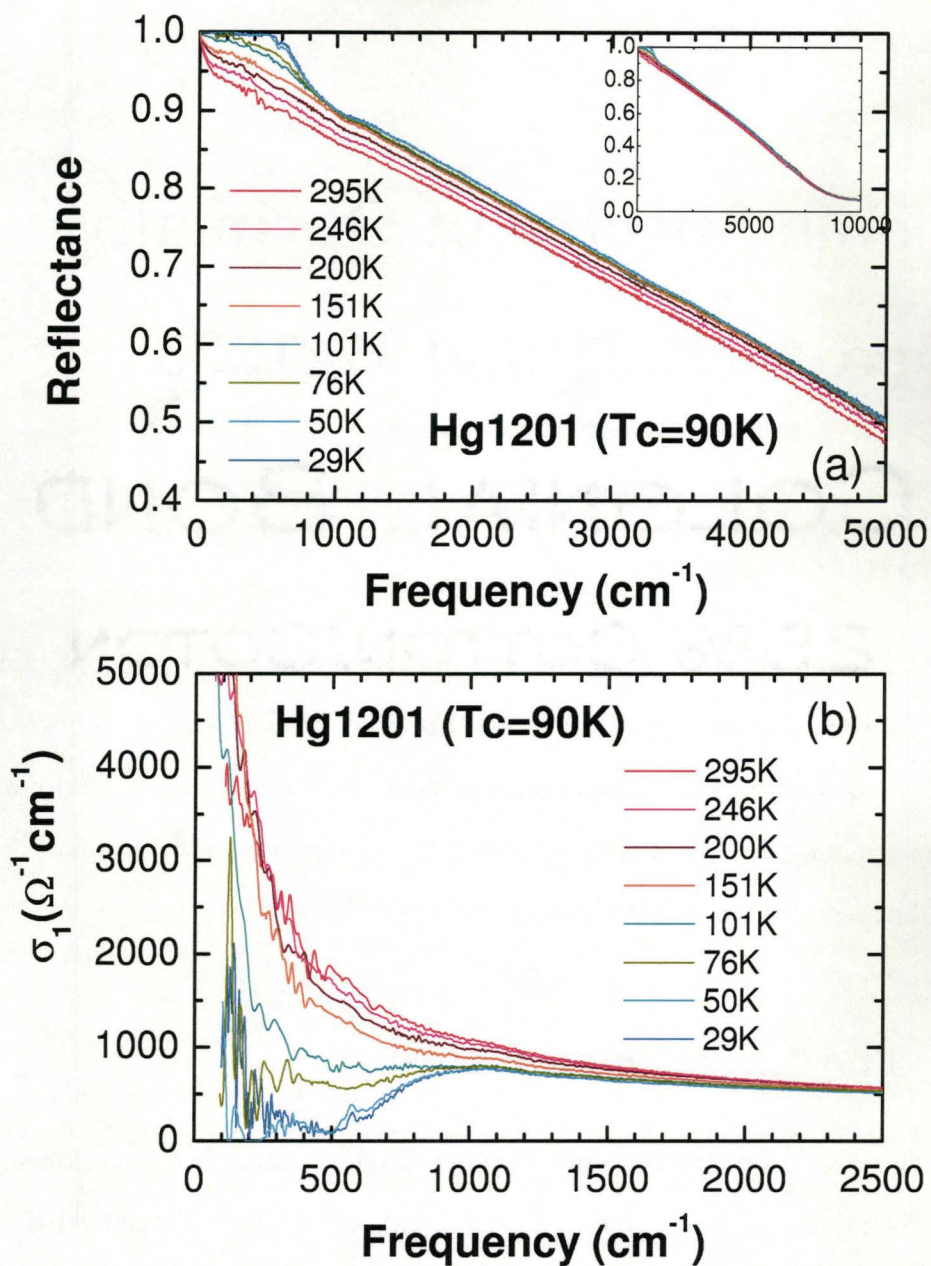


Figure 6.1 The reflectance (a) and optical conductivity spectra (b) of Hg1201 at eight different temperatures. The inset shows the overview of reflectance up to 10,000 cm^{-1} .

is reduced below $T_c=90$ K, a shoulder-like feature grows in the reflectance at low frequencies. Above $1,000\text{ cm}^{-1}$, the reflectance curves decrease monotonically until it reaches a minimum at the plasma edge around $10,000\text{ cm}^{-1}$. No obvious transverse optical phonons are observed in Hg1201. Through the KK transformation of reflectance data, we obtain the temperature-dependent optical conductivity spectra as displayed in Figure 6.1(b). Note that a valley develops in a frequency region below $1,000\text{ cm}^{-1}$ as temperature is lowered and which tends to become a complete gap when the system becomes superconducting. The Drude-like peak becomes narrower as temperature decreases. The temperature dependence is much less significant above $1,000\text{ cm}^{-1}$.

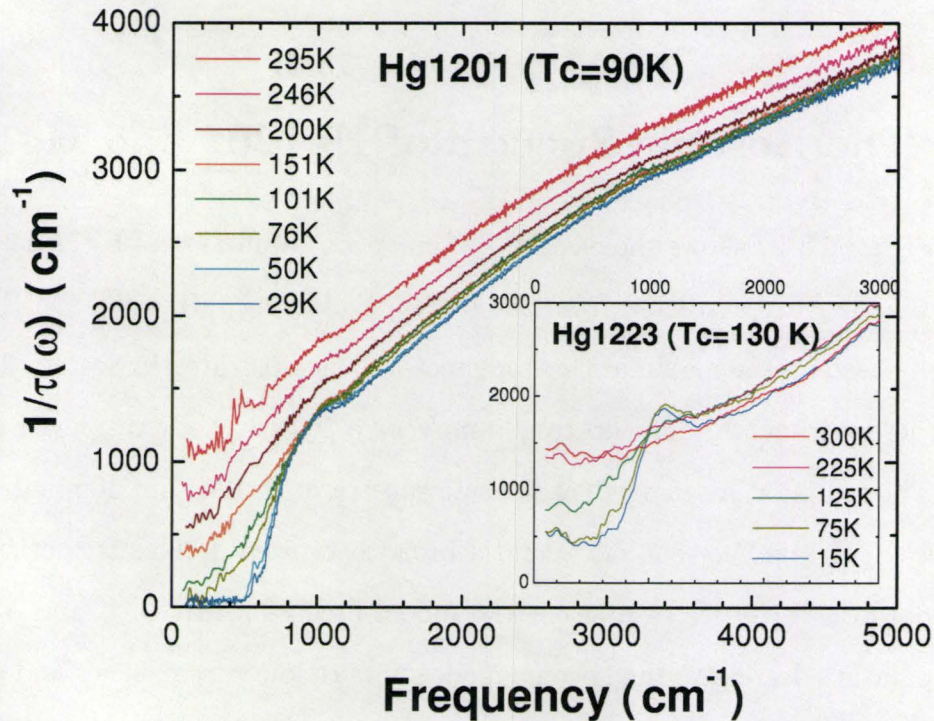


Figure 6.2 The optical scattering rate of Hg1201 at different temperatures. Inset: the optical scattering rate of trilayer Hg1223 ($T_c=130$ K) (McGuire, 2001).

Figure 6.2 shows the spectra of optical scattering rate of Hg1201 based on the extended Drude model, where the plasma frequency $\omega_p \approx 16,120\text{ cm}^{-1}$ and $\epsilon_H \approx 3.30$.

For a comparison, the optical scattering rate spectra of Hg1223 (McGuire, 2001), which has three CuO_2 planes in one unit cell and a higher $T_c=130$ K, are displayed as an inset. As seen in Figure 6.2, there is a sharp onset of scattering around 500 cm^{-1} at the lowest two temperatures of Hg1201. In contrast with this, the onset of scattering of trilayer Hg1223 is around 700 cm^{-1} , higher than that of monolayer Hg1201. Note that, the ratio between the onset frequency of Hg1201 and that of Hg1223, $500 \text{ cm}^{-1}/700 \text{ cm}^{-1}=0.71$, agrees with the ratio between their T_c values, *i.e.* $90 \text{ K}/130 \text{ K}=0.69$.

6.3 The Bosonic Spectra of Hg1201 and Hg1223

Figure 6.3(b) shows the electron-boson spectral function of Hg1201 as a function of temperature extracted from the optical scattering rate using the Eliashberg inversion based on the maximum entropy method, as illustrated in Section 3.3.2. The fits to the experimental data up to 400 meV or $3,200 \text{ cm}^{-1}$ are displayed in Figure 6.3(a). The temperature-dependent bosonic spectra of Hg1201 are dominated by one mode below 100 meV or 800 cm^{-1} and a broad background. This is consistent with the model for $I^2\chi(\Omega)$ we assume for the model fitting of $\text{YBCO}_{6.35}$ and $\text{YBCO}_{6.50}$. As temperature decreases, the bosonic mode shifts to lower frequencies and gets fixed around 56 meV or 448 cm^{-1} in the superconducting states. The bosonic mode position is in agreement with a magnetic mode that was observed to locate around 52 meV in a preliminary neutron study on optimally doped Hg1201 (Zhao et al., 2006). As seen in the inset of Figure 6.3 (b), the mode is fixed around 56 meV at low temperatures and starts to shift towards higher frequencies when $T > 160 \text{ K}$. Meanwhile the amplitude of the mode is reduced rapidly as temperature is increased.

All of the above features of the bosonic spectra of nearly optimally doped

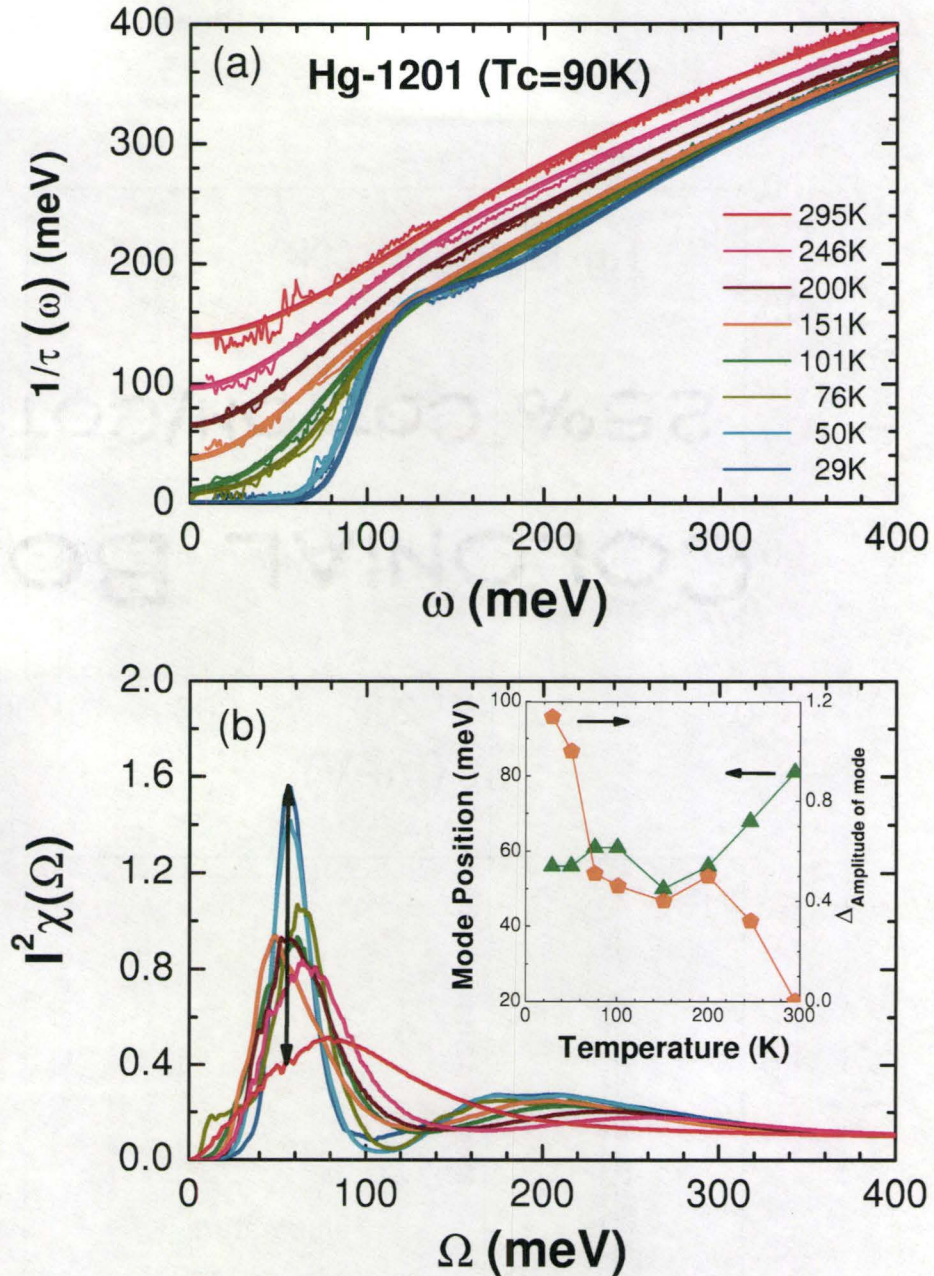


Figure 6.3 (a) The fits to the optical scattering rate of Hg1201 at different temperatures by using the maximum entropy inversion process. (b) The bosonic spectral density of Hg1201 at different temperatures. The arrow shows $\Delta_{\text{amplitude of mode}}$ for the mode located at 56 meV at $T=29$ K, which is the amplitude of the mode relative to the background of room temperature spectrum. Inset shows the variation of mode position and $\Delta_{\text{amplitude of mode}}$ with temperature.

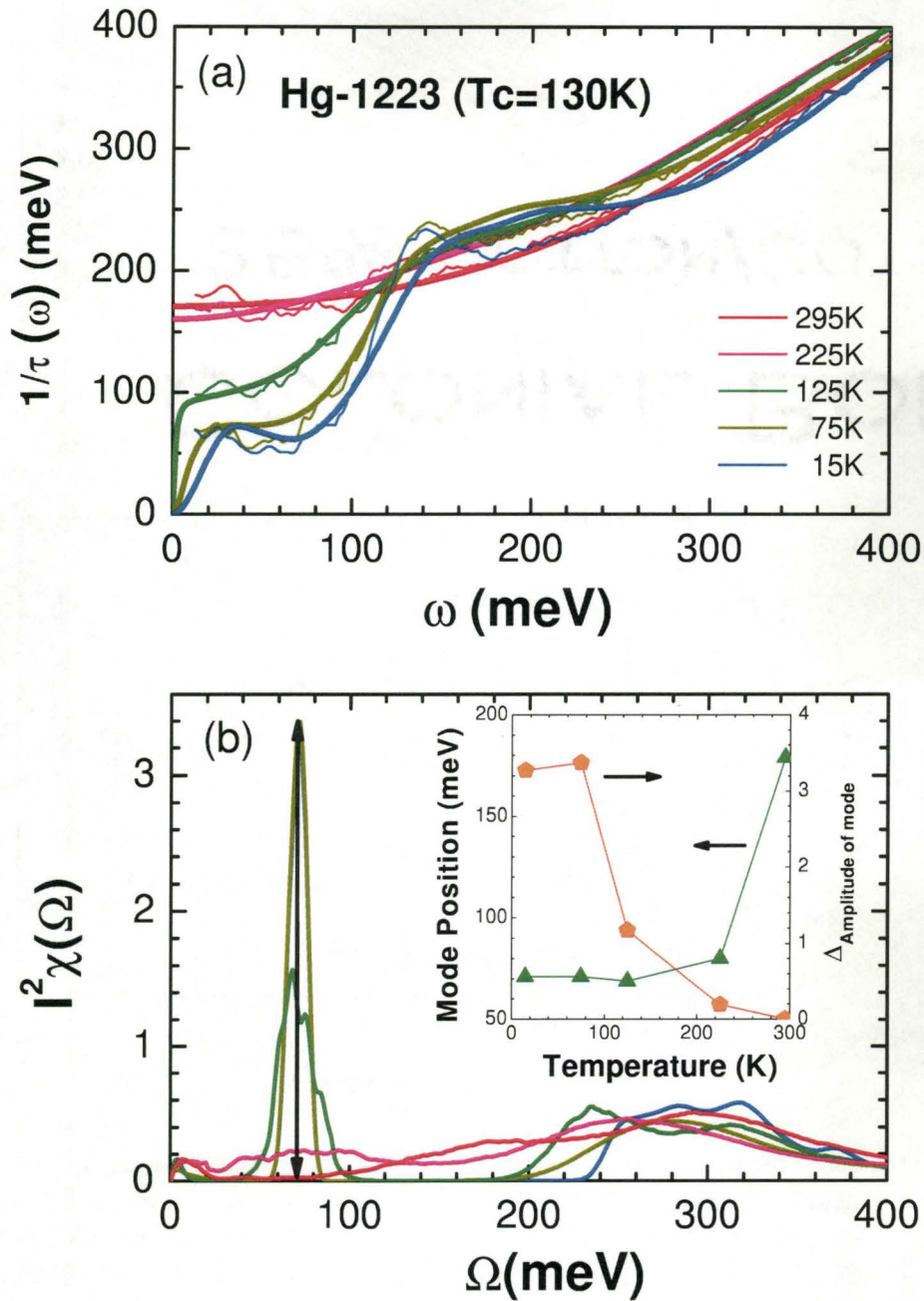


Figure 6.4 (a) The fits to the optical scattering rate of Hg1223 at different temperatures by using the maximum entropy inversion process. (b) The bosonic spectral density of Hg1223 at different temperatures. The arrow shows $\Delta_{\text{amplitude of mode}}$ for the mode located at 72 meV at $T=15\text{ K}$. Inset shows the variation of mode position and $\Delta_{\text{amplitude of mode}}$ with temperature.

monolayer Hg1201 are similar to those of the optimally doped bilayer Bi2212 system (Hwang et al., 2007b). However, in the case of another optimally doped monolayer cuprate system LSCO, there is an additional mode appearing at a lower frequency in the bosonic spectra, observed in both optical (Hwang et al., 2008a) and inelastic neutron studies (Vignolle et al., 2007). Therefore, the appearance of an additional lower-frequency bosonic mode is not a universal feature of the monolayer cuprate superconductors, but an intrinsic property of LSCO and might be responsible for its low $T_c^{max} \approx 30$ K.

For a comparison with the trilayer Hg-based cuprate system, we extract the bosonic spectra of Hg1223 as well from the optical scattering rate spectra measured previously (McGuire et al., 2000), as exhibited in Figure 6.4. The position of the bosonic mode of Hg1223 locates around 72 meV or 576 cm^{-1} , higher than the mode frequency of 56 meV for Hg1201. The ratio of the two mode positions, $56 \text{ meV}/72 \text{ meV}=0.78$, is once again in consistence with the ratio of the T_c values of the two Hg-based cuprates, within uncertainties. The mode frequency is approximately proportional to T_c as $\Omega_{\text{mode}} = A \cdot k_B T_c$ with a coefficient $A : 6 \sim 7$. The blue-shift of mode position and the decay of the mode amplitude with temperature are similar to those of Hg1201.

6.4 Summary

In summary, the bosonic spectrum of the nearly optimally doped monolayer cuprate Hg1201 features one mode located around 56 meV in the superconducting state. This confirms that the two-bosonic-mode feature observed in LSCO is not a common property for the monolayer cuprates, but an intrinsic property of LSCO which has a much lower $T_c^{max} \approx 30$ K. Furthermore compared to the bosonic mode of

optimally doped trilayer Hg1223 that has a higher T_c , the position of bosonic mode is approximately proportional to T_c . In both Hg1201 and Hg1223, the position of the mode shifts to higher frequencies and the amplitude is reduced dramatically as temperature is increased.

Chapter 7

Bosonic Spectra of Zn-Bi2212 and Ni-Bi2212

7.1 Introduction

Chapter 7 deals with the optical studies of the Zn- and Ni- substituted Bi2212 single crystals. Section 7.2 gives the experimental results and section 7.3 elaborates on the comparisons of the bosonic spectra within these two systems as well as with two bare optimally doped Bi2212 systems.

7.2 Sample Preparations

The high-quality single crystals were grown by the traveling-solvent floating-zone method in Dr. Kadowaki's group (Terashima et al., 2006). With a concentration of only 0.2% and 1.0%, Zn (non-magnetic) and Ni (magnetic) atoms are expected to be substituted for the Cu atoms in the CuO_2 planes of optimally doped Bi2212, respectively. The bare Bi2212 without substitution has a T_c around 86 K, while the

substituted samples have T_c 's of 82 K and 79 K for Zn- and Ni- substituted Bi2212, respectively.

The substituted Bi2212 samples are thin plates cleaved from bulk single crystals and have shiny *ab*-plane exposed. The sizes of the plates are $2.0 \times 4.0 \text{ mm}^2$ for Zn-Bi2212, and $1.3 \times 4.5 \text{ mm}^2$ for Ni-Bi2212. They were cut into smaller sizes, $2.0 \times 2.5 \text{ mm}^2$ and $1.3 \times 2.0 \text{ mm}^2$, with a razor blade for optical measurements. The sample pieces are quite thin with a thickness of less than $100 \text{ }\mu\text{m}$. This may cause the samples to break due to possible bends during the temperature-varying experiments. To solve the problem, a small piece of brass, which is about $100 \text{ }\mu\text{m}$ thick, is attached to the back side of each of the samples. The brass pieces have areas a little smaller than the samples to provide enough mechanical support and to avoid any reflection from the brass in the optical measurements.

7.3 Experimental Results

Figure 7.1 shows the reflectance data and the optical conductivity of Zn-Bi2212 and Ni-Bi2212 at seven different temperatures, three of which are in the superconducting states. Again, the shoulder-like feature is present in both reflectance spectra in the superconducting states below 800 cm^{-1} . The optical conductivity spectra feature a growth of the Drude-like peak as T is reduced and, in the superconducting states, an extremely narrow and strong peak around zero frequency accompanied by loss of spectral weight loss just above the peak. These are the common features in the spectra of cuprate superconductors.

As before, within the frame of an extended Drude model, we obtain the imaginary and real parts of optical self-energy, $1/\tau(\omega) = -2\Sigma_2^{op}$ and $-2\Sigma_1^{op}$, for Zn-Bi2212 and Ni-Bi2212, as seen in Figure 7.2. As what we see in Hg1201, a sharp onsets of

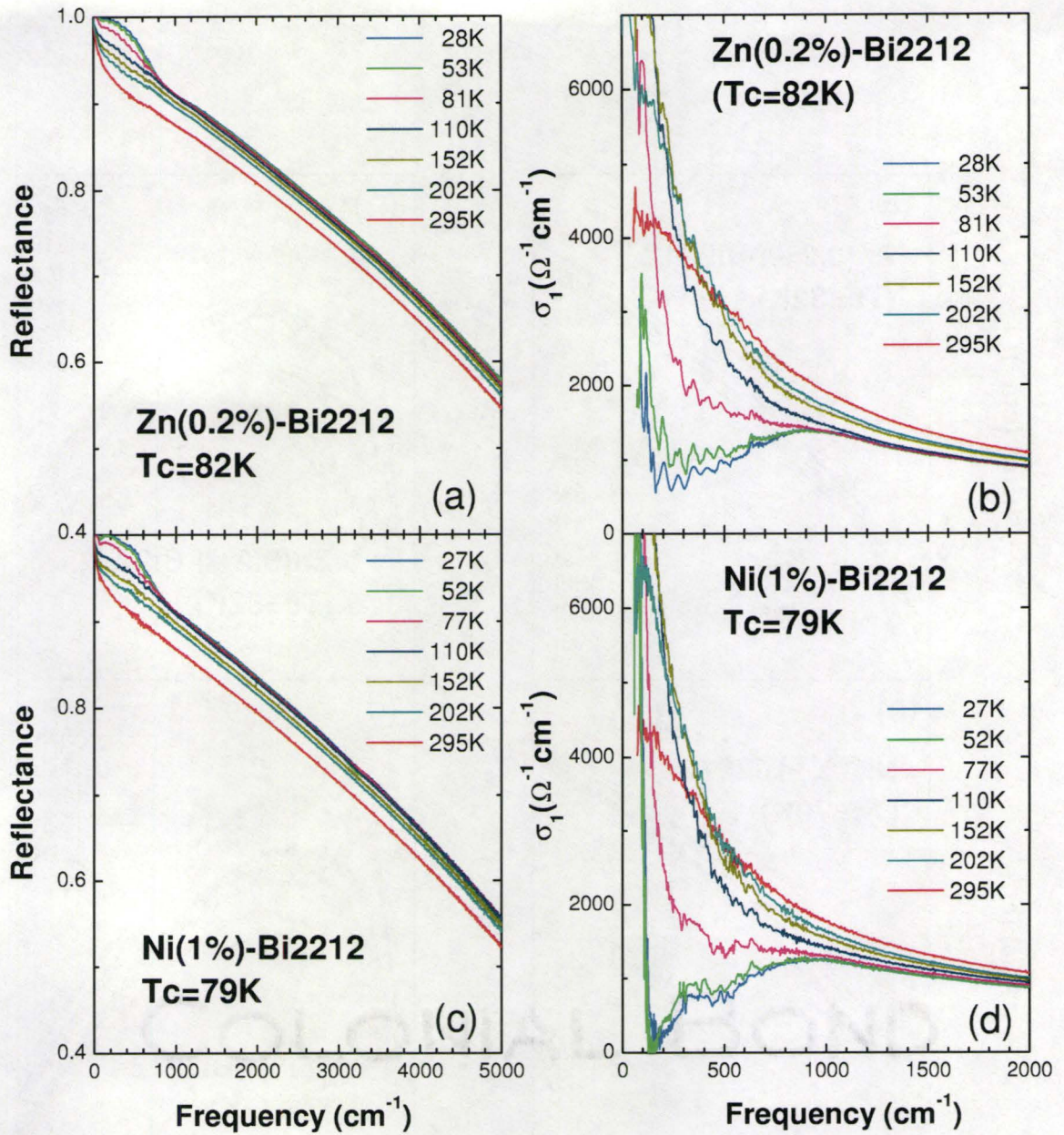


Figure 7.1 The reflectance and optical conductivity spectra at different temperatures for the Zn-substituted Bi2212 sample (a and b) and for the Ni-substituted sample (c and d).

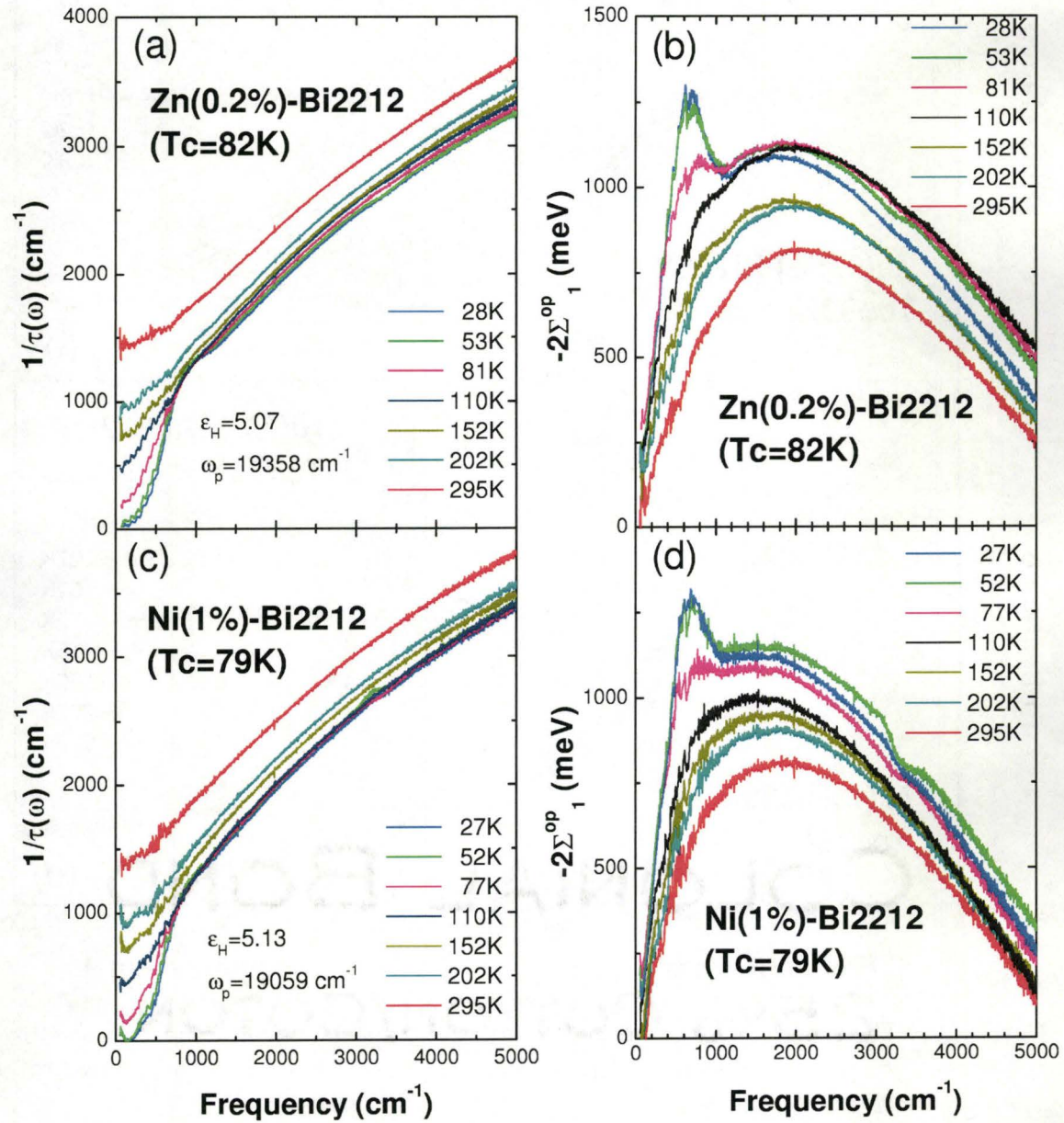


Figure 7.2 The optical scattering rate and the real part of optical self-energy of Zn-Bi2212 (a and b) and of Ni-Bi2212 (c and d).

scattering forms at low frequencies as temperature drops below T_c and the scattering rate increases linearly above $1,000 \text{ cm}^{-1}$ in both Zn-Bi2212 and Ni-2212. In the real part of optical self-energy as shown in Figure 7.2(b) and (d), there are strong peaks below $1,000 \text{ cm}^{-1}$ at the lowest two temperatures.

Although the overall spectra of Zn-Bi2212 and Ni-Bi2212 look quite similar, a tiny difference is noticeable in the real part of optical self-energy around $1,000 \text{ cm}^{-1}$ between these two systems. For Ni-Bi2212, the strong peak located around 700 cm^{-1} does disappear in the normal states; however, for Zn-Bi2212, the peak is still detectable as temperature rises above T_c and even up to 202 K. A comparison of the optical scattering rate between Zn-Bi2212 and Ni-2212 reveals the tiny difference as well, if we look more carefully to the spectra in Figure 7.2(a) and (c). In the normal states of Ni-Bi2212 the $1/\tau(\omega)$ curves are featureless in the region around $1,000 \text{ cm}^{-1}$, while the spectra of Zn-Bi2212 have a hump-like feature at $1,000 \text{ cm}^{-1}$ for $T > T_c$.

7.4 Discussion: the Bosonic Mode

The different behavior of the peak around 700 cm^{-1} in the real part of optical self-energy as a function of temperature between Zn-Bi2212 and Ni-Bi2212 are quantitatively analyzed with a slope-analysis method. First of all, the $-2\Sigma_1^{op}$ spectra between 680 cm^{-1} and $1,300 \text{ cm}^{-1}$ are fitted with polynomial functions as shown in Figure 7.3(a) and (b). The dashed curves represent the least square fits to the data with polynomial functions. The derivatives of the resulting polynomial curves are then calculated and plotted in Figure 7.3(e) and (f). The minimum of each curve, *e.g.* the solid dot, indicates the steepness of the peak in $-2\Sigma_1^{op}$ for each temperature. Around $1,200 \text{ cm}^{-1}$ the curves of derivative of $-2\Sigma_1^{op}$ tend to flatten out and merge for different temperatures, where we assign the value of the open dot as the slope of

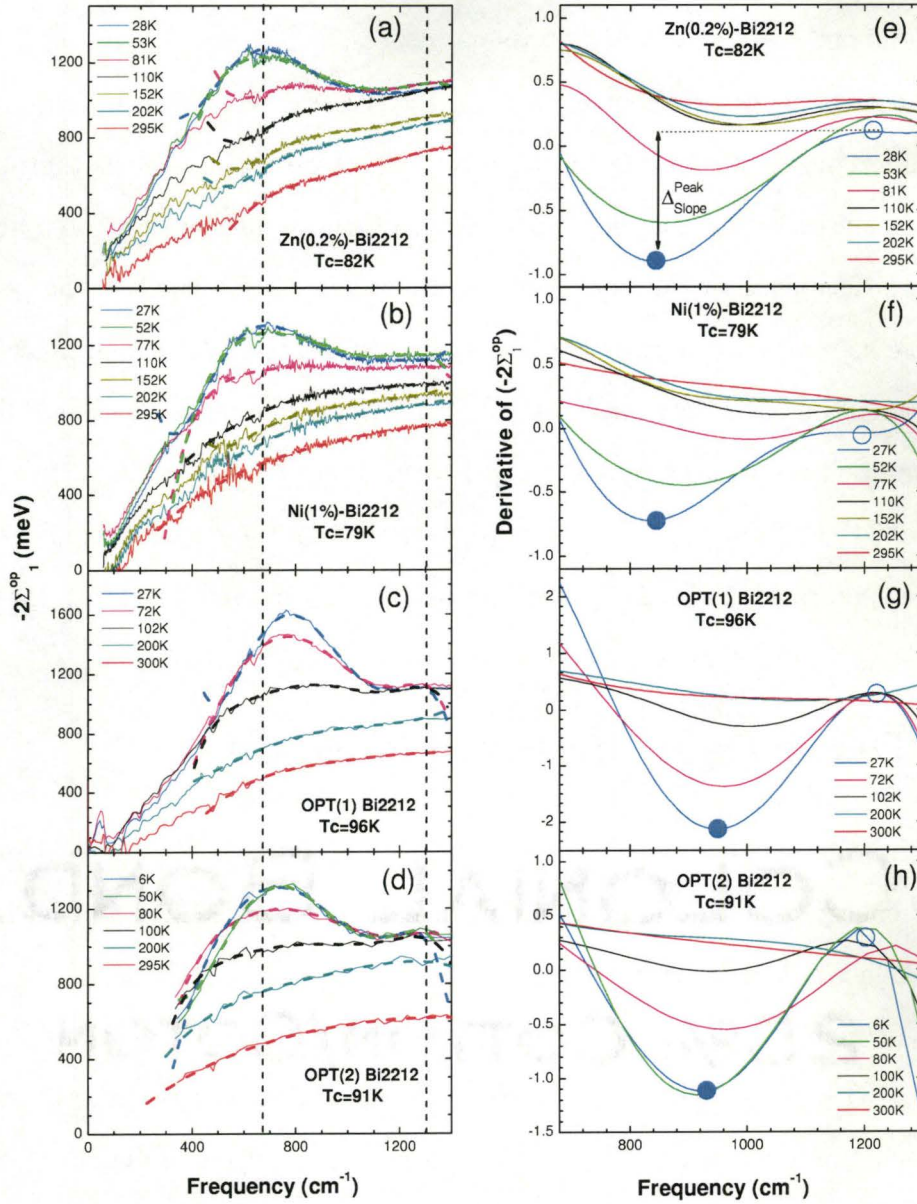


Figure 7.3 (a)-(d) Expanded view of the real part of optical self-energy at low frequencies for Zn-Bi2212, Ni-Bi2212, and another two optimally (OPT) doped bare Bi2212 samples, OPT(1) Bi2212 (Hwang et al., 2007b) and OPT Bi2212 (Tu et al., 2002). Note that, OPT(1) Bi2212 is slightly yttrium doped and thus has a higher T_c than OPT Bi2212. Dotted curves are polynomial fits to data. (e)-(h) The derivative of $-2\Sigma_1^{op}$ with respect to frequency for Zn-Bi2212, Ni-Bi2212, OPT(1) Bi2212, and OPT(2) Bi2212.

background above the peak. We define $\Delta_{Slope}^{Peak} \equiv \frac{\partial(-2\Sigma_1^{op})}{\partial\omega}|_{closed\ dot} - \frac{\partial(-2\Sigma_1^{op})}{\partial\omega}|_{open\ dot}$, which can be a measure of the steepness of the peak of $-2\Sigma_1^{op}$ relative to the background. The slope-analysis method is also performed to the data of another two bare Bi2212 samples, OPT(1) Bi2212 and OPT(2) Bi2212, that were measured previously by others (Hwang et al., 2007b, Tu et al., 2002), as shown in Figure 7.3(c) and (d).

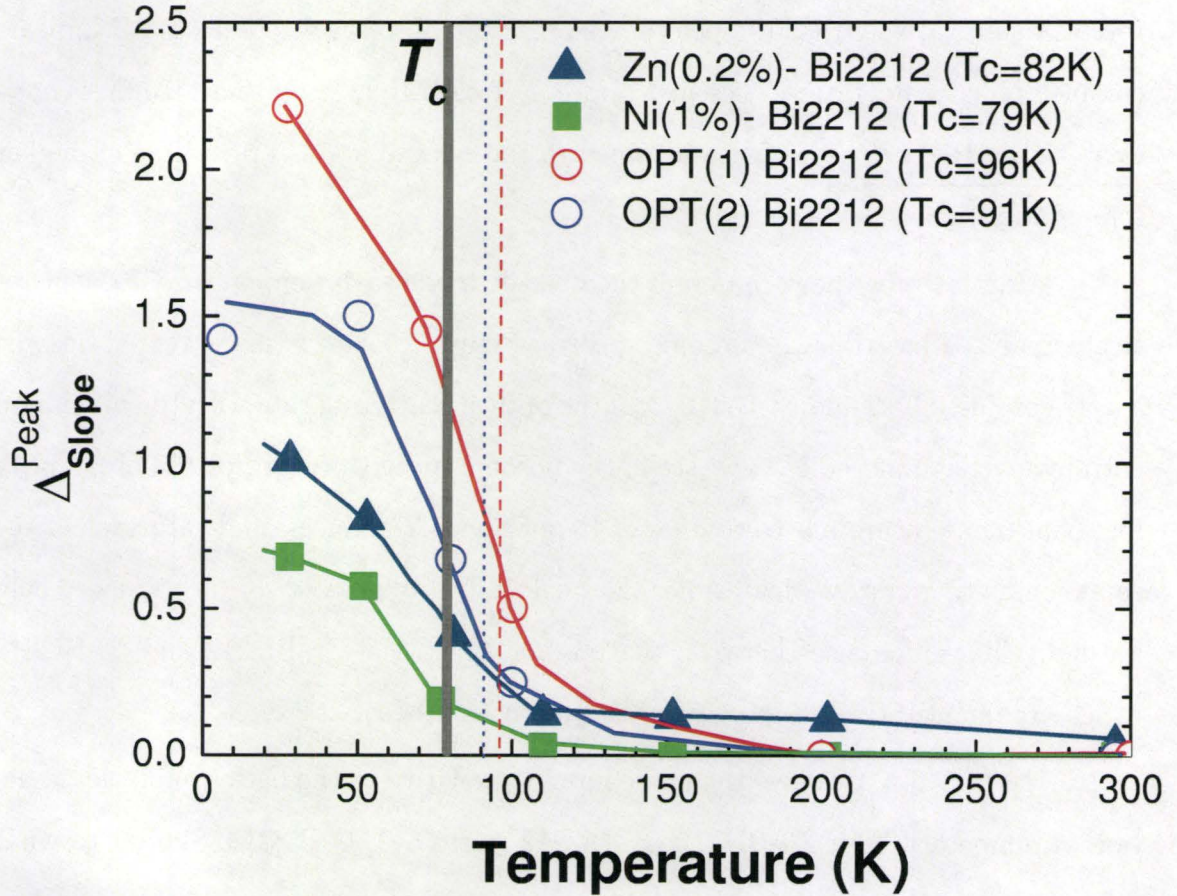


Figure 7.4 The slope of the right side of the peak in $-2\Sigma_1^{op}$ relative to the background, as a function of temperature for Zn-Bi2212, Ni-Bi2212, OPT(1) Bi2212, and OPT(2) Bi2212.

In Figure 7.4, we plot Δ_{Slope}^{Peak} as a function of temperature for Zn-Bi2212, Ni-Bi2212, OPT(1) Bi2212, and OPT(2) Bi2212. In the superconducting states, the small amount of substitution of Zn and Ni suppress the steepness of peak signifi-

cantly, compared to the bare Bi2212 samples. For all the samples, $\Delta_{\text{Slope}}^{\text{Peak}}$ decreases drastically around $T = T_c$ and becomes zero at $T > T_c$, except for Zn-Bi2212, the steepness of peak saturates at a non-zero value even up to 200 K. The slope-analysis reveals quantitatively that the peak in the real part of optical self-energy disappears completely as temperature rises just above T_c for Ni-Bi2212 and bare Bi2212; however, for Zn-Bi2212 the peak is sustained in the normal states up to a much higher temperature.

Alternatively, the variation of the bosonic mode with temperature is quantitatively analyzed based on the bosonic spectra. Figure 7.5 shows the extracted bosonic spectra of Zn-Bi2212 and Ni-Bi212 from the optical scattering rate with the maximum entropy inversion method. As we see in the bosonic spectra of Hg1201, the broad peak for room temperature moves to a lower frequency as T reduces, and saturates in the superconducting states. Meanwhile, the peak intensity grows as T decreases. There are noticeable differences between the bosonic spectra of Zn-Bi2212 and Ni-Bi2212 which are quantitatively summarized in Figure 7.6(a)-(d).

Figure 7.6(a) displays the mode intensity relative to the background as a function of temperature for Zn-Bi2212, Ni-Bi2212, and OPT(1) Bi2212. Similar to what we see in the slope-analysis, the intensity of the mode is substantially reduced in the substituted Bi2212 samples for the superconducting states. However for the normal states, unfortunately, there are no significant effects due to atom substitutions. As seen in Figure 7.6(b), the bosonic mode of Zn-Bi2212 is sharper than that of Ni-Bi2212 for both superconducting and normal states where the mode exists. The change of mode position with temperature, as shown in Figure 7.6(c), is consistent with the slope-analysis conclusion of the normal state. For both Ni-Bi2212 and bare OPT Bi2212, the bosonic mode starts to shift to higher frequencies around $T = T_c$, while for Zn-Bi2212, the mode position remains a constant up into the normal states

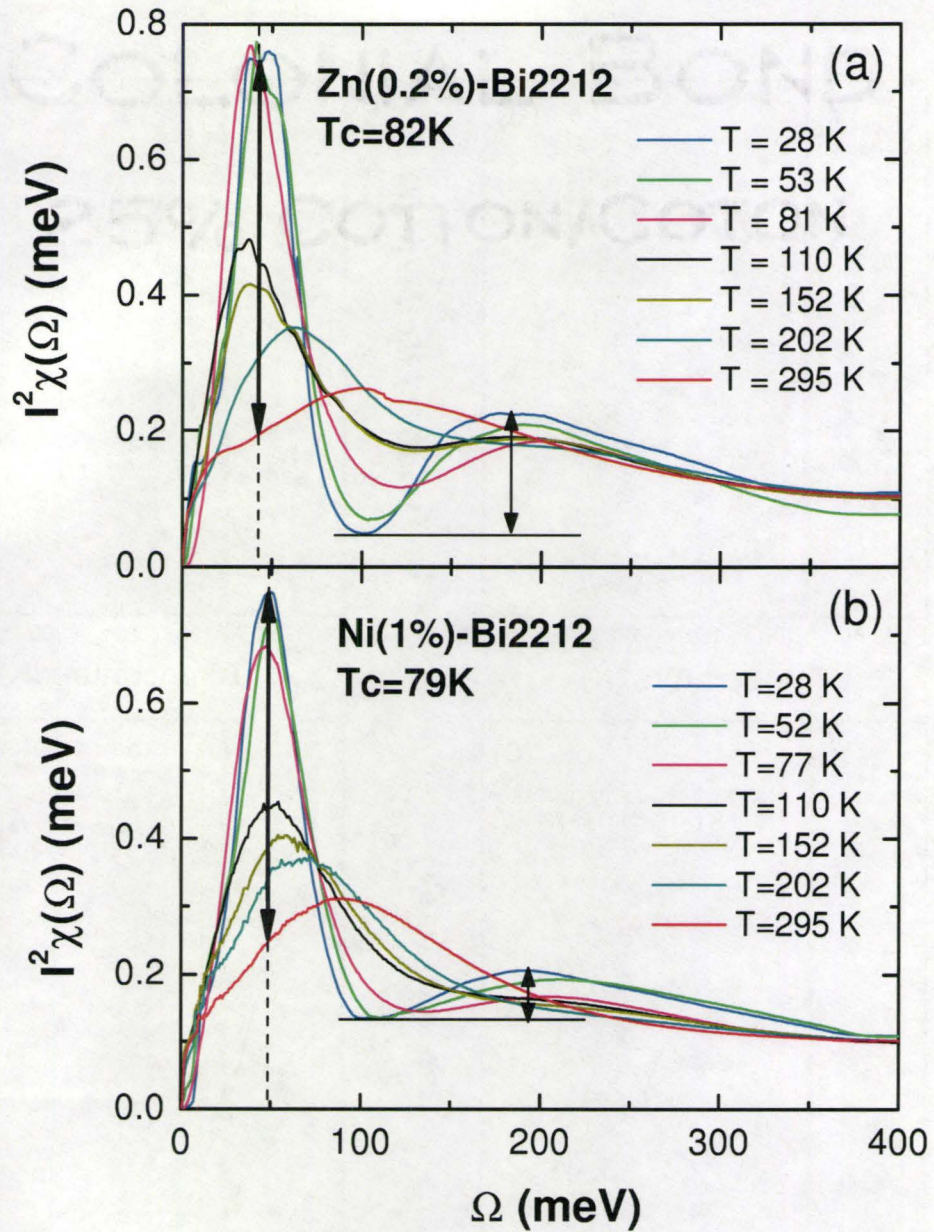


Figure 7.5 The extracted bosonic spectra of Zn-Bi2212 (a) and Ni-Bi2212 (b). The arrows show the amplitude of the mode around 50 meV and the gap around 100 meV at 28 K.

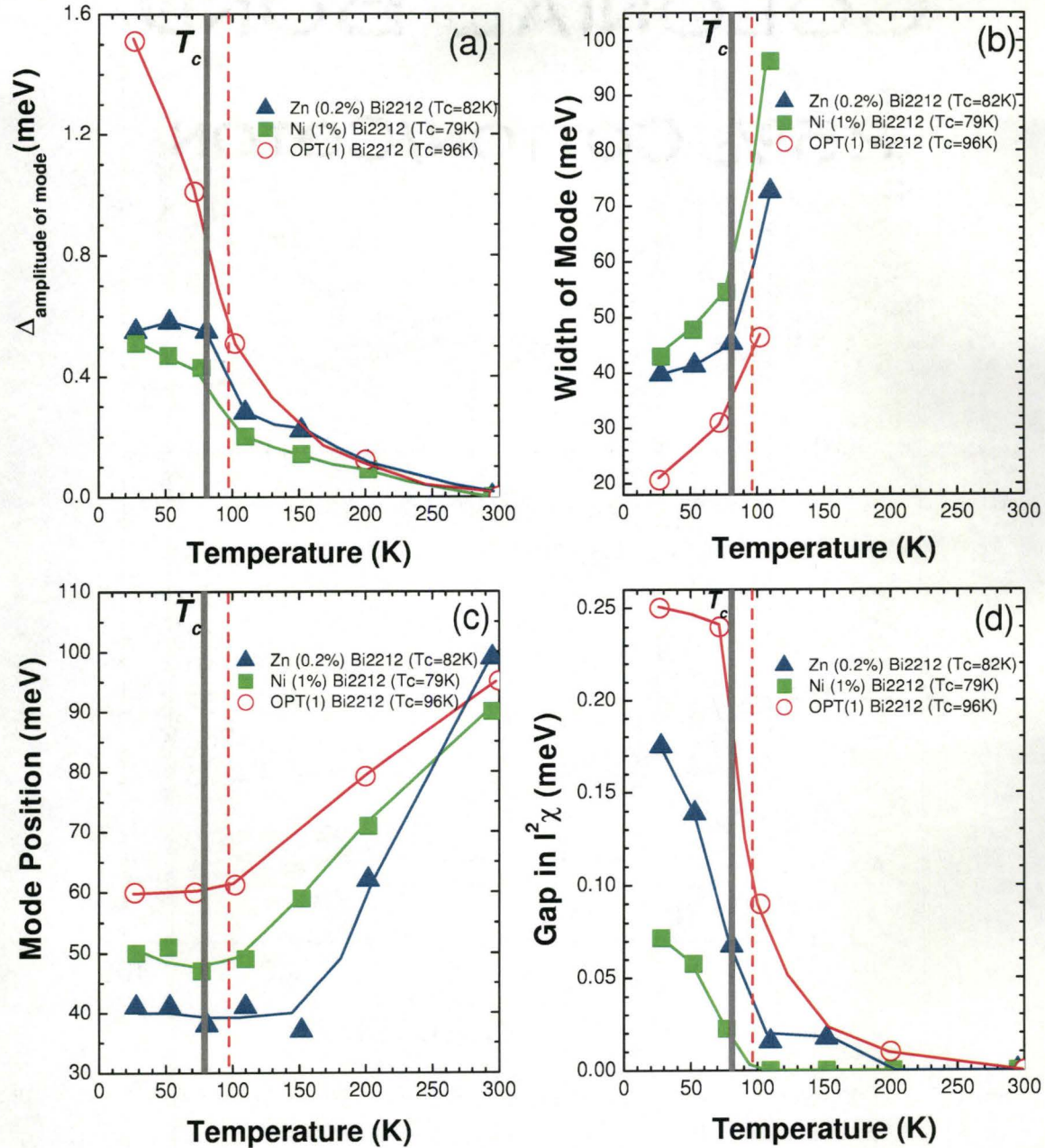


Figure 7.6 (a) The amplitude of the bosonic mode relative to the background of room-temperature spectra, as denoted by the first arrow in Figure 7.5, for different temperatures. (b) The width of the bosonic mode as a function of temperature. (c) The shifts of mode position with temperature. (d) The variation of the gap size, as indicated by the second arrow in Figure 7.5, with temperatures.

and then moves in a faster manner to higher frequencies. We define the size of the gap in the bosonic spectra as the difference between the gap minimum and the background maximum, as represented by the arrow in Figure 7.5. The variation of the gap size with temperature are displayed in Figure 7.6(d). The gap disappears in the normal states of Ni-Bi2212, whereas Zn-Bi2212 has a gap maintained for $T > T_c$.

The Zn- and Ni- substituted Bi2212 samples from the same source were studied by ARPES as well (Terashima et al., 2006), where the results were also compared with those of inelastic neutron scattering (INS) studies on Zn- and Ni- substituted YBCO samples as seen in Figure 7.7. In ARPES, the real part of the electron self-energy at a maximum, namely $\text{Re}\Sigma(\omega)^{max}$, of bare Bi2212 is substantially suppressed by a substitution of Zn or Ni for Cu when $T < T_c$. Meantime, in the normal states, only the Zn-Bi2212 sample has a residue amplitude of $\text{Re}\Sigma(\omega)^{max}$ up to $T > 150$ K, whereas $\text{Re}\Sigma(\omega)^{max}$ of Ni-Bi2212 and bare Bi2212 are nearly zero at temperatures above T_c . Similar behaviors are observed in the spin susceptibility χ'' data of bare, Zn-substituted, and Ni-substituted YBCO samples measured with neutrons as shown in Figure 7.7. Note that our optical results are consistent with those of ARPES and neutron studies in terms of the different substitution effects of non-magnetic and magnetic atoms for Cu, based on the analysis shown in Figure 7.4 and 7.6.

It should be mentioned that the substitution effects are anisotropic over the Brillouin zone and are more pronounced along the anti-nodal direction $(\pi, 0)$ according to ARPES, a momentum-sensitive study (Terashima et al., 2006). However in optical spectroscopy, the momentum transfer is almost zero and what optics detects are averaged effects over the Brillouin zone. Therefore, we observe less pronounced substitution effects shown in Figure 7.4 and 7.6 than those in ARPES shown in Figure 7.7.

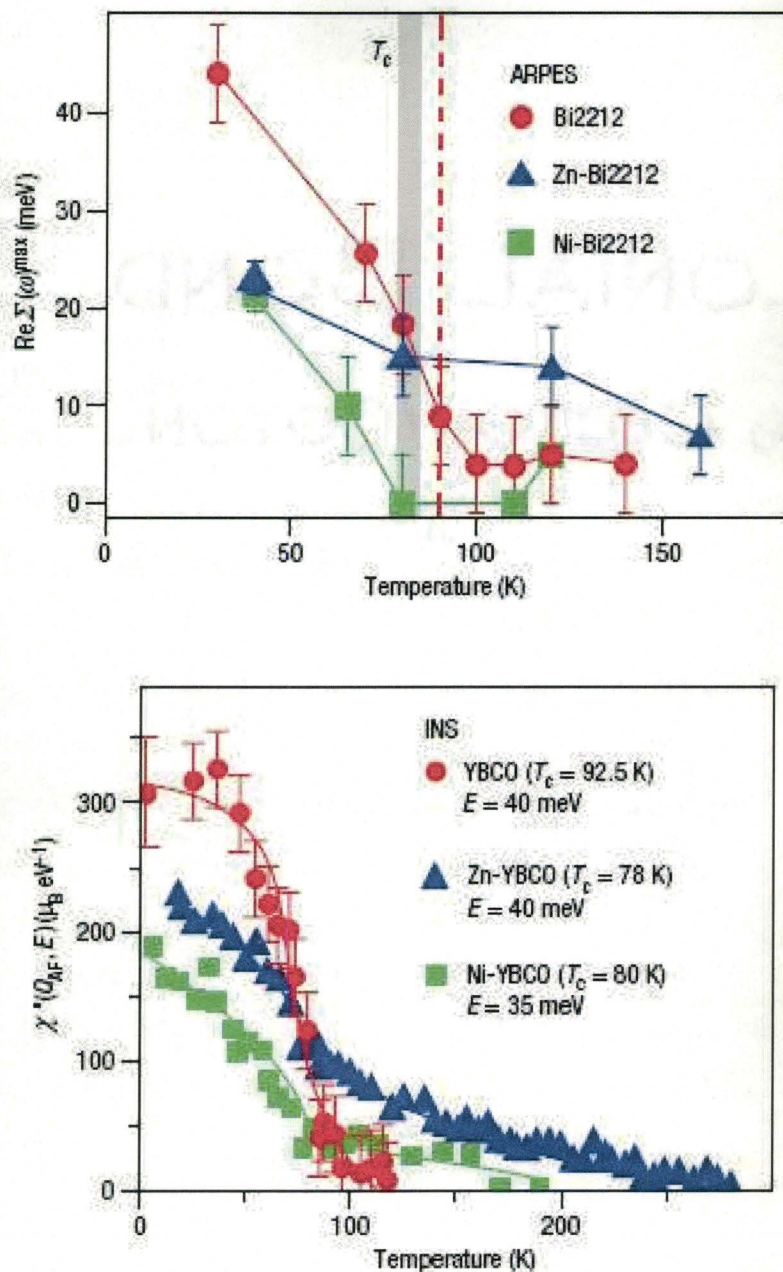


Figure 7.7 The real part of the electron self-energy at a maximum $\text{Re}\Sigma(\omega)^{\text{max}}$ as a function of temperature for bare Bi2212, Zn-Bi2212, and Ni-Bi2212 in an ARPES study. And the spin susceptibility χ'' of bare YBCO, Zn-YBCO, and Ni-YBCO in an inelastic neutron scattering study. (Terashima et al., 2006)

7.5 Summary

To summarize, optical studies on the Zn- and Ni- substituted optimally doped Bi2212 samples and comparisons with bare Bi2212 reveal that there are substitution effects in the temperature-dependent optical self-energy and the bosonic spectra. For the superconducting states, substitutions of Zn and Ni for Cu significantly suppress the bosonic mode intensity compared to bare Bi2212. As temperatures rise above T_c , the variations of the mode with temperature in Ni-Bi2212 and bare Bi2212 follow the same trend, whereas Zn-Bi2212 shows a different behavior. These optical results are consistent with those of an ARPES study on the Zn- and Ni- substituted Bi2212 samples from the same source and also the neutron studies on the Zn- and Ni- substituted YBCO systems.

Chapter 8

Conclusions

In conclusion, this thesis focuses on optical spectroscopy studies on two low-dimensional systems, SRR metamaterials and high- T_c cuprate superconductors. Although they exhibit completely different properties, they are both two-dimensional or quasi-two-dimensional systems.

Based on the transmission measurements and the numerical analysis of SRR metamaterials, we conclude that a double-ring SRR array could have a left-handed behavior or a negative index of refraction without any additional continuous metallic wires, as opposed to the conventional designs of SRR left-handed metamaterials. We also propose a new left-handed SRR metamaterial, which is composed of two single-ring SRRs in each unit cell. In our designs, we make use of not only the magnetic but also the electric resonance of the SRR structure and carefully tune the resonance frequencies to achieve a left-handed behavior within certain frequency region.

The reflectance measurements and related theoretical calculations on the high- T_c cuprate superconductors, reveal that the bosonic mode resolved from the optical data are consistent with the magnetic mode observed in the inelastic neutron scattering studies, in terms of mode energy, temperature dependence as well as non-magnetic

and magnetic atom substitution effects. Moreover, comparisons of the bosonic spectra between highly under-doped YBCO_{6.35} and under-doped ortho-II YBCO_{6.50}, optimally doped monolayer Hg1201 and trilayer Hg1223, Zn-substituted Bi2212 and Ni-substituted Bi2212, demonstrate the variation of the bosonic mode as functions of doping, T_c as well as non-magnetic and magnetic substitutions. In the YBCO systems, the mode located around 30 meV in under-doped ortho-II YBCO_{6.50} disappears completely in the highly under-doped YBCO_{6.35}; in optimally doped Hg-based cuprates, the mode energy follows T_c in an approximately linear manner; in the optimally doped Bi2212 systems, a substitution of Zn (non-magnetic) atoms for Cu affects the bosonic spectra in a different way from the Ni (magnetic)-substitution in the normal states. Meanwhile, in Figure 8.1, we summarize the center frequency of the bosonic mode at the lowest temperature Ω_{mode} versus the transition temperature T_c for different high- T_c cuprate systems, including the materials that are studied in this thesis as well as samples studied earlier by us (Hwang et al., 2006a, 2007b, 2008a) and by other groups (Schachinger and Carbotte, 2000, Schachinger et al., 2006, Schachinger, 2008). As shown by the dashed line of a linear fit to the data points, we conclude a linear relation between Ω_{mode} and T_c as $\Omega_{\text{mode}} \sim 7.1k_B T_c$, where k_B is the Boltzmann constant. We notice that a similar relation between the magnetic resonance of spin fluctuations E_{res} and T_c was deduced as $E_{\text{res}} \sim 5.4k_B T_c$, based on the inelastic neutron scattering studies (He et al., 2001). Our results are in excellent agreement with the neutron studies in terms of the linear behavior of the mode or resonance as a function of T_c . Since optics is not a momentum-sensitive technique, the mode we observed is an averaged effect over the first Brillouin zone, as opposed to the magnetic resonance with wave vector (π, π) observed in neutron studies. This causes small energy shifts of the optical mode compared to the neutron mode, which results in the difference in the slopes of the linear behaviors. In summary, we conclude that the electron-boson

spectral function extracted from the optical data on high- T_c superconductors are more relevant to the interactions between electron and the spin fluctuations, as opposed to the electron-phonon interactions in the conventional superconductors.

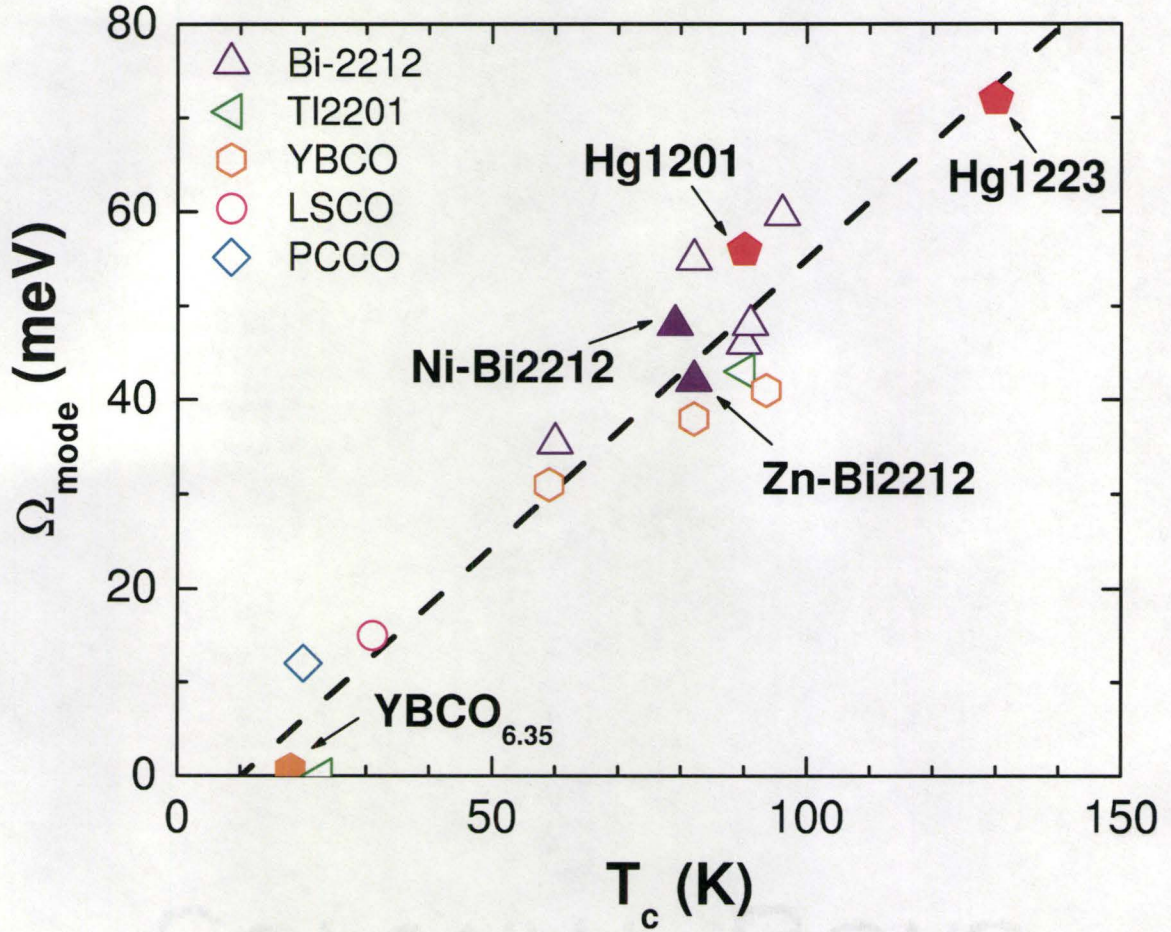


Figure 8.1 A summary of the center frequency of the bosonic mode (Ω_{mode}) versus the HTSC transition temperature (T_c), based on the optical studies. Closed symbols represent the materials studied in this thesis, and open ones are for the samples studied earlier by us (Hwang et al., 2006a, 2007b, 2008a) and by other groups (Schachinger and Carbotte, 2000, Schachinger et al., 2006, Schachinger, 2008). The dashed line shows a linear fit which denotes $\Omega_{\text{mode}} \sim 7.1 k_B T_c$.

References

Ahn, C. H., Triscone, J.-M., and Mannhart, J. (2003). *Nature*, 424, 1015.

Allen, P. B. (1971). *Phys. Rev. B*, 3, 305.

Bardeen, J., Cooper, L. N., and Schrieffer, J. R. (1957). *Phys. Rev.*, 108, 1175.

Basov, D. N. and Timusk, T. (2005). *Rev. Mod. Phys.*, 77, 721.

Bednorz, J. G. and Müller, K. A. (1968). *Z. Phys. B*, 64, 189.

Born, M. and Wolf, E. (1999). *Principles of optics: electromagnetic theory of propagation, interference and diffraction of light*. Cambridge University Press, Cambridge, 7th expanded edition.

Broun, D. (2008). *Private Communication*.

Burns, G., Dacol, F., Freitas, P., Plaskett, T., and König, W. (1987). *Solid State Commun.*, 64, 471.

Carbotte, J. P. (1990). *Rev. Mod. Phys.*, 62, 1027.

Carbotte, J. P. and Schachinger, E. (2006). *Ann. Phys.*, 15, 585.

Chen, H., Ran, L., Huangfu, J., Zhang, X., Chen, K., Grzegorzczak, T. M., and Kong, J. A. (2004). *Phys. Rev. E*, 70, 057605.

Colson, D. (2008). *private communication*.

Dai, P., Mook, H. A., Hayden, S. M., Aeppli, G., Perring, T. G., Hunt, R. D., and Dogan, F. (1999). *Science*, 284, 1344.

Enkrich, C., Wegener, M., Linden, S., Burger, S., Zschiedrich, L., Schmidt, F., Zhou, J. F., Koschny, T., and Soukoulis, C. M. (2005). *Phys. Rev. Lett.*, 95, 203901.

Farnworth, B. and Timusk, T. (1976). *Phys. Rev. B*, 14, 5119.

Fong, H. F., B. Keimer, Anderson, P. W., Reznik, D., Dogan, F., and Aksay, I. A. (1995). *Phys. Rev. Lett.*, 75, 316.

Fong, H. F., Bourges, P., Sidis, Y., Regnault, L. P., Ivanov, A., Gu, G. D., Koshizuka, N., and Keimer, B. (1999). *Nature*, 398, 588.

Fowles, G. R. (1989). *Introduction to Modern Optics*. Dover Publications Inc., New York, 2nd edition.

Griffiths, P. R. and de Haseth, J. A. (2007). *Fourier Transform Infrared Spectrometry*. John Wiley and Sons Inc., New York, 2nd edition.

He, H., Bourges, P., Sidis, Y., Ulrich, C., Regnault, L. P., Pailhès, S., Berzigiarova, N. S., Kolesnikov, N. N., and Keimer, B. (2002). *Science*, 295, 1045.

He, H., Sidis, Y., Bourges, P., Gu, G. D., Ivanov, A., Koshizuka, N., Liang, B., Lin, C. T., Regnault, L. P., Schoenherr, E., and Keimer, B. (2001). *Phys. Rev. Lett.*, 86, 1610.

Homes, C. C., Reedyk, M. A., Crandles, D. A., and Timusk, T. (1993). *Appl. Opt.*, 32, 2976.

- Honma, T. and Hor, P. H. (2006). *Supercond. Sci. Technol.*, 19, 907.
- Hüfner, S., Hossain, M. A., Damascelli, A., and Sawatzky, G. A. (2008). *Rep. Prog. Phys.*, 71, 062501.
- Hwang, J., Schachinger, E., Carbotte, J. P., Gao, F., Tanner, D. B., and Timusk, T. (2008a). *Phys. Rev. Lett.*, 100, 137005.
- Hwang, J., Timusk, T., and Gu, G. D. (2007a). *J. Phys.:Condens. Matter*, 19, 125208.
- Hwang, J., Timusk, T., Schachinger, E., and Carbotte, J. P. (2007b). *Phys. Rev. B*, 75, 144508.
- Hwang, J., Yang, J., Carbotte, J. P., and Timusk, T. (2008b). *Accepted for publication in J. Phys.: Condens. Matter*.
- Hwang, J., Yang, J., Timusk, T., Sharapov, S. G., Carbotte, J. P., Bonn, D. A., Liang, R., and Hardy, W. N. (2006a). *Phys. Rev. B*, 73, 014508.
- Hwang, J., Yang, J., Timusk, T., Sharapov, S. G., Carbotte, J. P., Bonn, D. A., Liang, R., and Hardy, W. N. (2006b). *Phys. Rev. B*, 73, 014508.
- Jaynes, E. T. (1957). *Phys. Rev.*, 106, 620.
- Kittel, C. (1976). *Introduction to Solid State Physics*. John Wiley and Sons Inc., New York, 5th edition.
- Koschny, T., Kafesaki, M., Economou, E. N., and Soukoulis, C. M. (2004). *Phys. Rev. Lett.*, 93, 107402.
- Koschny, T., Markoš, P., Smith, D. R., and Soukoulis, C. M. (2003). *Phys. Rev. E*, 68, 065602(R):

- Liang, R., Bonn, D. A., Hardy, W. N., Wynn, J. C., Moler, K. A., Lu, L., Larochelle, S., Zhou, L., Greven, M., Lurio, L., and Mochrie, S. G. J. (2002). *Physica C*, 383, 1–7.
- Linden, S., Enkrich, C., Wegener, M., Zhou, J., Koschny, T., and Soukoulis, C. M. (2004). *Science*, 306, 1351–1353.
- McGuire, J. (2001). *Infrared Properties of Three Low-Dimensional Materials*. Ph.D. thesis, Hamilton, Canada.
- McGuire, J. J., Windt, M., Startseva, T., Timusk, T., Colson, D., and Viallet-Guillen, V. (2000). *Phys. Rev. B*, 62, 8711.
- McMillan, W. L. and Rowell, J. M. (1969). *Superconductivity*, volume 1. Marcel Dekker, New York.
- Mook, H. A., Dai, P., Hayden, S. M., Aeppli, G., Perring, T. G., and Dogan, F. (1998). *Nature*, 395, 580.
- Mook, H. A., Yethiraj, M., Aeppli, G., Mason, T. E., and Armstrong, T. (1993). *Phys. Rev. Lett.*, 70, 3490.
- Onnes, H. K. (1911). *Commun. Phys. Lab. Univ. Leiden*, 12, 120.
- Padilla, W. J., Taylor, A. J., Highstrete, C., Lee, M., and Averitt, R. D. (2006). *Phys. Rev. Lett.*, 96, 107401.
- Pendry, J. B., Holden, A. J., Robbins, D. J., and Stewart, W. J. (1999). *IEEE Trans. Microwave Theory Tech.*, 47, 2075–2084.
- Rockstuhl, C., Zentgraf, T., Guo, H., Liu, N., Etrich, C., Loa, I., Syassen, K., Kuhl, J., Lederer, F., and Giessen, H. (2006). *Appl. Phys. B*, 84, 219–227.

- Romberg, H., Nücker, N., Fink, J., Wolf, T., Xi, X. X., Koch, B., Geserich, H. P., Dürbler, M., Assmus, W., and Gegenheimer, B. (1990). *Z. Phys. B: Condens Matter*, 78, 367.
- Schachinger, E. (2008). *Preprint*.
- Schachinger, E. and Carbotte, J. P. (2000). *Phys. Rev. B*, 62, 9054.
- Schachinger, E., Neuber, D., and Carbotte, J. P. (2006). *Phys. Rev. B*, 73, 184507.
- Schilling, A., Cantoni, M., Guo, J. D., and Ott, H. R. (1993). *Nature*, 363, 56.
- Schurig, D., Mock, J. J., and Smith, D. R. (2006). *Appl. Phys. Lett.*, 88, 041109.
- Sharapov, S. G. and Carbotte, J. P. (2005). *Phys. Rev. B*, 72, 134506.
- Shelby, R. A., Smith, D. R., and Schultz, S. (2001). *Science*, 292, 77–79.
- Shulga, S. V., Dolgov, O. V., and Maksimov, E. G. (1991). *Physica C*, 178, 266.
- Sidis, Y., Bourges, P., Fong, H. F., Keimer, B., Regnault, L. P., Bossy, J., Ivanov, A., Hennion, B., Gautier-Picard, P., Collin, G., Millius, D. L., and Akasay, I. A. (2000). *Phys. Rev. Lett.*, 84, 5900.
- Smith, D. R., Padilla, W. J., Vier, D. C., Nemat-Nasser, S. C., and Schultz, S. (2000). *Phys. Rev. Lett.*, 84, 4184–4187.
- Smith, D. R., Schultz, S., Markoš, P., and Soukoulis, C. M. (2002). *Phys. Rev. B*, 65, 195104.
- Smith, D. R., Vier, D. C., Koschny, T., and Soukoulis, C. M. (2005). *Phys. Rev. E*, 71, 036617.

Soukoulis, C. M., Kafesaki, M., and Economou, E. N. (2006). *Adv. Mater. (Weinheim, Ger.)*, 18, 1941.

Stock, C., Buyers, W. J. L., Cowley, R. A., Clegg, P. S., Coldea, R., Frost, C. D., Liang, R., Peets, D., Bonn, D., Hardy, W. N., and Birgeneau, R. J. (2005). *Phys. Rev. B*, 71, 024522.

Stock, C., Buyers, W. J. L., Yamani, Z., Broholm, C. L., Chung, J. H., Tun, Z., Liang, R., Bonn, D. A., Hardy, W. N., and Birgeneau, R. J. (2006). *Phys. Rev. B*, 73, 100504(R).

Stock, C., Buyers, W. J. L., Yamani, Z., Tun, Z., Birgeneau, R. J., Liang, R., Bonn, D., and Hardy, W. N. (2008). *Phys. Rev. B*, 77, 014513.

Tajima, S., Ido, T., Ishibashi, S., Itoh, T., Eisaki, H., Mizuo, Y., Arima, T., Takagi, H., and Uchida, S. (1991). *Phys. Rev. B*, 43, 10496.

Terasaki, I., Tajima, S., Eisaki, H., Takagi, H., Uchinokura, K., and Uchida, S. (1990). *Phys. Rev. B*, 41, 865.

Terashima, K., Matsui, H., Hashimoto, D., Sato, T., Takahashi, T., Ding, H., Yamamoto, T., and Kadowaki, K. (2006). *Nature Physics*, 2, 27.

Tu, J. J., Homes, C. C., Gu, G. D., Basov, D. N., and Strongin, M. (2002). *Phys. Rev. B*, 66, 144514.

Veal, B. W., Paulikas, A. P., You, H., Shi, H., Fang, Y., and Downey, J. W. (1990). *Phys. Rev. B*, 42, 6305.

Veselago, V. G. (1968). *Sov. Phys. Uspekhi*, 10, 509.

- Vignolle, B., Hayden, S. M., McMorrow, D. F., Rønnow, H. M., Lake, B., Frost, C. D., and Perring, T. G. (2007). *Nature Physics*, 3, 163.
- Yang, J. (2005). *The Doping and Temperature Dependence of Optical Properties of $Nd_{1-x}TiO_3$* . M. Sc. thesis, Hamilton, Canada.
- Yang, J., Hwang, J., and Timusk, T. (2008). *Phys. Rev. B*, 77, 205114.
- Zhao, X., Yu, G., Cho, Y.-C., Chabot-Couture, G., Barišić, N., Bourges, P., Kaneko, N., Li, Y., Lu, L., Motoyama, E. M., Vajk, O. P., and Greven, M. (2006). *Adv. Mater.*, 18, 3243.
- Zhou, J., Koschny, T., Kafesaki, M., Economou, E. N., Pendry, J. B., and Soukoulis, C. M. (2005). *Phys. Rev. Lett.*, 95, 223902.

Appendix A

Matlab programs

```
% Calculation of the optical scattering rate (TAU) by using
% Sharapov's formula shown in Equation (3.23) in Chapter 3.
% Calculation of real part of optical self-energy
% -2*Re(Sigma_1)--RSF is added.
% T: temperature; A: Area of peak; Wpk: Peak frequency; d: Peak width;
% B, C1, C2: parameters for the step function of background;
% Delta: the size of pseudogap.
% PK: peak; BG: background;
```

```
function tau_model
```

```
T=30;A=255;Wpk=0;d=25;A2=0;Wpk2=515;d2=270;B=1.3;C1=380;C2=660;
pref=0.5;Delta=550.001;
beta=1.4388/T;
i=1;j=1;
```

```

w=[1 7 10 51 101:100:401 501:10:601 631 661 701 801:100:3001];
W=[5.1:1:10.1 12.1:2:20.1 25.1 30.1:10:490.1 499.1 500.1:10:2000.1];
z=[-23000:10:23000];
zp=[0:10:23000];

while j<=45 %Number of w;
    i=1;
    while i<=211 %Number of W;
        PK=A/(sqrt(2*pi)*d/2.35)*exp(-(W(i)-Wpk)^2/(2*d^2/2.35^2)); %Gaussian PK.
        %BG=A2/(sqrt(2*pi)*d2/2.35)*exp(-(W(i)-Wpk2)^2/(2*d2^2/2.35^2));% Gaussian PK.
        %BG=A2*d2/(2*pi)/((W(i)-Wpk2)^2+d2^2/4); %Lorentzian PK.
        BG=1.0*heaviside(W(i)-500)*heaviside(800-W(i))+0.2*heaviside(W(i)-800)
            *heaviside(1000-W(i));
        %BG=B*heaviside(W(i)-C1)*heaviside(C2-W(i));
        %BG=Is*W(i)/(Wo^2+W(i)^2); \% MMP background.
        N_0=pref*T/300;

% Calculations for TAU;
N=(N_0+(1-N_0)*(z-W(i)).^8/Delta^8).*heaviside(Delta-abs(z-W(i)))
    +(1+8/9*(1-N_0))*heaviside(2*Delta-abs(z-W(i))).*heaviside(abs(z-W(i))
    -Delta)+heaviside(abs(z-W(i))-2*Delta); % Recovery width=1*Delta;
%N=(N_0+(1-N_0)*(z-W(i)).^8/Delta^8).*heaviside(Delta-abs(z-W(i)))
% +(1+80/9*(1-N_0))*heaviside(1.1*Delta-abs(z-W(i))).*heaviside(abs(z-W(i))
% -Delta)+heaviside(abs(z-W(i))-1.1*Delta); %Recovery width=0.1*Delta;
n_B=1/(exp(beta*W(i))-1);
f1=1./(exp(beta*(z-W(i)))+1);

```

```

f2=1./(exp(beta*(z-w(j)))+1);
f3=1./(exp(beta*(z+w(j)))+1);
DT=N.*(n_B+1-f1).*(f2-f3);
int_z=cumtrapz(z,DT);
g(j,i)=(PK+BG)*int_z(4601);

% Calculations for -2*Re(optical self-energy);
N_S=(N_0+(1-N_0)*zp.^8/Delta^8).*heaviside(Delta-abs(zp))
      +(1+8/9*(1-N_0))*heaviside(2*Delta-abs(zp)).*heaviside(abs(zp)-Delta)
      +heaviside(abs(zp)-2*Delta); % Recovery width=1*Delta;
N_SP=(N_0+(1-N_0)*(w(j)-W(i))^8/Delta^8)*heaviside(Delta-abs(w(j)-W(i)))
      +(1+8/9*(1-N_0))*heaviside(2*Delta-abs(w(j)-W(i))).*heaviside(abs(w(j)
      -W(i))-Delta)+heaviside(abs(w(j)-W(i))-2*Delta); %Recovery width=1*Delt
IZP=N_S.*log((zp+W(i)).^2)-(N_S-N_SP).*log(abs((zp+W(i)).^2-w(j)^2));
int_zp=cumtrapz(zp,IZP);
R=N_SP*((2.3e4+W(i)-w(j))*log(abs(2.3e4+W(i)-w(j)))-(W(i)-w(j))
      *log(abs(W(i)-w(j)))+(2.3e4+W(i)+w(j))*log(abs(2.3e4+W(i)+w(j)))
      -(W(i)+w(j))*log(abs(W(i)+w(j)))-2*2.3e4);
f(j,i)=(PK+BG)*(int_zp(2301)-R);

i=i+1;
end
j
j=j+1;
end
% Calculations for 1/tau;

```

```
int_W=cumtrapz(W,g');
TAU=2*pi./w.*int_W(211,:)+525.7;

% Calculations for -2*Re(optical self-energy);
intWRSF=cumtrapz(W,f');
RSF=2./w.*intWRSF(211,:);

%-----Results output-----
filename=input('Enter the output filename > ','s'); fid=fopen(filename,'w');
fprintf(fid,' Freq      1/tau      Re(self energy)\n'); fprintf(fid,'/*\n');
fprintf(fid,'%8.4f %8.4f %8.4f\n',[w;TAU;RSF]);
fclose(fid);

%-----Figures plotting-----
hold on
plot(w,TAU);
xlabel('Frequency (cm-1)');
ylabel('1/\tau(\omega) (cm-1)');
axis([0 3000 0 5000]);
hold off
```